Biodegradation Study of Magnesium-based Implant Materials under Physiological Conditions

Dissertation

zur Erlangung des akademischen Grades

Doktor der Ingenieurwissenschaften

(Dr.-Ing.)

der Technischen Fakultät

der Christian-Albrechts-Universität zu Kiel

vorgelegt von

Nezha Ahmad Agha

Kiel 2016

Erstgutachterin: Prof. Dr. Regine Willumeit-Römer

Zweitgutachterin: Prof. Dr. Christine Selhuber-Unkel

Termin Der Disputation: 21.06.2016

Erklärung

Hiermit erkläre ich, dass die beigefügte Dissertation, abgesehen von der Beratung durch die Betreuerin, nach Inhalt und Form meine eigene Arbeit ist.

Die Arbeit, ganz oder zum Teil, wurde nie schon einer anderen Stelle im Rahmen eines Prüfungsverfahrens vorgelegt und ist nie veröffentlicht worden oder zur Veröffentlichung vorgelegt worden.

Außerdem ist die Arbeit unter Einhaltung der Regeln guter wissenschaftlicher Praxis der Deutschen Forschungsgemeinschaft entstanden.

Geesthacht, den 18.04.2016

Abstract

Biodegradable magnesium and its alloys are new-generation materials for orthopaedic implants. They eliminate further complications that may accompany retrieval surgery, which is particularly helpful in bone fixation for children. In addition to their degradability, some magnesium alloys have been proven to exhibit good bioactivity as well as physical and mechanical properties that are comparable to those of bone. During the degradation process, the interface between material and tissue is continuously changing. Moreover, rapid or uncontrolled degradation is detrimental to *in vivo* outcomes. *In vitro* setups utilising physiological conditions are promising for material/degradation analysis prior to animal experiments. In addition, understanding the *in vivo* degradation mechanisms can reveal new applications for magnesium implants. The work of this study is divided into two parts. In **part 1,** the influence of important blood plasma salts on pure magnesium degradation and product composition was elucidated first in Hank's Balanced Salt solution without calcium or magnesium (HBSS) and then in complex cell culture media, including Dulbecco's Modified Eagle's Medium (DMEM) and Roswell Park Memorial Institute medium (RPMI-1640). All immersion media were supplemented with 10% of Fetal Bovine Serum (FBS). The degradation interface was analysed with Electron-Induced X-ray Emission (EIXE) spectroscopy and Fourier Transform Infrared Reflection micro-spectroscopy (FTIR). The results highlight the importance of bicarbonate as a blood-buffering salt on the formation of magnesium carbonate as the main degradation product. In the presence of phosphate, and calcium containing salts the material surface was passivated by forming low-soluble depositions which reduced the degradation rate. In **part 2,** higher complexity was achieved by studying the direct influence of osteoblast cells on the degradation of pure magnesium and two alloys, Mg-2Ag and Mg-10Gd. Samples were immersed in DMEM with 10% FBS for up to 14 days. The degradation interface (directly beneath the cells) was analysed with a new approach that uses a scanning electron microscope equipped with energy-dispersive X-ray and a focused ion beam. The influence of the materials degradation on cell metabolism was also examined using different parameters, such as an active mineralisation process, lactate dehydrogenase, and Live/Dead staining. Results indicate the role of osteoblasts in altering the chemical composition by forcing apatite precipitations. The alloying element that was used had a cross-influence on the metabolic activity of the cells and, therefore, their function. The interface on Mg-10Gd was rich in Ca, P and Gd, which lead to the assumption that Gd itself potentially contributed to HA precipitation and increased bone mineralisation ability. By contrast, initial cell stress and damage was shown with Mg-2Ag, and therefore, less mineralisation matrix was observed on the surface.

Zusammenfassung

Magnesium und Magnesiumlegierungen haben ein beträchtliches Potential als abbaubares Material für orthopädische Anwendungen. Während des Degradationsprozesses verändert sich das Interface zwischen Zellen und Material kontinuierlich. Eine zu schnelle oder unkontrollierte Degradation kann zu einem Versagen des Materials *in vivo* führen. Um solches Versagen zu verhindern ist es notwendig, *In vitro* Methoden zur Material- und Degradationsanalyse zu entwickeln und anzuwenden. Diese orientieren sich unter Ausnutzung physiologischer Bedingungen möglichst nah am *in vivo*-Geschehen und sollten vor Tierexperimenten durchgeführt werden. Darüber hinaus kann das Verständnis der Degradationsmechanismen *in vivo* zu neuen Anwendungsfeldern führen. Das Ziel dieser Arbeit liegt darin, den Einfluss von im Körper vorhandenen Salzen auf die chemische Zusammensetzung der Degradationsschicht zu verstehen (chemischer Aspekt). Zweitens sollen die Mechanismen der Änderung dieser Degradationsschicht in Anwesenheit der knochenbildenden Zellen (Osteoblasten) definiert werden (biologischer Aspekt). Daher teilt sich die Arbeit in zwei Teile. Im **ersten Teil** wurde analysiert, welche anorganischen Salze einen signifikanten Einfluss auf die Zusammensetzung der Degradationsschicht haben. Der Einfluss auf die Degradation und die Degradationsprodukte wurde zunächst in Hank's Balanced Salt solution (HBSS) und danach in komplexen Zellkulturmedien (Dulbecco's Modified Eagle's Medium (DMEM) und Roswell Park Memorial Institute Medium (RPMI-1640) untersucht. In allen Versuchen wurden Proteine in Form von Fötalem Kälberserum (FKS, 10 %) hinzugegeben. Das Degradationsinterface wurde mit Elektronen-induzierter Röntgenemissionsspektroskopie (EIXE) und Fourier-Transformations-Infrarotspektrometrie (FTIR) analysiert. Die Ergebnisse zeigen, dass in Gegenwart von Bikarbonat (dem Hauptbestandteil des Blut-Puffersystems) Magnesiumkarbonat als das dominante Degradationsprodukt gebildet wird. Bei Zugabe von Phosphaten und Kalziumsalzen wurde die Materialoberfläche durch die Bildung von Produkten mit geringer Löslichkeit passiviert. Im **zweiten Teil** der Arbeit wurden komplexe Systeme untersucht. Hier war das Ziel, den direkten Einfluss von Zellen (Osteoblasten) auf das Degradationsverhalten von Rein-Magnesium, Mg-2Ag und Mg-10Gd zu verstehen. Dies erfolgte über Immersion der verschiedenen Materialien in DMEM + 10 % FKS bis zu 14 Tagen. Das Degradationsinterface unterhalb der Zellen wurde mit einer für diese Anwendung erstmalig etablierten komplexen Messtechnik untersucht (Rasterelektronenmikroskope mit fokussiertem Ionenstrahl in Kombination mit Energiedispersiver Röntgen-spektroskopie; FIB-SEM/EDX). Die Material-Zell Interaktion wurde außerdem mittels bildgebender Methoden (Lebend-Tot-Färbung, OsteoImage zur Färbung von Hydroxylapatit) und biochemischer Methoden (Analyse der Bildung von Alkalischer Phosphatase). Osteoblasten greifen aktiv in

das Degradationsgeschehen ein und forcieren die Bildung von Hydroxylapatit bei direktem Kontakt mit dem Material. Dadurch wird die Zusammensetzung der Degradationsschicht geändert. Je nach zugegebenem Legierungselement konnten zusätzliche Effekte beobachtet werden. Auf der Mg-10Gd Legierung wurde ein erhöhter Anteil von Ca, P und Gd gefunden, was zu der Annahme führt, dass Gadolinium die metabolische Aktivität der Osteoblasten verstärkte, sowie einen positiven Einfluss auf die Matrixbildung hat. Die Zugabe von Silber als Legierungselement führte zu gegensätzlichen Effekten, messbar an initialem Zellstress und Zytotoxizität.

Contents

1. Introduction

1.1. The innovation of biodegradable metals

Advances in material science and engineering have allowed structural material adjustment to meet the desired material properties. Continuous developments in health care and improvements in living standards have increased the expectation for a better quality of life. In this context, researchers are working on developing new materials and technologies to create implants with higher clinical performance. The new generation of biodegradable material grew out of the need to have only temporary implant support for the surrounding tissue during the healing process [1]. The concept of biodegradation was first applied in medicine through the use of biodegradable polymer sutures [2, 3]. However, biodegradable metals have a novel concept that actually breaks the established paradigm of ‘‘metallic biomaterials must be corrosion resistant‘‘ [4].

The concept of degradable biomaterials is derived from the fact that some implants might be needed only temporarily to supporting the healing process of injured tissue. This temporary function is needed in some applications, such in cardiovascular and orthopaedic; especially in paediatric field. Those temporary implants possess similar characteristics, but because they are employed in different implantation sites, they might have different functions. For example, temporary cardiovascular implants used as stents should be able to open a narrowed artery and hold it open until the vessel remodels. Afterwards, the stent should degrade and be replaced by new arterial vessel tissue [5]. Ideally, biodegradable coronary stents would reach a balance between mechanical integrity and degradation. Therefore, the degradation should begin at a very slow rate to maintain the stent’s optimal mechanical integrity until the arterial vessel remodelling process is completed, which is expected to take 6 to 12 months [6, 7]. Thereafter, whilst the mechanical integrity decreases, the degradation should progress. Temporary orthopaedic implants, such as bone fixation screws or pins, should be able to join a fractured bone and hold it securely until sufficient new bone is formed. Degradation and replacement by new bone tissue should then be achieved [8]. In paediatric applications, the implant should also match the growing implantation site, the surrounding tissue, and the organs.

Generally, the degradation rate of biodegradable metals should be sufficient to avoid an intolerable accumulation of degradation products around the implantation site and in the surrounding tissue. Figure 1.1 shows two currently available biodegradable implants.

The definition of biodegradable metals, based on [4], is as follows: “biodegradable metals are metals expected to corrode gradually *in vivo* with an appropriate host response elicited by the release of corrosion products and then dissolve completely upon fulfilling the mission to assist tissue healing with no implant residues”. Therefore, the major component of

biodegradable metals should be essential metallic elements that can be metabolised by the human body, and demonstrate appropriate degradation rates and modes in the human body.

Figure 1.1: Some magnesium implants; left: BIOTRONIK magnesium bio-absorbable drug eluting stent; right: Screws used to correct mild hallux valgus: dark (left): Titanium fracture compressing screw and light (right): MAGNEZIX compression screw based on magnesium-REE (rare earth elements) alloy *(with permission from Magnesium Research Journal* [9]*)*.

Until now, newly developed biodegradable metals have been based on three main systems: magnesium, iron, and zinc. As shown in Figure 1.2, it is quite clear that among these types, Mg-based biodegradable metal studies are the main force with hundreds of publications on *in vitro* cytotoxicity, animal testing and clinical trials [10].

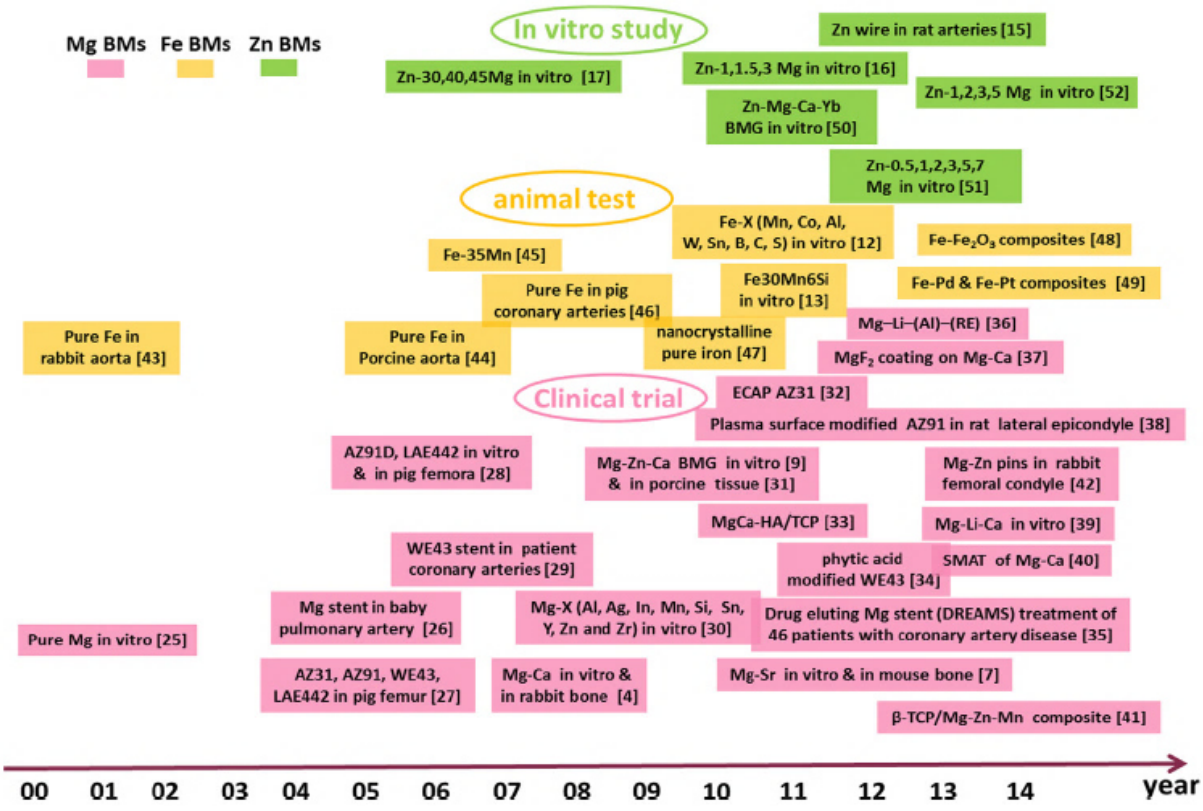

Figure 1.2: Research status of the three biodegradable metal (BMs) systems: Mg-, Fe-, and Zn-based BMs *(with permission from ELSEVIER* [10]*)*.

1.2. Magnesium as a biodegradable metal for bone implants

In terms of mechanical properties, metals are considered to be more suitable than polymers for bone fixation applications, which require a high strength-to-bulk ratio (e.g., internal bone fixation screws or pins) [9].

Magnesium is a light material with a density of 1.74 g/cm^3 and is 1.6 and 4.5 times less dense than aluminium and steel, respectively. Its fracture toughness is greater than that of ceramic biomaterials, such as hydroxyapatite [9]. Magnesium's elastic modules and compressive yield strength are closer to those of natural bone compared to other commonly used biomaterial metals. Table 1.1 shows the mechanical properties of bone tissue compared to different biomaterial types and some magnesium-based alloys. Magnesium is essential to human metabolism and is naturally found in bone tissue. It is the fourth most abundant cation in the human body. It has been estimated that 1 mole of magnesium is stored in the body of a normal 70 kg adult, where half of the total physiological magnesium is stored in bone tissue [11-15]. Magnesium is a co-factor for many enzymes, and it stabilises the structures of cell membranes, DNA and RNA [13, 14]. The level of magnesium in extracellular fluid ranges from 0.7 to 1.05 mmol/L [11]. Serum magnesium levels exceeding 1.05 mmol/L can lead to muscular paralysis, hypotension and respiratory distress, and cardiac arrest occurs with severely high levels of 6 to 7 mmol/L [11]. However, it has been reported that the incidence of hypermagnesemia is rare due to the efficient excretion of the element in urine. The *in vivo* corrosion of magnesium-based materials involves the formation of soluble, nontoxic corrosion products that are harmlessly excreted in the urine [11, 12]. By contrast, because of its functional role and presence in bone tissue, magnesium may actually have stimulatory effects on the growth of new bone tissue [16-18]. Therefore, magnesium and its alloys can fulfil the need for a lightweight, degradable, load-bearing orthopaedic implant. These types of implants should remain in the body and maintain mechanical integrity for 12 to 18 weeks whilst the bone tissue heals, and eventually, the implant will be replaced by natural tissue [19, 20]. The major drawback of magnesium in many engineering applications is its low corrosion resistance, which is a highly influential characteristic in biomaterials applications [21]. Therefore, magnesium is still not commonly used in clinics because of its high degradation rate in some cases. In addition, the degradation process of magnesium is accompanied by hydrogen evolution and solution alkalisation, which may delay healing and cause implant loosening [21].

Table 1.1: Mechanical properties of bone tissue and different biomaterials *(with permission from Magnesium Research Journal* [9]*)*.

	Tensile strength [MPa]	**Young's Modulus [GPa]**	**Density [g/cm^3]**
Tissue [88]			
Cortical bone	35 - 283	5 - 23	1.8 - 2.0
Cancellous bone	1.5 - 38	0.01 - 1.57	1.0 - 1.4
Polymers [89-92]			
Polyglocolide (PGA)	60 - 99.7	6 - 7	1.5 - 1.707
Polylactide (PLA)	32.2	0.35 - 3.5	1.21 - 1.25
Poly-L-lactide (PLLA)	45 - 70	2.7 - 4.14	1.24 - 1.30
Polycaprolactone (PCL)	23	0.21 - 0.44	1.11 - 1.146
Chitosan	34 - 44	1.1 - 1.4	n/a
Calcium Phosphates [88, 93]			
Beta-Tri-calcium phosphate (β-TCP)	18 - 130	23.4 - 84.8	3.14
Hydroxyapatite (HA)	40 - 200	70 - 120	3.05 - 3.15
Bulk metallic glasses [94]			
Bioglass (45S5)	42	35	2.2 - 2.8
Mg67Zn28Ca5	675 - 894	48	-
Metals			
Titanium alloys [95, 96]			
Ti6Al4V	895 - 930	110 - 114	4.43
Ti6Al7Nb	900 - 1050	114.00	4.51
Ti13Nb13Zr	973 - 1037	79 - 84	4.66
Iron alloys [97, 98]			
Pure Iron (electroformed)	160 - 435	211	7.86
Fe35Mn	235	-	-
Magnesium alloys [21, 88, 99-101]			
Pure Mg	90	44	1.74
AZ91E	165 - 457	45	1.81
WE43	250 - 277	44 - 46	1.84
Mg10Gd	69.1 - 85.4	-	1.88
Mg6Zn	277 - 281	42.3	1.84
Mg1Ca	75 - 240	-	1.73

1.3. Implantation site: Bone as living tissue

Bone comprises trabecular (cancellous) and cortical bone parts. Trabecular bone is a mesh bone structure surrounded by cortical bone, which is dense and hard, giving the bone its stiffness (See Table 1.1) [22]. The adult human skeleton comprises 80% cortical bone and 20% trabecular bone [22]. Different bones and skeletal sites have different ratios of these two components. Both trabecular and cortical bone are composed of osteons [22]. Bone undergoes longitudinal and radial growth, modelling and remodelling during its life span. Those processes are mediated through three main types of bone cells; osteoblasts, osteoclasts and osteocytes (see Figure 1.4 a) [22]. Bone remodelling is the process by which bone is renewed to maintain its strength and mineral homeostasis. This process involves the continuous removal of old bone, replacement with a newly synthesised proteinaceous matrix and subsequent mineralisation of the matrix to form new bone [22, 23].

Role of osteoblasts in bone formation

Osteoblast cells work in groups to generate new bone matrices. The work of osteoblasts in bone formation is linked to the role of osteoclasts in bone resorption, meaning that if one goes down, the other usually follows. This coupling between formation and resorption is controlled by several mechanisms that are not yet fully understood. First, osteoblasts are able to stimulate osteoclast differentiation by the production of osteoclast-stimulating factors, such as RANKL (receptor activator of NF-kB ligands) and M-CSF (macrophage colony-stimulating factor). RANKL is a key cytokine for osteoclast formation. In addition, osteoclast activity is coupled to osteoblast activity. During osteoclastic bone resorption, multiple factors are released from the extracellular matrix, including IGF-I (insulin-growth factor I) and TGFß (transforming growth factor ß), which control the differentiation and activity of osteoblasts after their release (Figure 1.3) [23].

Active osteoblasts work on the surface of new bone and form an uncalcified, collagen-rich protein mixture known as osteoid. Osteoid comprises bony matrix proteins, such as type I collagen, and other non-collagenous proteins, including osteocalcin, bone sialoprotein, osteopontin, and osteonectin [23]. After it is formed, it mineralises to become bone. After making bone, osteoblasts becomes either lining cells or osteocytes [23].

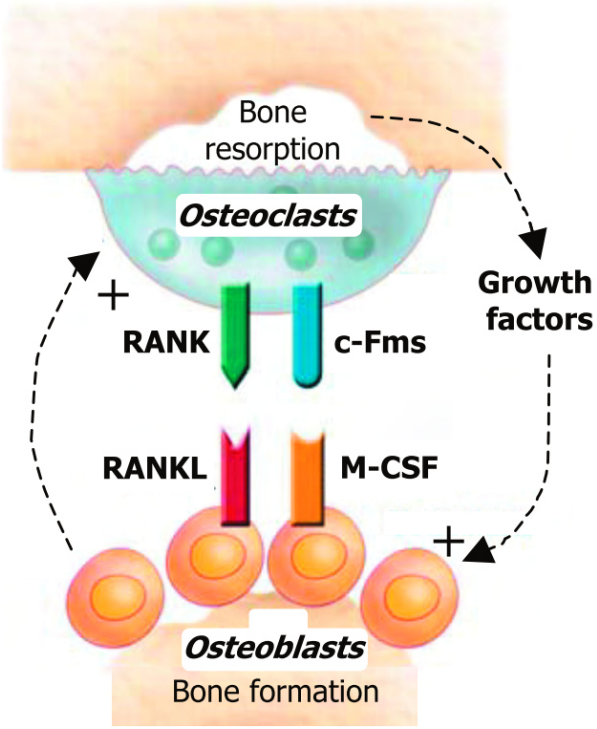

Figure 1.3: The coupled function and differentiation of osteoblasts and osteoclasts. Osteoblasts activate osteoclast differentiation by expressing RANKL and M-CSF, which bind to RANK and c-Fms receptors on the surface of osteoclasts. During bone resorption, osteoclasts release various growth factors from the bone matrix that in turn stimulate osteoblast differentiation *(with permission from The Journal of Clinical Investigation* [24]*)*.

Bone matrix mineralisation

Bone comprises 20 to 40% organic components, 50 to 70% minerals, 5 to 10% water, and <3% lipids. Bone minerals provides stiffness and load-bearing strength to bone, whereas the organic matrix provides elasticity and flexibility [22]. Bone mineral content is primarily hydroxyapatite [$Ca_{10}(PO_4)_6(OH)_2$] with small amounts of carbonate, magnesium, and acid phosphate [22]. Compared to geological hydroxyapatite, bone hydroxyapatite crystals are very small (approximately 200 Å in their largest dimension). These small, poorly carbonated-substituted crystals are more soluble than the geological ones allowing support mineral metabolism [22].

Osteoblasts as bone-forming cells are primarily responsible for the mineralisation process in bone (Figure 1.4). First, osteoblasts produce a non-mineralised extracellular matrix that predominantly consists of collagen type I. These collagen fibres determine the structural organisation for other extracellular matrix proteins and act as a template for mineral deposition [23]. Osteoblasts also produce a wide variety of so-called non-collagenous extracellular matrix proteins. These includes enzymes, growth factors, calcium-binding proteins and several other proteins that are important for the structure of the extracellular matrix [23]. After osteoblasts have produced a complete and maturated extracellular matrix, hydroxyapatite is deposited in this matrix [23]. Bone mineralisation is a complicated process controlled by many factors, including calcium and phosphate concentrations, enzyme activity, and the composition of the extracellular matrix. The initiation of mineralisation requires the precipitation and attachment of hydroxyapatite crystals to the extracellular matrix [23]. One possible mechanism of hydroxyapatite crystal formation is through extracellular matrix vesicles. It has been demonstrated that osteoblasts produce extracellular matrix vesicles by polarised budding and pinching off vesicles from specific regions of their outer plasma membranes. After the extracellular matrix vesicles are released into the extracellular matrix, they initiate the formation of the first mineral crystals [23]. The osteoblast differentiation marker alkaline phosphatase is suggested to play a role in the mineralisation process, where it hydrolyses organic phosphate substrates to release free inorganic phosphate. This enzyme is highly expressed in matrix vesicles along with several phosphate and calcium transporters. These transporters increase local calcium and phosphate concentrations and therefore initiate hydroxyapatite crystal formation. This is one mechanism, there might be additional mechanisms in which mineralisation in bone is initiated [23].

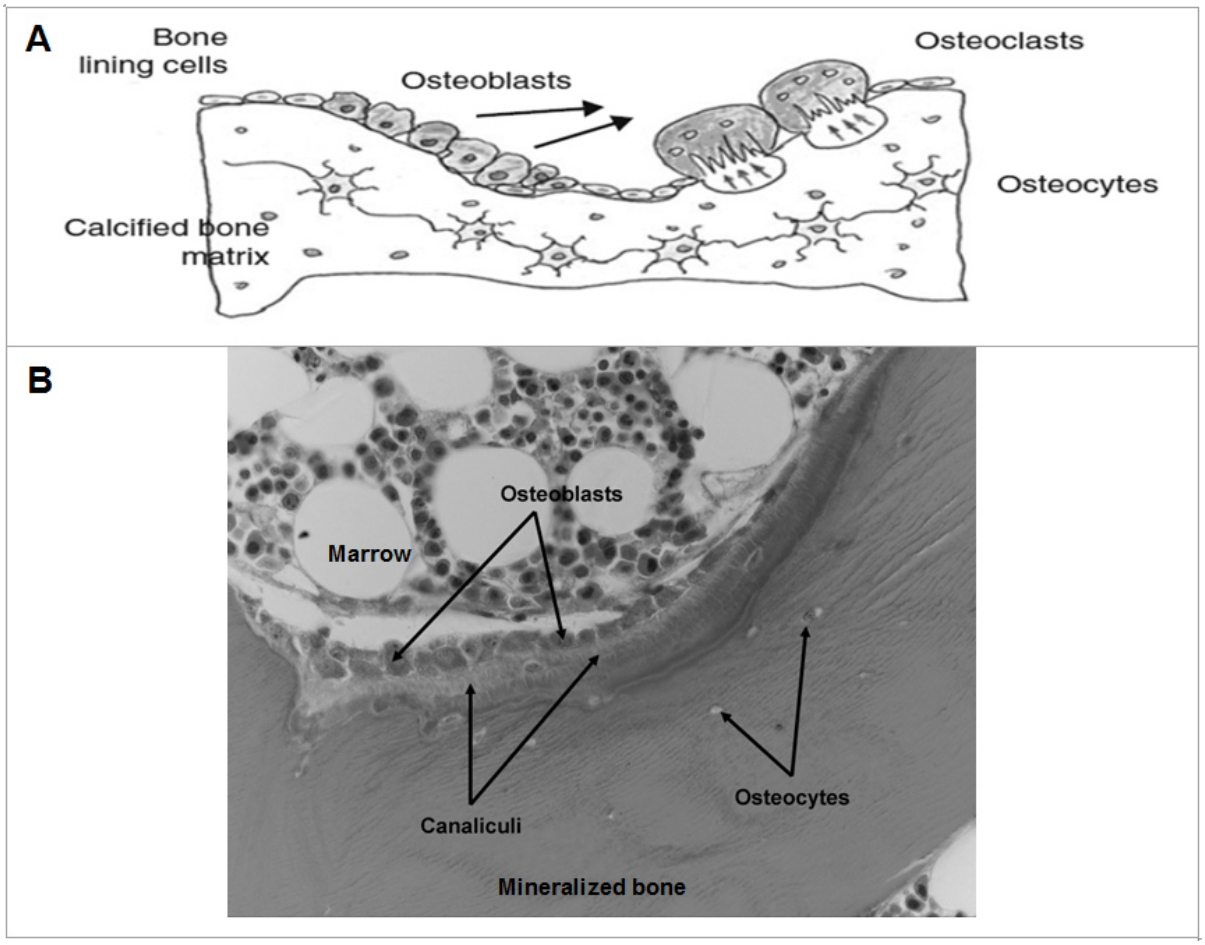

Figure 1.4: A: Four different cell types reside in bone and are responsible for bone growth, modelling and remodelling: 1] osteoclasts resorb bone by acidification and secretion of a wide variety of proteases, 2] osteoblasts produce new bone matrix, 3] osteocytes sense mechanical strains, and 4] lining cells cover the bone tissue *(with permission from Springer* [25]*)*. **B:** Osteoblasts synthesise the proteinaceous matrix composed mostly of type I collagen to fill in resorption pits. The proteinaceous matrix is then gradually mineralised to form new bone *(with permission from the American Society of Nephrology* [22]*)*.

1.4. Overview on the use of magnesium orthopaedic implants from past to present

Around 1900, physician Erwin Payr proposed the first Mg implants for musculoskeletal applications, including pins, nails, wires and plates. Payr was probably the most influential investigator in this field, proposing that the levels of tissue oxygen, water content, carbon dioxide, and salts in blood and the chemical processes in cells were primarily responsible for magnesium degradation *in vivo* [26]. In 1906, Albin Lambotte also investigated Mg implants. He declared that Mg could only be implanted if it was not combined with other metallic implants to prevent electrolytic corrosion. This was the outcome of his first clinical case in which he used magnesium plate and steel screws to fixate a fracture [26]. He then decided to use Mg implants to treat supracondylar fractures in children because this type of fracture heals fast. Lambotte and his assistant, Jean Verbrugge, operated on 4 children who were

between 7 and 10 years of age with these types of fractures. All of the fractures healed without complications except for those caused by gas cavities. However, the evolved cavities disappeared after several weeks and were not a major concern in any of the reported clinical cases [26]. In 1924, Zierold compared the reaction of different metals on bone tissue and concluded that magnesium has little effect as a connective tissue stimulant. He hypothesised that magnesium may retard as well as accelerate new bone production [26]. Around 1938, McBride followed the work of Jean Verbrugge. He found that plates made of magnesium metal and put on the surface were not suitable, because of the higher adsorption behaviour. By contrast, screws were more resistant to corrosion, particularly when the screws were fitted more tightly into hard cortical bone [26]. McBride found that magnesium stimulated the early proliferation of connective tissue and caused an overproduction of callus. He further recommended that magnesium implants be used in compound fractures and in the fixation of autologous grafts, where prethreaded screws could reduce operative time and provide firm fixation [26, 27]. In 1948, Troitski and Tsitrin reported the successful treatment of pseudarthrosis with a plate and screw made of an Mg-Cd alloy. The implant was completely resorbed and stimulated callus bone formation. This bone-stimulating effect was hypothesised to be based on the formation of $MgCO_3$, which was observed in the corrosion layer [26, 28]. Troitski, Tsitrin and Verbrugge stated that the implantation of magnesium into inflammatory tissue leads to neutralisation of the acidic environment and therefore stimulates the formation of callus bone [26]. These early examples show that magnesium-based materials are non-toxic and may actually stimulate bone tissue healing (see Figure 1.5). However, the too-rapid corrosion rates of pure magnesium and these simple alloys were not compatible with the required healing rate because it had been recommended that the implant fixture be present for at least 12 weeks [19]. Therefore, subsequent studies focused on improving corrosion resistance by adjusting the type and concentration of the alloying elements that were added to magnesium to achieve the suitable mechanical properties of the material along with the optimised degradation profile. Stroganov et al. reported that magnesium alloyed with 0.4-4 wt% rare earth metal; 0.05-1.2 wt% cadmium; 0.05-1.0 wt% calcium or aluminium; and variable trace (<0.8 wt%) levels of manganese, silver, zirconium or silicon had a slowed corrosion rate, with 3-mm diameter pins present for 5 months and 8-mm diameter pins present for 11 months *in vivo*. No information has been provided about the mechanical integrity over time or whether the potentially toxic effects of the alloying elements were considered [29].

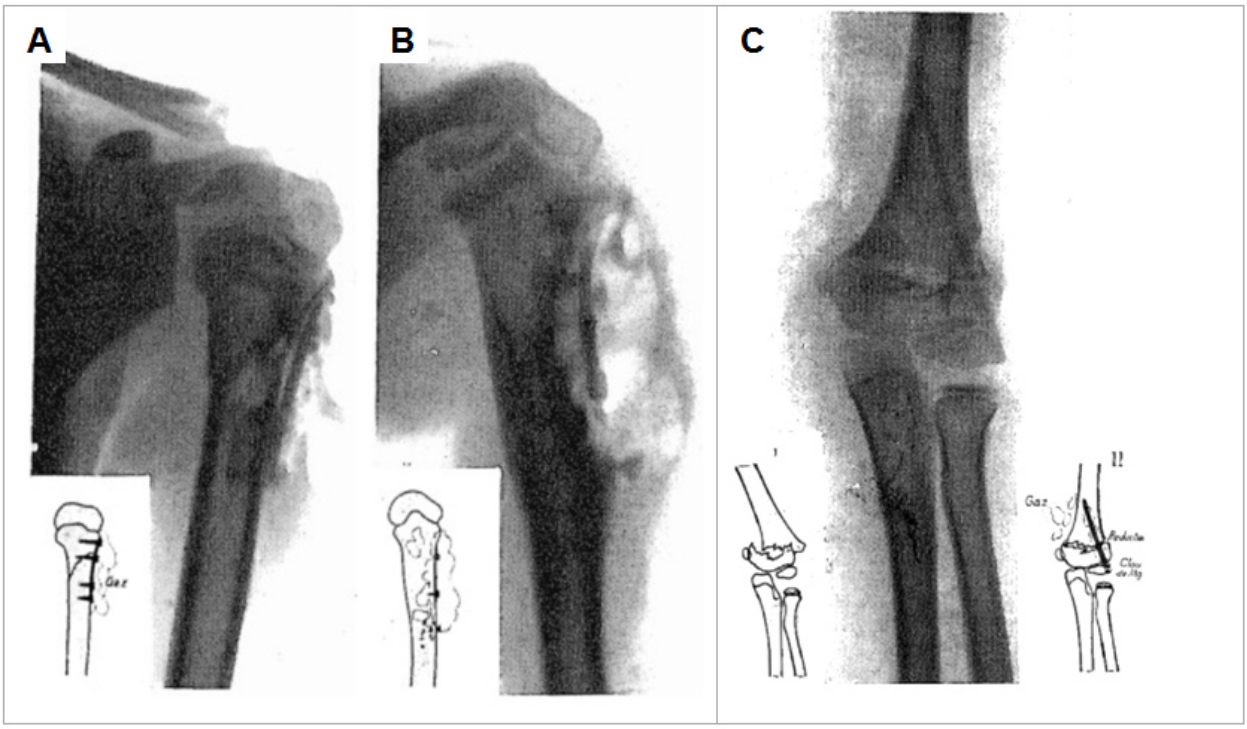

Figure 1.5: Verbrugge used a magnesium plate and screws to stabilise a diaphyseal humerus fracture in an 8-year-old child. **(A)** Immediately after the operation with initial gas formation; **(B)** 3 weeks after the operation, the Mg plate was largely degraded. **(C)** Postoperative X-ray of a supracondylar fracture of a 7-year-old child treated with a Dow magnesium nail *(with permission from ELSEVIER* [26]*)*.

In 2005, Witte et al. explored the *in vivo* degradation of magnesium-based alloys [19]. Implants consisting of rods that were 1.5 mm in diameter and 20 mm in length were inserted into the femurs of guinea pigs. Polylactide rods of the same dimensions was used as a control. Radiographs were taken frequently. Implants were harvested at 6 and 18 weeks after implantation. Synchrotron radiation-based microtomography was used to characterise the degradation of the implants. Increased bone area was observed in all groups with magnesium-based implants ($P< 0.05$) at weeks 6 and 18 compared to the polymer control groups [19].

Same findings have been observed in more recent *in vivo* work. For example, Kraus et al. investigate the bone tissue response to degradable pin implants in a growing rat skeleton over the degradation period. Two magnesium alloys were used for this study, including fast-degrading ZX50 (composition in wt%: 5% Zn, 0.25% Ca, 0.15% Mn, rest Mg), and slow-degrading WZ21 (composition in wt%: 1% Zn, 0.25% Ca, 0.15% Mn, 2% Y, rest Mg). Despite the large amount of hydrogen gas formation with ZX50 pins, callus formation occurred, bone function was not permanently harmed, and the bone recovered quickly after complete pin degradation. WZ21 kept its integrity for more than four weeks and showed good osteo-conductive properties by enhancing bone accumulation at the pin surface, and gas formation did not hinder bone generation [30] (see Figure 1.6).

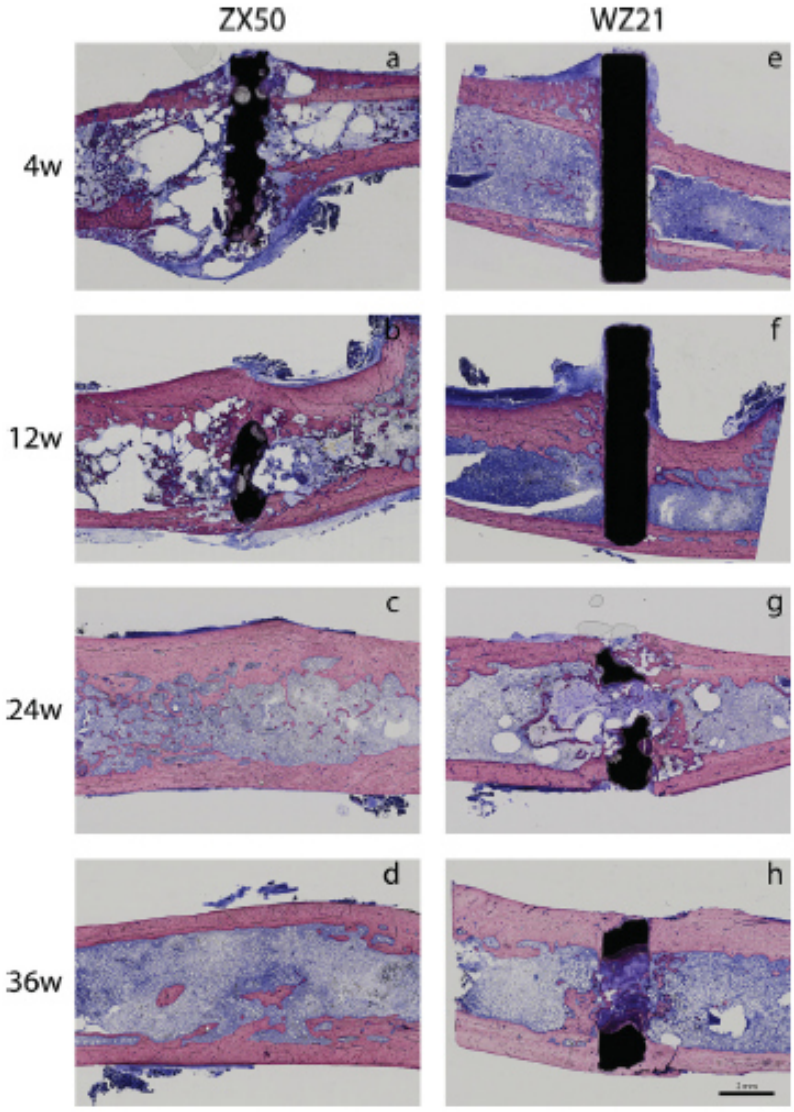

Figure 1.6: Histological thin slides of ZX50 **(a-d)** and WZ21 **(e-h)** pins (in a Levai-Laczko staining). ZX50 showed complete bone healing despite the massive callus formation and release of high amounts of gas (a). WZ21 showed enhanced new bone formation around the implant, which revealed the osteo-conductive properties of magnesium alloys. The scale bar represent 2 mm *(with permission from ELSEVIER* [30]*)*.

The use of magnesium implants for orthopaedic applications in human clinical trials started to be published in 2015. Plaaß et al. treated 22 patients suffering from Hallux valgus deformity with a distal metatarsal osteotomy using a biodegradable Mg-based implant (MAGNEZIX screw, Syntellix GmbH) (see Figure 1.7). With the exception of one case with traumatic dislocation of the osteotomy, all other cases showed rapid and uneventful bony healing [31]. Those results were comparable to other studies on distal metatarsal osteotomies [32]. However, further studies on the use of biodegradable magnesium screws for these applications have been suggested because of the short follow-up period and small patient cohort [31]. Despite the fact that magnesium is currently in clinical trials, the full mechanisms through which degradation takes in the implantation site is not well known. In addition, defining the physiological influence on degradation and vice versa might suggest new applications for magnesium-based implants.

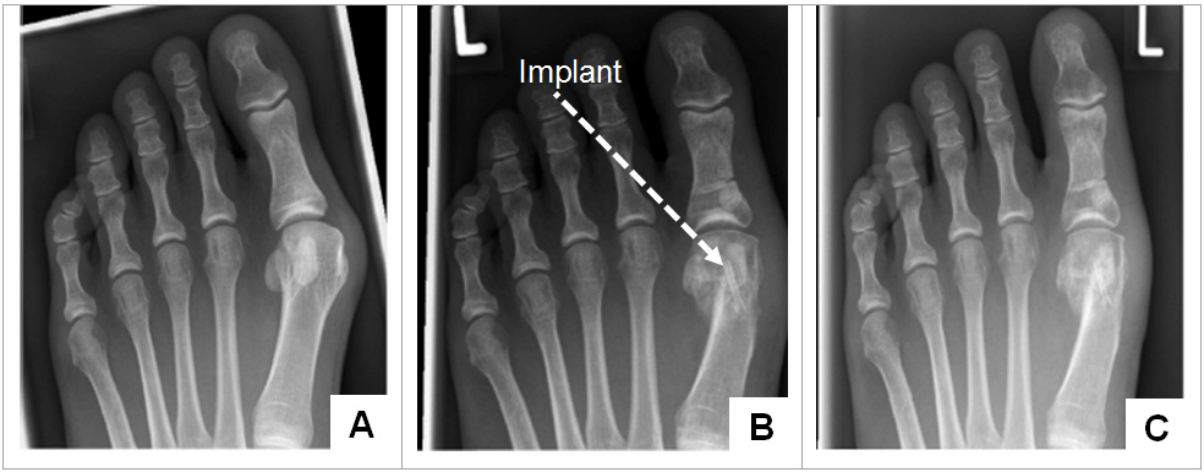

Figure 1.7: X-ray images of the healing process for a 28-year-old patient suffering from Hallux valgus deformation **(A)**. (**B**): Six weeks after implantation, a correction on the distal metatarsal took a place. **(C)**: Twelve weeks after the operation, secure consolidation and significant bone remodelling were observed *(with permission from ELSEVIER* [31]*)*.

1.5. Improvements in magnesium properties

It is clear that good mechanical properties are needed when using magnesium as an orthopaedic implant. Therefore, many studies have focused on this aspect by following the known mechanisms for strengthening metals. In theory, strengthening is hindering dislocations motions. This can be achieved by grain size reduction, solid-solution alloying, or secondary phases, as follows.

1- Effect of grain size

Grain refinement improves the strength of metals. A general relationship between yield stress and grain size was proposed by Hall [33] and expanded by Petch [34]:

$$\sigma_0 = \sigma_i + k/d^{1/2} \quad (1)$$

where σ_0: yield stress;

σ_i: friction stress, which is the overall resistance of the crystal lattice to dislocation movement;

k: locking parameter, which measures the relative hardening contribution of the grain boundaries; and

d: grain diameter.

The original explanation for this effect was that pile-ups formed at grain boundaries, which required a critical stress to break through them [33-35].

2- Effect of alloying elements

The introduction of solute atoms into interstitial or substitutional positions in the solvent atom lattice invariably produces alloys that stronger than the pure metal. If the solute atom is much smaller than the solvent atom, an interstitial solid solution forms. Elements commonly used to form interstitial solid solutions include H, N, C, and O. In a substitutional solid

solution, solute atoms replace solvent atoms in their lattice positions [36]. It should be noted that interstitial atoms have a greater strengthening effect than substitutional atoms [36].

3- Effect of secondary phases

A relative small number of alloy systems permit extensive solubility between two or more elements, and only a relatively small hardening effect can be produced in most alloy systems by solid solutions additions [36]. Therefore, many commercial alloys contain a heterogeneous microstructure consisting of two or more metallurgical phases. Precipitation strengthening is produced by solution treating and quenching an alloy in which a second phase is in solid solution at the elevated temperature but precipitates upon quenching and ageing at a lower temperature [36]. Many factors must be considered for a complete understanding of strengthening from second-phase particles. These factors include the size, shape, number, and distribution of the second-phase particles; the strength, ductility and strain-hardening behaviour of the matrix and second phase; the crystallographic fit between the phases; and the interfacial energy and interfacial bonding between phases [36].

Strength is often considered a critical property. However, it is not the only property that has to be considered. Ductility, elastic moduli, corrosion behaviour, rate of degradation and toxicology, among others, are also part of property profile, which is primarily influenced by the alloy composition and the processing step [37]. Therefore, improvements in the mechanical properties of magnesium alloys should coincide with the degradation behaviour, which is crucial for a biodegradable implant. Due to the high reactivity of magnesium, most of the alloying elements in their pure form or intermetallic phase are more noble than pure magnesium [21]. Therefore, the matrix acts as anode and dissolves. However, alloying is an essential step for improving the mechanical properties of magnesium and ease of alloy manufacture. Different possibilities exist to tailor the corrosion rate of magnesium by adjusting the type and concentration of alloying elements to achieve both the suitable mechanical properties of the material and the optimised degradation profile [38-47]. Two primary groups of magnesium alloying elements exist. One contains 2-10 wt% aluminium with trace additions of zinc and manganese. This group exhibits improvements in corrosion behaviour and mechanical properties [48]; however, its use as a bio-implant is limited by the observed toxicity of Al [42]. The second group uses metallic elements such as zinc, silver, or rare earth element mixture that can contain small amounts of zirconium, which imparts a fine-grain structure and therefore improves the mechanical properties [48]. Heat treatments on the cast alloys, such as solution treatment (T4) and ageing (T6), are ideally applied to achieve the desired improvements [49]. Further improvements can be made by selecting the processing method, defining and controlling its parameters. For example, extrusion has been used to improve the mechanical properties by achieving microstructure refinement [50]. Furthermore, applying a thermomechanical process through equal channel angular pressing

(ECAP) led to substantial grain refinement on extruded material, which increased the yield tensile strength and ultimate tensile strength [51, 52]. These treatments and processing methods directly influence the microstructure of the material, which further influences the degradation behaviour of the metal. A fine grain size has been proven to show improved degradation properties promoting homogenous degradation rather than localised one [53]. However, the relation between microstructure and degradation is still not completely understood. For example, it has been reported that corrosion resistance of hot extruded AZ31B alloys increases with finer grain size [54], but the opposite behaviour was observed in several other studies [55-57]. Therefore, researches on correlating the influence of the microstructure on degradation including dispersive studies on the microstructure grain size and the secondary phase type, size, amount, and distribution and their influence of corrosion of each specific alloy system are demanded.

In the following section, the use of silver and gadolinium as alloying elements is further discussed because investigations on Mg-2Ag and Mg-10Gd alloys were part of this thesis work.

Silver as an alloying element:

The Mg-Ag phase diagram shown in Figure 1.8 is established by applying a thermodynamic assessment [58]. Several portions are presented, including (1) the liquid; (2) the solid solution of Mg with a maximum solid solubility of 3.83 at.% Ag at the eutectic temperature of 472°C; (3) the solid solution of Ag with a maximum solid solubility of 29.3 at.% Mg at the eutectic temperature of 759.3°C; (4) the intermediate-phase Ag_3Mg; (5) the congruently melting Ag-Mg compound with a wide range of homogeneity that narrows at a lower temperature; and (6) the intermediate-phase $AgMg_3$ with a complex structure that forms by a peritectic reaction at 492°C [58].

It has been reported that in a binary alloying system (Mg-2Ag, Mg-4Ag, and Mg-6Ag), adding silver to magnesium cast and following it with a solution (T4) heat treatment improved the mechanical properties and exhibited an acceptable level of corrosion resistance (Figure 1.9) [59]. The reason for the improvement in corrosion resistance was attributed to dissolving the silver-enriched secondary phases in the matrix (α-Mg) by the heat treatment, which hindered the galvanic corrosion. Since these phases containing silver can shift the corrosion potential to the anodic direct [59]. In addition to using silver as an alloying element to improve magnesium properties, it is known that ionised silver Ag^+ has antibacterial properties [60, 61].

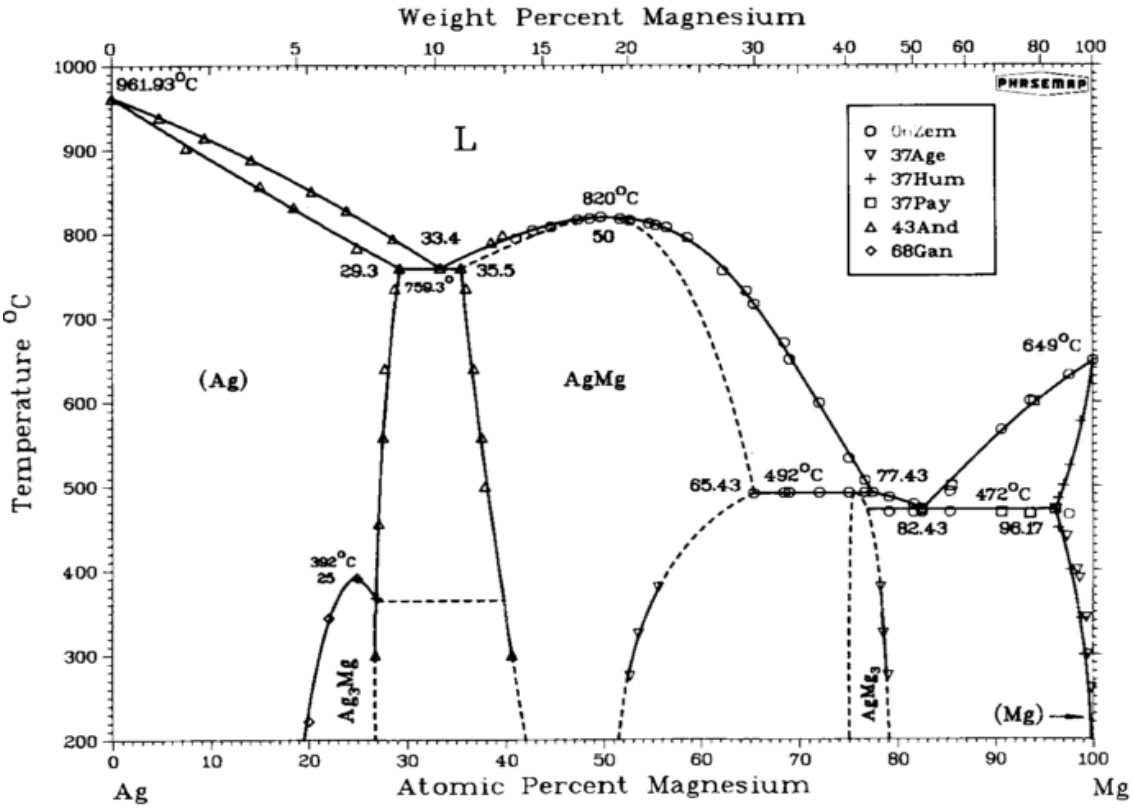

Figure 1.8: Assessed Ag-Mg phase diagram at atmospheric pressure with selected experimental data points *(with permission from Springer* [58]*).*

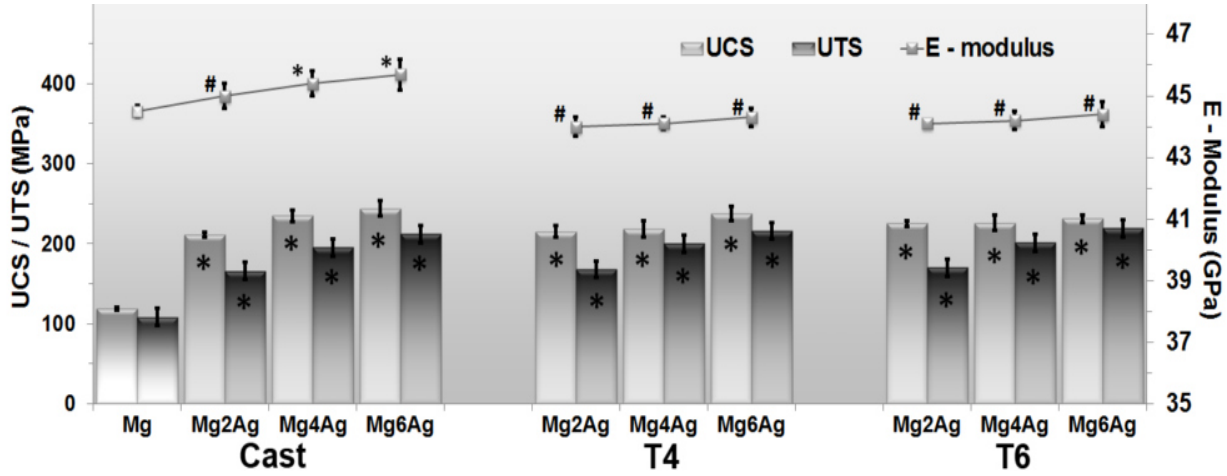

Figure 1.9: Ultimate tensile strength (UTS), ultimate compression strength (UCS) and Young's modulus (E) for different binary Mg-Ag alloys at different treatments states. T4 is the solution heat treatment at 440°C for 16 hours followed by water quenching at 25°C, and T6 is the ageing treatment of the solution- treated samples at 185°C for 8 hours followed by water quenching at 25°C. (* Significance level $p < 0.05$, # means no significant difference when compared with pure magnesium). (*Reproduced with permission from eCM journal* [59]*).*

Gadolinium as an alloying element:

Different investigations on Mg alloys containing gadolinium and additional REEs have been conducted [62-64]. These investigations have shown that Gd can be used to adjust mechanical properties with a wide range of alloy compositions and heat treatments because of its large solubility (23.49 wt% at the eutectic temperature) and because of the formation of intermetallic phases, such as Mg_5Gd (see Figure 1.10). As a single alloying element, Gd is present in solid solution and can be used in a concentration-dependent manner to contribute to precipitation strengthening [37].

Mg-based alloys containing REEs show increased mechanical properties [37, 65]. One systematic study was performed by adding gadolinium (Gd) to magnesium in Mg-XGd binary systems where X = 2, 5, 10, and 15 wt%. It was found that increasing the Gd content improved the mechanical properties; however, the study revealed that the addition of this alloying element should be consistent with the corrosion behaviour because the improved corrosion resistance was obtained in the range of 5-10 wt% of added gadolinium (Figure 1.11) [37]. From a biological perspective, there have been reports on the implementation of REEs in anticancer drugs due to their anti-carcinogenic properties [66].

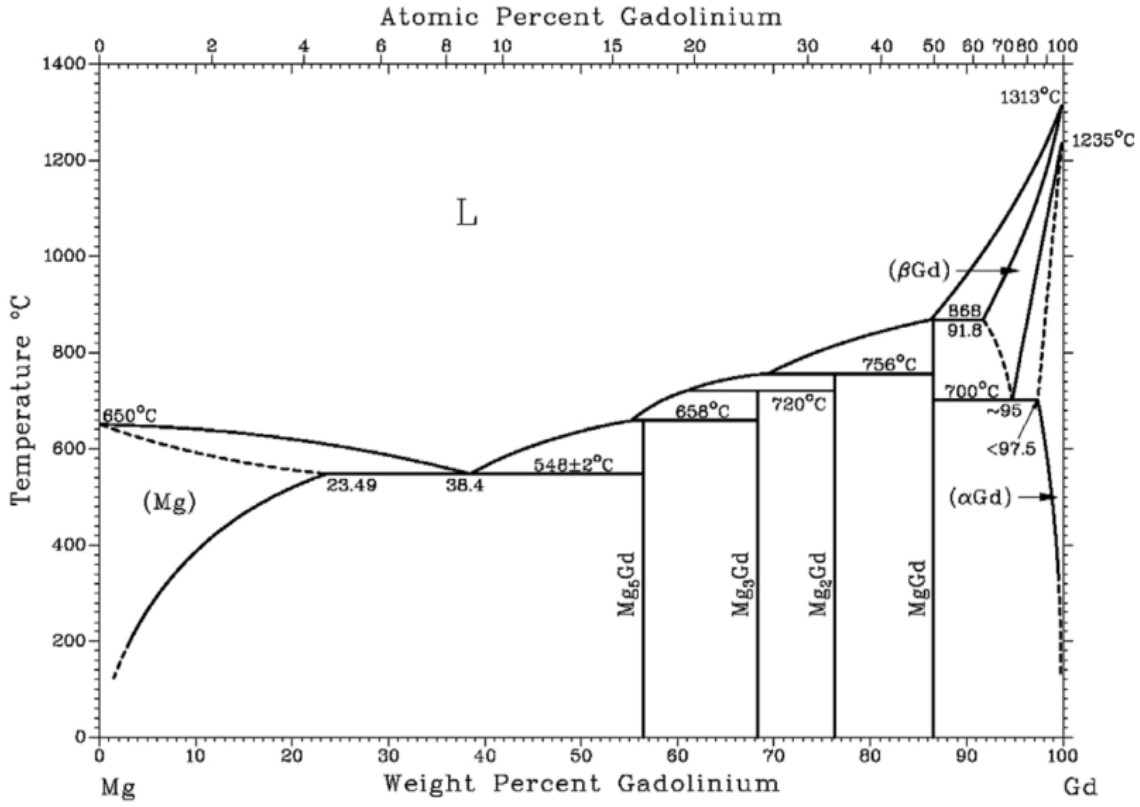

Figure 1.10: Mg-Gd phase diagram *(with permission from Elsevier[37])*.

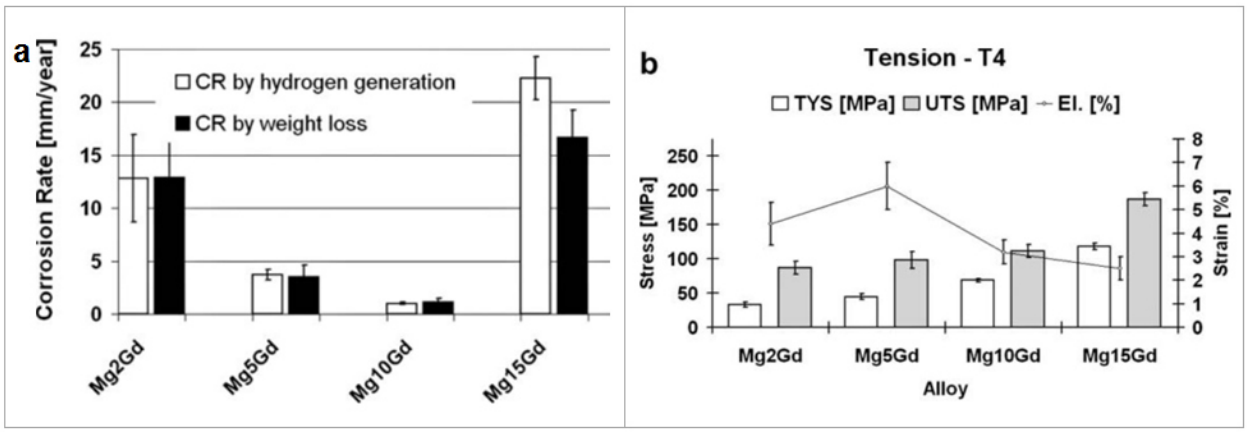

Figure 1.11: (a) Corrosion rate [mm/year] determined by hydrogen evolution and mass loss for binary Mg-Gd alloys as cast materials. The test was performed with a standard eudiometer setup with a total volume of 400 mL and a resolution of 0.5 mL. The immersion was performed in aerated 1% NaCl solution (starting pH 6.5, 21.5 ± 0.5°C, without agitation). **(b)** Ultimate tensile strength (UTS), tensile yield strength (TYS) and Young's modulus (E) for different binary Mg-Gd alloys after a T4 solution heat treatment at 525°C for 24 hours followed by water quenching at 25°C *(with permission from ELSEVIER* [37]*)*.

1.6. The degradation of magnesium from simple testing conditions to complex physiological imitating conditions

The corrosion mechanism of magnesium in water has been well described by the formation of hydroxide and hydrogen gas evolution as follows:

$$Mg_{(s)} + 2\,H_2O_{(aq)} \rightarrow Mg(OH)_{2\,(s)} + H_{2\,(g)} \quad (2)$$

This overall reaction involved the following anodic dissolution of the metal and the reduction reaction (cathodic reaction):

$$Mg_{(s)} \rightarrow Mg^{2+}_{(aq)} + 2\,e^- \text{ (anodic reaction)} \quad (3)$$

$$2\,H_2O_{(aq)} + 2\,e^- \rightarrow H_{2\,(g)} + 2OH^-_{(aq)} \text{ (cathodic reaction)} \quad (4)$$

$$Mg^{2+}_{(aq)} + 2OH^-_{(aq)} \rightarrow Mg(OH)_{2\,(s)} \text{ (product formation)} \quad (5)$$

However, it was found afterwards that degradation in the aqueous environment containing chlorine can increase the degradation of magnesium by inducing pitting corrosion [67]. It was proposed that Cl^- reacted with the solid Mg matrix and the degradation layer, such as $Mg(OH)_2$, according to the equations:

Solid Mg:

$$Mg_{(s)} + 2\,Cl^- \rightarrow MgCl_{2\,(s)} + 2\,e^- \quad (6)$$

$Mg(OH)_2$ layer:

$$Mg(OH)_{2\,(s)} + 2\,Cl^-_{(aq)} \rightarrow MgCl_{2\,(s)} + 2OH^-_{(aq)} \quad (7)$$

Studies then proposed that inorganic constitutes other than Cl^- in the physiological body fluid can directly change or alter the degradation chemical reaction. For example, it was suggested that the presence of HPO_4^{2-}/PO_4^{3-}, HCO_3^-/CO_3^{2-} anions and Ca^{2+} cations can alter the corrosion of magnesium due to phosphate and carbonates precipitations [4]. It has been recommended that more systematic studies should be performed to address the cross-interaction and the influence of the salts in the body fluid on magnesium degradation.

Some studies highlighted that even the selected buffering system in *in vitro* setups can change the degradation of magnesium. For example, it is known that the most commonly used buffering agents include Hepes, Tris-Hcl, and HCO_3^-/CO_3^{2-}. The first two control the pH value by consuming the generated OH^- and can accelerate the degradation of Mg according to the first suggested equation (2) [4].

In terms of body environment complexity, this suggests that the body fluid flow and temperature in various anatomical sites can differently alter the degradation of magnesium (see Figure 1.12) [68]. The normal human physiological temperature, which ranges from 35.8 to 37.2°C, may influence the adsorption of proteins and therefore the response of the biological environment [21]. Concerning the role of proteins on magnesium degradation, there have been several systematic studies on magnesium alloy degradation with different corrosion media ± proteins [69, 70]. It was determined that the composition of the medium itself influenced the degradation behaviour, which was additionally altered by the presence or absence of proteins. Proteins such as albumin have been shown to form a corrosion blocking layer on magnesium alloys in *in vitro* experiments [69-71]. It was found that this layer was enriched by calcium phosphates *in vitro* [69, 71] and *in vivo* [19, 72, 73] and therefore played a protective role [4]. Cells can also alter the degradation of magnesium because they adhere to the material surface and over time proliferate and form an adjacent layer to the degraded surface. This can be considered as a passive influence. However, the active influence of cells on the degradation surface (interface) by changing the chemical composition of the degradation interface has not been widely studied *in vitro*. As described previously, this is related to the complexity of the physiological environment which can even reach a higher level by including cells in the studied system.

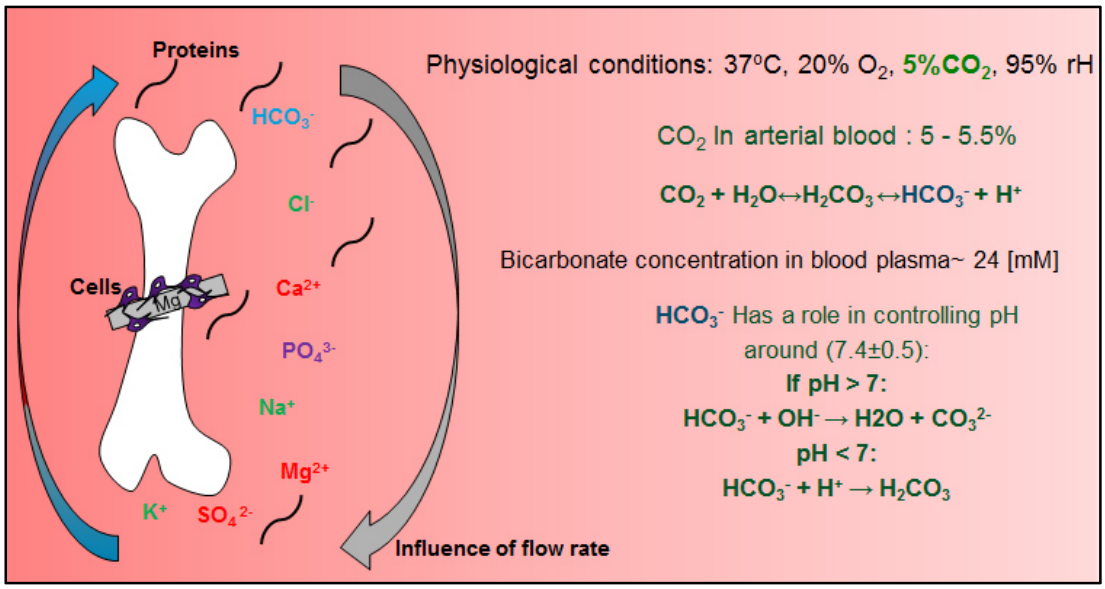

Figure 1.12: Prepared scheme showing the complexity of the physiological conditions under which degradation can be influenced by individual or incorporated parameters, such as temperature and high humidity, body fluid flow, the buffering agent HCO_3^-/CO_3^{2-}, salt composition, proteins, and cells.

1.7. Methods used to determine magnesium degradation rate *in vitro*

In vitro tests utilising physiological conditions are useful for mimicking the *in vivo* corrosion/degradation behaviour of magnesium. Those tests are helpful for material screening, quality control, and the study of degradation mechanisms [4]. The commonly used techniques *in vitro* are electrochemical, hydrogen evolution, and immersion tests [4]. Normative standards, such as the ISO 10993 series, described the test procedures in which an implant is characterised.

Corrosion is an electrochemical process that describes the electron flow between anodes and cathodes. The electron flow represents the rate of oxidisation and reduction at the magnesium/electrolyte interface [4]. Therefore, monitoring the electron flow provides the capability for defining the kinetics of the corrosion process. Two methods, potentiodynamic polarisation and impedance measurements, are commonly used to determine the corrosion rate. However, the corrosion rate of Mg-based BMs obtained from the electrochemical method may be unreliable due to the negative difference effect (NDE) [4, 74].

The hydrogen volume generated from the degradation of magnesium can also be used to calculate the amount of degraded material. This technique enables the study of variation in degradation rates with respect to exposure time. However, caution should be taken in the experiment setup because under the produced *in vitro* physiological environment, contamination with other gases (e.g., CO_2) can happen [4].

Calculating the weight loss to measure bio-corrosion is a simple method in which the sample is placed in the corrosion medium for a period of time. The resultant change in weight is then

measured. The setup is dependent on the experimental variables, such as the choice of buffering system, which by a systematic design of serial experiments can give the individual or combined influence of specific physiological parameters. Prior to measuring the final weight, a cleaning solution, such as diluted chromic acid (usually 180-200 gr/L CrO_3 for 5-10 minutes) is used to remove the corrosion products from the surface without damaging the magneisum substrate. The results from weight loss experiments are typically accurate assuming that the degradation is relatively homogenous, and problems with the removal of the corrosion layer are minimised, and the requirement for multiple replicates improves the confidence in the results. Depending on the design of the experiment, it is possible to combine this method with other *in vitro* measurements, such as pH monitoring, or electrochemical experiments [75] [76].

The corrosion rate by weight loss is calculated by [77]:

$$CR = \frac{W}{A\,t\,\rho} \tag{8}$$

where CR refers to the corrosion rate, W is the calculated weight loss of the samples, A is the exposure area, t is the immersion time, and ρ is the standard density of the studied material.

Determining magnesium degradation under cell interaction in vitro

The methods described previously can be used to study material degradation. However, in this type of degradation study under cells interaction, defining the influence of cells on the material may require a long period of immersion; therefore, performing a weight loss test could be a more favourable strategy. In this case, a sufficient number of samples should be used to allow for sufficient repetitions and statistics. After immersion, the quantification of the degradation products can be performed as previously described by weight loss. In these types of studies, additional parameters might be adjusted and monitored.

Immersion procedure

In this type of material testing in the presence of cells, the immersion medium primarily consists of a suitable cell culture medium with the further addition of serum (e.g., foetal bovine serum) and antibacterial substances (penicillin/streptomycin). It is recommended to perform a pre-incubation, i.e., immersing magnesium samples for sufficient time under standard cell culture condition (CCC; 37°C, 20% O_2, 5% CO_2, 95% rH) without cells. Afterwards, the medium should be changed, and the cells can be added to the system. These methods were recently discussed as a better approach for improving cell adherence, eliminating the strong initial reaction between the material and the surrounding cell-containing environment, and, therefore, preventing the cell death that may result from

osmotic shock [78]. This is important in this type of study, in which cells' influence on the material degradation is being explored. For consistency, the negative control (samples without cells) should be treated with the same pre-incubation procedure. After pre-incubation of the cell samples, cells can be seeded and allowed to adhere for 30 minutes under cell culture conditions. Afterwards, fresh medium is added so the immersion can proceed. Further controls (medium alone and medium with cells) should be included in the experiment layout. Different approaches to perform direct contact test are shown in Figure 1.13.

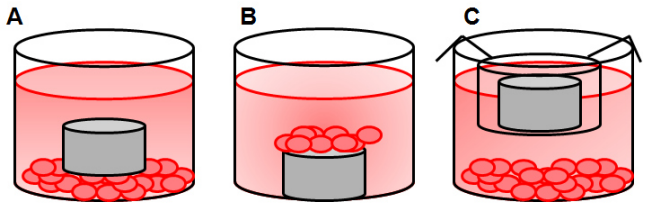

Figure 1.13: Schematic illustration of different experimental approaches for performing direct test to investigate cell-material interactions; A material on cells, B cells on material, C hanging material.

pH and osmolality

To ensure the cell culture and prevent any saturation effect, the immersion medium should be refreshed by medium change, semi-change or circulation. Osmolality should be measured at different time points as should pH, which is an important parameter to monitor during the immersion time. Moreover, pH could be a key factor/parameter in explaining the cells' influence on the material. For example, the cell metabolic activity combined with lactic acid release can change the material dissolution and, therefore, the pH level [79].

Cell viability and morphology

Monitoring cell viability to ensure healthy cell growth and spreading in the presence of degradable magnesium is an important factor whenever cell influence is being investigated. For this purpose, different assays can be applied, such as lactate dehydrogenase (LDH) measurements for cytotoxicity assessments and florescence staining (e.g., Live/Dead staining). Scanning electron microscopy can also be applied to evaluate some interesting points, such as cell surface morphology, cell adhesion contact points and connections.

1.8. Considering the biosafety of the degradation products

The degradation products generated from biodegradable metallic implants may disturb local physiological equilibrium at the implantation site. The release of metal cations in addition to the formation reaction of some degradation products, such as oxides, phosphates, and carbonates, can change the local pH and produce hydrogen gas [4]. Below a certain concentration, these components are tolerable and not harmful to the host. The precipitation of solid metal salts produced by chemical reactions generally shows relatively low solubility

in aqueous solutions [4]. However, those products may show good influence, particularly in bone tissue. For example, $MgCO_3$ is used as a component for bio-glass, and $Mg_3(PO_4)_2$ and $Ca_3(PO_4)_2$ are used for bone cements [4].Theoretically, the detached particles from the biodegradable metal surface may contain pure metal/alloy and intermetallic phases. Those particles should have high degradation behaviour due to their high specific surface area. Therefore, the cytocompatibility and degradability of the intermetallic phase particles should further be examined and considered in biodegradable metallic material design [4]. In the following section, the cytocompatibilities of silver and gadolinium are discussed because those two elements were used for alloying magnesium in this thesis work.

Cytocompatibility of silver:

Silver applications, as silver sulfadiazine (Ag-SD) and silver nanomaterial, for treating external wound infections are well known [60, 61]. The disinfectant properties of silver are used in different biomedical applications, such as endotracheal breathing tubes, urinary catheters, and bone prostheses [80-82].

The principle of silver antibacterial action can be explained by the high bioactivity of the silver ions, which can rapidly penetrate the bacterial membranes and interact with enzymes and other proteins causing cellular distortion and loss of viability [83]. Studies have reported that silver ions interact with sulfhydryl (-SH) groups of proteins as well as the bases of DNA leading to either cell inhibition of respiratory process or DNA unwinding [84].

Silver exists in human tissue only in trace amounts. When overexposure occurs, silver will accumulate in the skin, liver, kidneys, gingiva, mucous membranes, nails and corneas [85]. Soluble silver compounds have the highest potential for causing adverse effects on human health [85]. Acute symptoms caused by overexposure include argyria (silver accumulation in the skin) and argyrosis (silver accumulation in the eyes) [86]. Venugopal and Luckey (1978) reported that argyria can be considered a mechanism for detoxifying silver stored in the tissues by forming less harmful compounds, such as silver-protein complexes and silver sulphide [87]. It has been recommended that silver exposure be limited to 0.01 mg/m^3 in all forms (e.g., metal and soluble compounds) [87].

Cytocompatibility of gadolinium:

Gadolinium is a rare earth element with paramagnetic properties. Its atomic number is 64 [88]. It is one of 15 metallic chemical elements known as the lanthanide series. Lanthanides have been referred to as “bone seekers” because they tend to deposit in bone [89]. Studies have confirmed that gadolinium deposits in bone and remains there for many years [90-93]. Gadolinium Gd^{3+} has an ionic radius that is very similar to that of calcium Ca^{2+}, which is why gadolinium in its ionic form can be toxic in biological systems. It can compete with Ca^{2+} in all

biological systems that require Ca^{2+} for proper function because the trivalent ion binds with much higher affinity [94-97]. Gadolinium was first used in the 1980s as a base contrast agent for MRI and MRA, and , where its paramagnetic properties were used to enhance images of abnormal tissue on magnetic resonance imaging (MRI) scans [98, 99]. Studies have estimated that approximately 1% (15 mg) of the 1.5 g of injected gadolinium from each dose of contrast medium (0.1 mmol/Kg body weight) may be released from the contrast agent and deposited into the patient's bones, including patients with normal kidney function [91, 92]. Although many authors have stated that gadolinium is toxic, the acute toxicity is only moderate. The intraperitoneal LD_{50} dose of $GdCl_3$ was 550 mg Kg^{-1} in mice, whilst $GdNO_3$ induced acute toxicity at concentrations of 300 mg Kg^{-1} in mice and 230 mg Kg^{-1} in rats [100, 101]. Tests regarding the cytotoxicity of Gd in osteoblast-like cells showed that Gd is a suitable element for designing Mg-Gd-based materials for orthopaedic applications when the degradation is carefully controlled by the alloy design. Therefore, the release of Gd ions is in a range in which no negative systemic effects are evoked [42].

1.9. Magnesium degradation types under physiological conditions

The adverse effect of the degradation is the loss of mechanical strength and integrity. In this section, the typical ways in which Mg can corrode in the body environment are presented.

Galvanic corrosion

Galvanic corrosion occurs when two metals with different electrochemical potentials are placed next to each other in the presence of an electrolyte, which provides a pathway for electron transfer (see Figure 1.14). The less noble metal becomes an anode, corrodes and contributes to producing corrosion products. The presence of secondary phases and inter-metallic elements can also induce this type of corrosion [102].

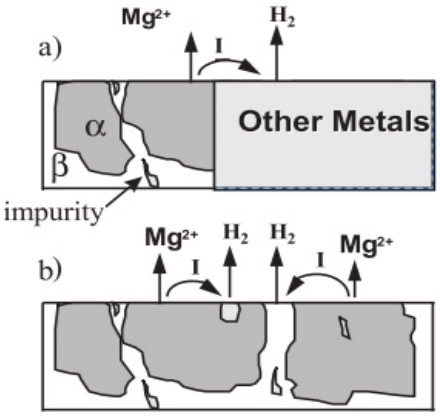

Figure 1.14: Galvanic corrosion resulted from **a**: the contact of dissimilar metals in the presence of an electrolyte (e.g., a magnesium plate with a titanium screw), and **b**: the presence of secondary phases and impurities *(with permission from Wiley* [103]*)*.

Granular corrosion

Intergranular corrosion is generated by the presence of impurities and inclusions that are deposited in the grain boundary regions during solidification. Numerous galvanic reactions take place between the metal matrix and the different impurities and inclusions. However, intergranular corrosion does not occur on magnesium because the matrix (grain) will tend to be anodic whilst their boundaries are cathodic in nature compared to the interior of the grains. The resulting grain boundary corrosion can undercut nearby grains, which subsequently fall out of the matrix [104].

Pitting corrosion

Pitting corrosion occurs from the rapid corrosion of small localised areas that damage the protective surface corrosion layer. This form of corrosion is more serious than the other forms. The pits are small and highly corrosive, and they continue to grow downwards, perforating the metal matrix. After initial nucleation (presence) on the surface, the presence of impurities in the matrix often contributes to further corrosion due to the galvanic differences in the materials [105, 106]. Taking into account the surrounding environment which contains Cl^- , this can accelerate the situation and the pit nucleation. In addition, the mouth of the formed pit is small and eliminates the dilution of the pit contents, which forces and accelerates the autocatalytic growth of the pit. During this process, electrons flowing from the pits make the surface surrounding the pit entrance cathode protected (see Figure 1.15 a). Once pitting starts, the Mg matrix can be completely penetrated within a relatively short period of time, and in the case of a biomedical implant, the load-bearing capacity can be reduced to the point of failure. Another problem related to pitting is the localised increase in stress produced by the pits, which has the potential to form cracks (stress corrosion cracking) [107]. The formation of stress corrosion cracking and metal fatigue cracks in the pits can lead to implant failure during normal loading conditions.

Crevice corrosion

Crevice corrosion is a form of local corrosion that occurs between metal and metal or non-metal components (e.g., a magnesium plate that is fixed in a location by set of screws with a small gap between the screw head and the plate). If the width of the gap is not sufficient to allow the flow of bodily fluids, the low flow will lead to Mg^{2+} ion build up, with a gradient in Mg^{2+} ion concentration, between the entrance and the inside end of the gap, and a corrosion cell will be formed that initiates the attack on the metal components of the implant (see Figure 1.15 b) [102].

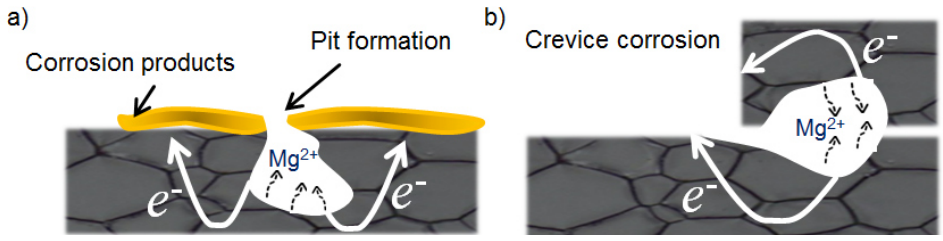

Figure 1.15: Prepared schematics of **a)**: pitting corrosion on magnesium surface and **b)**: crevice corrosion between two magnesium components in a bodily fluid environment.

Fretting corrosion:

Fretting corrosion is the result of damage from metal component that are in direct physical contact with one another in the present of small vibratory surface motions. The micro-motion can be produced by the normal activity of the human body, which results in mechanical wear and metallic debris between the metal component surfaces. Fretting corrosion is common in load-bearing surfaces and is capable of initiating fatigue cracks in the fretting zone. Once a crack is formed, it can propagate into the bulk of the material matrix and lead to implant failure [102].

Erosion corrosion:

Erosion corrosion occurs when the material surface or protecting layer is worn away by the impact of wear debris in the body environment surrounding the implant. The metallic debris can impact the surface of the implant, transfer energy into the region of the collision and plastically deform the surface. During deformation, the surface becomes work hardened to the point where the next impact exceeds the strain required for surface fracturing. Over time, the impact results in materials loss from the material surface [108].

Stress corrosion

Stress corrosion occurs when an electrochemical potential is formed between stressed and unstressed regions of a metal under loading conditions. Consequently, the metal chemical activity increases. The stress effectively initiates the corrosion mechanism, and consequently, the corrosion rate increases by two to three times the normal uniform rate. This usually results in the formation of small cracks within the loaded implant, and those cracks can propagate and extend between the grains throughout the metal matrix [109]. The mechanism is known as stress corrosion cracking (SCC).

Corrosion fatigue

Corrosion fatigue is the result of material being exposed to the combined effect of a cycling load and a corrosive environment. In general, metal fatigue is damage caused by repeated loading and unloading on the implant. The cyclic stress initiates the formation of micro-

cracks on the metal surface and can also damage the protecting layer. Surface imperfections, such as pores and pits from corrosion, can become crack nucleation sites, which can significantly speed up the crack growth rate [102].

1.10. Solubility products of mineral compounds

The precipitation of mineral compounds from an aqueous solution occurs when the aqueous solution is supersaturated with the mineral compound. Compound dissolution takes place when the surrounding aqueous solution is undersaturated with that mineral compound.
The driving forces controlling dissolution and precipitation reactions are related to the respective over/undersaturated levels, and those levels are defined according to the thermodynamic solubility product.

The thermodynamic solubility product describes the equilibrium state between a mineral compound and an aqueous phase. The reaction that controls this equilibrium for single compound AB can be written as [110]:

$$AB\ (S) \leftrightarrow A^{n+}(aq) + B^{n-}(aq) \tag{9}$$

where (S) and (aq) indicate solid and aqueous states, respectively. The rise in Gibbs free energy (ΔG) in equation 9 can be written as:

$$\frac{\Delta G}{RT} = \frac{\mu^{\circ}_{A,\,aq} + \mu^{\circ}_{B,\,aq} - \mu^{\circ}_{AB,s}}{RT} + ln\ I_p^{AB} \tag{10}$$

where μ° is the molar Gibbs free energy under normal conditions of ionic species in solution, $\mu_{AB,s}$ is the Gibbs free energy for the solid compound, R is the gas constant, T is the absolute temperature, and I_p^{AB} is the ionic activity product of the compound AB.

The Ionic activity product of compound AB in aqueous solution is represented as:

$$I_p^{AB} = (A^{n+})(B^{n-}) \tag{11}$$

where (A^{n+}) and (X^{n-}) are the molar activities of cation and anion, respectively. In the state of equilibrium (i.e., $\Delta G=0$), equation 10 can be reduced to:

$$\frac{\mu^{\circ}_{A,\,aq} + \mu^{\circ}_{B,\,aq} - \mu^{\circ}_{AB,s}}{RT} = -\ ln\ I_p^{AB} \equiv -ln\ K_{sp}^{AB} \tag{12}$$

where $\mu^{\circ}_{AB,s}$ is a constant for a pure solid of fixed composition, and μ°_{i} are fixed, by definition, at a determined temperature and pressure. Therefore, the term on the left of equation 12 is also constant. According to this, equation 12 shows that the ionic activity product for compound AB in a saturated aqueous solution must also be constant. This constant is called

the thermodynamic solubility product constant or solubility product constant, which is referred to as K_{sp}^{AB} for the AB compound.

Therefore, by combining equation 12 with equation 10, the general expression would be:

$$\frac{\Delta G}{RT} = ln \frac{I_p^{AB}}{K_{sp}^{AB}} = ln\ S \quad (13)$$

where S is the thermodynamic saturation level. Depending on its value, the following cases can be discussed:

(1) S=1: the aqueous solution is saturated in relation to the compound AB.
(2) S < 1: the aqueous solution is undersaturated, and $\Delta G < 0$. In this state, the reaction in equation 9 will shift to the right, and the solid will tend to dissolve.
(3) S > 1: the aqueous solution will be supersaturated, $\Delta G > 0$, the reaction (in equation 9) will shift to the left, and precipitation or growth of the AB compound will occur.

The calculation of the ionic activity product requires knowledge of the chemical species of the ions in solution. For example, the ionic activity product for a compound with a general composition of A_xB_y is given by:

$$Ip = (A)^x\ (B)^y \quad (14)$$

where (A) and (B) are given by $[A]*f_a$, and $[B]*f_b$, respectively, and f_i is the ionic activity coefficient that depends on the ionic strength of the solution. For example, when the ionic strength of the solution (I < 0.1), the use of the extended Debye-Hückel formula is recommended [111]:

$$-log\ f_i = \frac{A(T)\ z_i^2\ \mu^{1/2}}{1+ B(T)\ a_i\ \mu^{1/2}} \quad (15)$$

where

- A(T) and B(T) are temperature-dependent parameters (e.g., at 25°C, A(T)=0.5114 and B(T)=0.3291);
- z_i is the charge number for the specific ionic component;
- μ is the ionic strength; and
- a_i is the effective diameter of the specific hydrated ions.

2. Motivation and objectives

Defining the *in vitro* setup parameters and their influence on magnesium degradation is an important factor in understanding the degradation mechanisms *in vivo*. The objectives of this thesis work are highlighted in the following points:

1- Identify the influence of important blood plasma salts containing carbonate, calcium, and sulphate on pure magnesium degradation by using a simple salt solution as a basal immersion media and then adding the intended salts.
2- Identify the influence of complex commercial media used in cell culture on the degradation of pure magnesium and compare the results to the findings in (1).
3- Perform the degradation of pure magnesium and two alloys (Mg-2Ag and Mg-10Gd) in a complex environment containing osteoblast cells.
4- Identify the role of osteoblasts in changing the degradation of the studied materials and the effect of material degradation on the metabolic activity of cells.

Although studying the influence of the material microstructure on the degradation is not a primary focus of this thesis work, the microstructure characterisation was performed and briefly discussed in relevance to the obtained results.

3. Materials and Methods

3.1. Material production

The magnesium materials in the study were supplied by Magnesium Innovation Center (MagIC) in Helmholtz-Zentrum Geesthacht (HZG). Pure magnesium and two magnesium-based alloys (Mg-2Ag and Mg-10Gd) were used in the experiments. For casting, pure materials were used, including Mg (99.99%), Gd (99.95%), and Ag (99.99%).

Mg-2Ag was produced by permanent mould gravity casting. After melting the pure Mg, the melt was held at 720°C, and the preheated Ag was added with continuous stirring for 15 minutes. The melt was poured into a preheated (550°C) permanent steel mould using boron nitride (BN) as a mould-release agent.

Mg-10Gd and pure Mg were produced by permanent mould direct-chill casting. In this casting method, the melt was placed into a preheated steel mould, which was placed in a holding furnace at 680°C for another 15 minutes. After the holding time, the mould was slowly immersed in running water to solidify the ingot. BN was used as a mould-release agent.

During the casting process, a cover gas was used (2 wt% SF_6 in Ar mixture). The alloys were then homogenised with a T4 heat treatment in an Ar atmosphere at 550°C (Mg-10Gd) or at 420°C (Mg-2Ag) for 6 h prior to extrusion. The concentrations of Mg, iron (Fe), copper (Cu), and nickel (Ni) on the cast materials were determined by spark emission spectrometry (Spectrolab M, Spektro, Germany), and the concentrations of Ag and Gd were determined by X-ray fluorescence spectrometry (Bruker AXS S4 Explorer, Bruker AXS GmbH, Germany) (see Table 3.1). Afterwards, the materials were indirectly extruded (Strangpreßzentrum Berlin, Berlin, Germany). The extrusion parameters are shown in Table 3.2. Different processing parameters in casting and extrusion were applied due to the diversity of materials and to achieve similar microstructures in the final product. Discs (10 mm in diameter and 1.5 mm thick) were machined from the extruded bars (Henschel KG, Munich, Germany). Samples were sonicated in ethanol for 20 minutes and then sterilised by gamma radiation at a dose of 29.2 KGy (BBF GmbH, Stuttgart, Germany). For material characterisation, the discs were embedded in plastic cold-curing resin. Powder and liquid Demotec 30 were mixed at a 1:1 ratio. The plastic resin took approximately 15 minutes to solidify at room temperature. The samples were ground using silicon carbide emery paper of up to 2500 grit. Afterwards, they were polished with a lubricant containing 1-µm diamond particles (Schmitz-Metallographie GmbH, Herzogenrath, Germany) and 0.05-µm colloidal silica (OPS; Cloren Technology GmbH, Wegberg, Germany); etched in an etching solution composed of 30 mL deionised water, 140 mL ethanol, 7 mL glacial acetic acid (J.T baker, Center Valley, USA), and 8 g picric acid (Sigma-Aldrich, Taufkirchen, Germany); quickly washed with ethanol; and

dried with blowing hot air. Micrographs were taken using an optical microscope (Reichert-Jung (Leica) MeF3, Wetzlar, Germany) with a digital camera. The grain size was determined by the line intercept method according to ASTM E112 [112].

Table 3.1: The chemical compositions of the studied materials.

Alloy	Chemical composition wt%					
	Ag	Gd	Fe	Cu	Ni	Mg
Mg	-	-	0.0042	0.0021	0.0006	Bal.
Mg-2Ag	2.4	-	0.0048	0.0017	0.0007	Bal.
Mg-10Gd	-	10.5	0.0029	0.0048	<0.0036	Bal.

Table 3.2: The extrusion parameters for pure Mg, Mg-2Ag, and Mg-10Gd rods.

Alloy	Extrusion parameters					
	Type	Extrusion ratio	Speed [mm/sec]	Extr.T [°C]	BilletT [°C]	d_{final} [mm]
Mg	Indirect	1:84	0.7	300	340	12
Mg-2Ag	Indirect	4:25	2.5	370	370	12
Mg-10Gd	Indirect	4:25	3.5	370	430	12

3.2. Immersion procedures

The immersion procedures differed based on the experimental objectives. The procedures are described according to their appearance sequence in this thesis as follows:

Influence of specific inorganic salts on magnesium degradation

To track the influence of inorganic salts, HBSS (Life Technologies, Darmstadt, Germany), a simple salt solution with no calcium and magnesium additions, was used as a base solution for all immersion media with 10% fetal bovine serum (FBS, PAA laboratories, Linz, Austria) as the protein supplement. Three important salts, sodium bicarbonate ($NaHCO_3$), calcium chloride ($CaCl_2$), and magnesium sulphate ($MgSO_4$), were added in concentrations close to those in human blood plasma and the cell culture medium Dulbecco's modified Eagle's medium (DMEM) [113] (see Table 3.3 for the media formulations).

Twelve immersion media were prepared based on HBSS and can be classified into four groups according to the each specific inorganic salt addition.

A. $NaHCO_3$ (Sodium-hydrogen carbonate, Merck, Darmstadt, Germany)

(1) Base solution (BS): HBSS + 10% FBS

(2) BS + 1150 mg/L $NaHCO_3$

(3) BS + 3350 mg/L $NaHCO_3$

B. $CaCl_2$ (Calcium Chloride-Dihydrate, Fluka, Germany)

(4) BS + 264 mg/L $CaCl_2$

(5) BS + 1150 mg/L $NaHCO_3$ + 264 mg/L $CaCl_2$

(6) BS + 3350 mg/L $NaHCO_3$ + 264 mg/L $CaCl_2$

C. $MgSO_4$ (Magnesium Sulphate-Heptahydrate, Merck, Darmstadt, Germany)

(7) BS + 200 mg/L $MgSO_4$

(8) BS + 1150 mg/L $NaHCO_3$ + 200 mg/L $MgSO_4$

(9) BS + 3350 mg/L $NaHCO_3$ + 200 mg/L $MgSO_4$

D. *$MgSO_4$ + $CaCl_2$*

(10) BS + 264 mg/L $CaCl_2$ + 200 mg/L $MgSO_4$

(11) BS + 1150 mg/L $NaHCO_3$ + 264 mg/L $CaCl_2$ + 200 mg/L $MgSO_4$

(12) BS + 3350 mg/L $NaHCO_3$ + 264 mg/L $CaCl_2$ + 200 mg/L $MgSO_4$

Ten samples were immersed in 2 mL/sample of each immersion medium for 72 and 240 hours under cell culture conditions (37°C, 20% O_2, 5% CO_2, 95% rH). Samples were placed on the surface of a well plate, and the immersion medium was changed every 3 to 4 days to enable a semi-static immersion test. pH and osmolality were measured during each medium exchange.

Influence of the cell culture media salt composition on magnesium degradation

Different media were used, including Hank's Balanced Salt Solution with no calcium and magnesium addition (HBSS); Dulbecco's Modified Eagle's Medium (DMEM; Life technologies, Darmstadt, Germany); and Roswell Park Memorial Institute medium (RPMI-1640; Sigma-Aldrich, Taufkirchen, Germany). All media were supplemented with 10% fetal bovine serum (FBS) and 1% penicillin/streptomycin (P/S; Invitrogen, Darmstadt, Germany). The inorganic salt concentrations of the immersion media compared to blood plasma are shown in Table 3.3.

Six samples were immersed in 2 mL of the immersion medium under cell culture conditions for total immersion times of 3 and 14 days. The immersion medium was changed every 3 to 4 days to enable a semi-static immersion test and prevent the saturation effect.

Table 3.3: Inorganic salt concentrations in HBSS, DMEM Glutamax, RPMI, and blood plasma (*in vivo* reference). Components of interest are highlighted in red when the difference with the *in vivo* condition exceeds 50%.

Concentration [mM]	HBSS	DMEM Glutamax	RPMI- 1640	Blood plasma
Bicarbonate	4.2	44.1	23.8	24.4
Calcium	-	1.80	0.4	2.5
Chloride	143.3	117.5	108.0	103
Magnesium	-	0.81	0.4	0.8
Potassium	5.8	5.3	5.4	4.4
Phosphate	0.8	0.9	5.6	1.3
Sulphur	-	0.8	0.4	1.1
Sodium	142.4	155.3	137.0	137.5
	In vitro			*In vivo*

Analysing the degradation interface of magnesium alloys under osteoblast cell interaction

Dulbecco's Modified Eagle's Medium with 10% fetal bovine serum and 1% penicillin/streptomycin was used as a cell culture and immersion medium. Samples were pre-incubated for 24 h under cell culture conditions. The medium was then changed, and cells were cultured directly on upper surface of the discs. This protocol has been reported to improve cell adhesion, exclude the strong initial reaction between the material and medium, and prevent cell death from osmotic shock [78]. This is important in our study because the direct cell influence on degradation is the aim. Systematically, the samples without cells (samples with no cells: **SNCs**) were treated in the same way as the samples with cells (samples with cells: **SCs**) by following the same pre-incubation procedure. After the pre-incubation of the **SCs**, 100,000 human primary osteoblasts were applied on the samples' top surfaces and allowed to adhere for 30 min in the incubator (Heraeus, Langenselbold, Germany). The medium was then added to continue the immersion. In addition, medium control (**MC**), and cell control (**CC**) were added to the experimental layout. The isolation of primary human osteoblasts was performed according to the Declaration of Helsinki as described previously [114]. Human hip joints were obtained from patients undergoing hip arthroplasty (Hospital Eilbek, Hamburg, Germany) with the approval of the local ethics committee. Briefly, cancellous bone material was removed from the hip joint bone with bone rongeurs in pieces of about 5mm diameter. Bone marrow and non-bone components are removed by thoroughly vortexing in phosphate buffered solution (PBS) repeatedly for 30 seconds, with continuous replacement of the PBS. After the bone fragments had received a

white, ivory-like appearance they were cultures in DMEM with 10% FBS, 1% penicillin/streptomycin for about 10 days without medium change. Thereafter medium was changes every2-3 days. Passaging was done at approximately 90% confluence. For this study, osteoblasts were used up to the third passage [114].

To clarify the role of osteoblasts in mediating a mineralisation action, a fibroblasts L929 mouse cell line (Sigma-Aldrich, Taufkirchen, Germany) was used as a cell control. The same protocol described previously was used for the immersion procedure.

3.3. Degradation rate by weight loss method

Before sample sterilisation, the initial weight of the samples was recorded. After immersion, the formed products were removed by treating the corroded disk with chromic acid (180 g/L in distilled water, VWR international, Darmstadt, Germany) for 20 min at room temperature. The degradation rate (DR) was calculated in mm/year using the equation:

$$DR = \frac{8.76\ 10^4\ \Delta g}{A\ t\ \rho} \quad (1)$$

where Δg is the weight change in grams, A is the surface area of the sample in cm^2, t is the immersion time in hours, and ρ is the density in g/cm^3.

3.4. pH and osmolality measurement

The pH and osmolality of the immersion media were measured initially and during the immersion time. Six samples were used at each time point for each condition.

The pH was measured with a SENTRON ARGUS X pH-meter (Fisher Scientific GMBH, Schwerte, Germany). The pH measurement concept is based on the Nernst equation. The electrode of the SENTRON table pH meter is a non-glass pH electrode (MicroFET; SENTRON ARGUS X pH-meter, Fisher Scientific GMBH, Schwerte, Germany), where a hydrogen ion-selective field effect transistor (ISFET) is used.

The online pH measurements were performed using the SDR sensorDish reader system (PreSens GmbH, Regensburg, Germany). Special 24-well plates were used with an integrated pH sensor (HydroDish, preSens GmbH, Regensburg, Germany). The measurement method is based on non-invasive luminescence detection (see Figure 3.1). The measureable pH in this system ranges from five to nine. Prior to changing the medium, pH was measured after shaking with the table pH meter to compare and check the validity of the online pH measurement.

Osmoality was measured with the Osmomat 030 (Gonotec, Berlin, Germany). The concept of measurement is based on comparing the freezing point of pure water with that of different solutions. Whilst water has a freezing point of 0°C, a solution with a saline concertation of 1 Osmol/kg has a freezing point of -1.858°C.

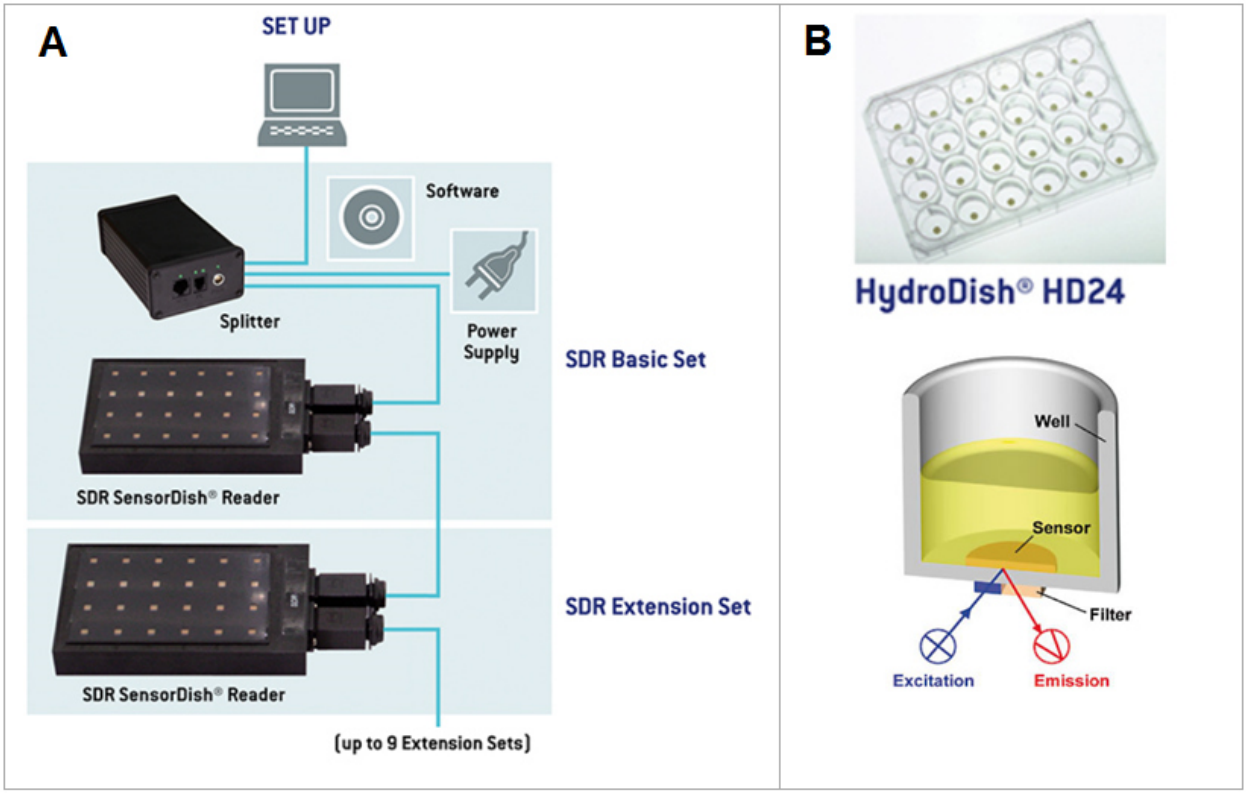

Figure 3.1: Online pH measurement method. **(A)** The setup and its connections. **(B)** The pH multidish and the concept by which the pH is measured. *(Courtesy of PreSens GmbH, Regensburg, Germany).*

3.5. Element concentrations in the immersion media

The concentrations of calcium, magnesium and phosphorous in the extract were measured with inductive coupled plasma spectroscopy (ICP-MS, Agilent 7700x, Agilent Technologies, California, USA) against external 3-point-calibration.

The concept of the measurement is based on converting the atoms of the element in the sample to the ions by a high temperature ICP (inductively coupled plasma) source. These ions enter the mass-spectrometer, where they are separated by their mass-to-charge ratio and are then detected by a suitable detector that translates the number of ions striking it into an electrical signal. This signal can be measured and related to the number of atoms of that element in the sample using calibration standards.

The samples of the immersion media were diluted with ultrapure water (18.2 MW cm, Millipore, Darmstadt, Germany) and acidified with 2% (v/v) nitric acid that was sub-boiled prior to use (Sigma-Aldrich, Hamburg, Germany). Calibration standards were prepared from single-element standards (1000 mg/L, CPI-International, California, USA). An internal standard solution was added online during the measurement. Accuracy of the calibration was checked by measuring an independent multi-element standard (CMS-5, Inorganic Ventures, Virginia, USA).

3.6. Chemical analysis on the sample cross-section after immersion

3.6.1. Sample preparation

The Mg discs treated in different immersion media were cut in half using a precision diamond wire saw (Well Walter Ebner, Switzerland). One half of each dry sample was then embedded in resin (Reckli Injektionsharz, Reckli GmbH, Herne, Germany) with the cross-sections oriented upwards and subsequently polished with 0.1-μm colloidal silica suspension at the final stage of fine polishing. This sample preparation method allows for the analysis of the distribution of chemical species across the outermost oxidised layer of magnesium samples by applying infrared microspectroscopy and electron-induced x-ray emission spectroscopy. At the same time, it ensures stress-free sample handing (i.e., there were no artificially induced mechanical cracks in the samples), and the possibility for chemical alteration of the examined area was excluded. The only plausible contamination may come from the silica nanoparticles used for final polishing, but SiO_2 was not detected by either of spectroscopic methods used to study the interface layer.

3.6.2. X-ray Diffraction XRD

The non-embedded half from each sample was subjected to powder x-ray diffraction (XRD) in reflection mode (X'Pert diffractometer, Philips & Co., Eindhoven, Netherlands, Cu Kα radiation) to check the compositions of the potentially formed crystalline compounds. X-ray diffraction is based on the fact that the interaction of the incident x-rays with the sample produces constructive interference when conditions satisfy Bragg's law. These diffracted x-rays are then detected, processed and counted. Conversion of the diffraction peaks to d-spacings allows the identification of the mineral because each mineral has a set of unique d-spacings. This is achieved by comparison with the standard reference patterns [115].

3.6.3. Fourier Transform infrared (FTIR) microspectroscopy

The FTIR method relies on the fact that most molecules absorb light in the infrared region of the electromagnetic spectrum. This absorption corresponds specifically to the bonds present in the molecule. The frequency range is measured as wave numbers and is typically within the range of 4000-600 cm^{-1}. The background emission spectrum of the IR source is first recorded, followed by the emission spectrum of the IR source with the sample in place. The ratio of the sample spectrum to the background spectrum is directly related to the sample's absorption spectrum. The resulting absorption spectrum from the bond natural vibration frequency indicates the presence of various chemical bonds and functional groups in the sample [116, 117].

The polished cross-sections of the samples were subjected to FTIR reflection miscrospectroscopy performed with a Bruker Equinox55 FTIR spectrometer equipped with a

LN2-cooled MCT detector and an A590 infrared microscope with 15 x objectives (Bruker Optics, Ettlingen, Germany). The spectra were recorded in back scattering geometry with an instrument resolution of 2 cm^{-1}, and by taking the average of 512 scans. The background single-channel signal was measured from an aluminium mirror. The used aperture of the IR beam restricted the spatial area from which the spectra were collected to a circle with a diameter of 60 µm. The measured spectra were compared to reference IR reflection spectra collected from brucite ($Mg(OH)_2$), whewellite ($CaC_2O_4 \cdot H_2O$), struvite ($MgCO_3$), and hydroxyapatite ($Ca_5(PO_4)_3OH$), enamel and bone), which are biominerals that can be formed under mild conditions simulating those in the human body.

3.6.4. Electron-induced X-ray emission spectroscopy

Backscattered electron (BSE) imaging, chemical element mapping, and electron microprobe analysis on the cross-sections of corroded Mg discs were performed using a Cameca Microbeam SX100 electron microscope (Cameca, Gennevilliers Cedex, France) equipped with a wavelength and energy dispersive system, an accelerating voltage of 15 kV and a beam current of 20 nA. The mapping was conducted for carbon (C), nitrogen (N), oxygen (O), sodium (Na), calcium (Ca), phosphorus (P), sulphur (S), chlorine (Cl), and potassium (K) with a lateral spatial size of 0.1 µm and a detection limit in the range 100-300 ppm. Electron microprobe analysis (EPMA) to quantify the content of oxides in wt% was attempted in at least 25 points from each sample with a lateral resolution of ~1 µm. The standards used were albite for Na, MgO for Mg, apatite for P, $BaSO_4$ for S, vanadinite for Cl, orthoclase for K, and andrandite for Ca. The carbon content could not be quantitatively determined by this method because of the necessity to coat the sample surface with a conductive layer of carbon. The principle of EMPA is based on focusing accelerated electrons on the sample surface using a series of electromagnetic lenses. These energetic electrons produce characteristic x-rays within a small volume (1 to 9 cubic microns) of the sample. The characteristic x-rays are then detected at particular wavelengths, and their intensities are measured to determine concentrations. Elements (except H, He, and Li) can be detected because each element has a specific set of x-rays [118, 119].

3.7. Scanning electron microscope and energy dispersive x-ray measurements on the sample surface

A scanning electron microscope (SEM) is a high magnification microscope that uses a focused scanned electron beam to produce images of the samples, where the primary electrons generate low-energy secondary electrons that tend to emphasis the topographic nature of the specimen. Primary electrons can also be backscattered, producing images with a high degree of atomic number contrast.

Ionised atoms can relax by electron shell-to-shell transitions, which lead to either x-ray emission or Auger electron ejection. The x-rays emitted are characteristic of the elements in the top few µm of the sample. Characteristic x-rays are identified via a detector using their unique energies or wavelengths to ascertain the composition of the sample [118, 119]. In EDX, a solid-state detector collects and counts all emitted x-rays at once, divides the energy spectrum into different channels or ranges, and displays it on the computer screen. Peaks will show up on the spectrum that correspond to the energies of elements present in a sample [118, 119].

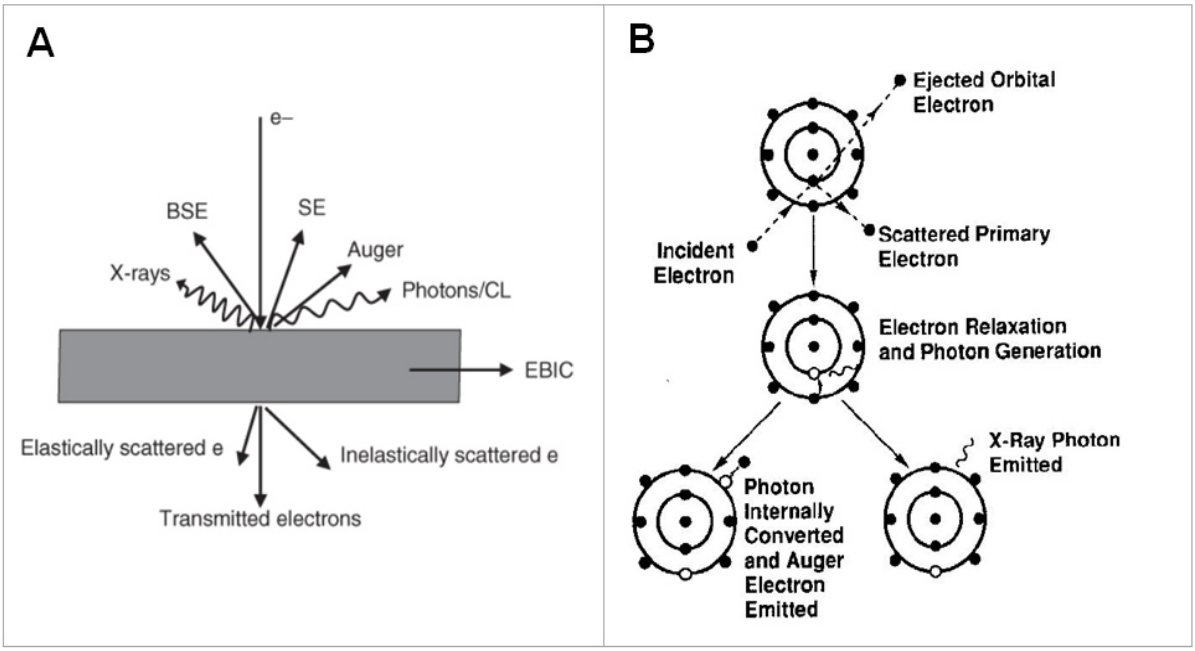

Figure 3.2: A: Overview of the signal generated when an electron beam interacts with a relatively thin specimen (in the case of a thick specimen, there are no transmitted electrons and the signal is absorbed within the material). B: The production of the characteristics x-rays *(with permission form Wiley* [118]*).*

The SEM and EDX measurements were used in this thesis work for the following objectives.

Element distribution on the degraded surface

The SEM and EDX measurements were obtained by Phenom ProX desktop SEM (Phenom-World BV, Eindhoven, Netherlands). Chemical element mappings of the pure magnesium sample surfaces after 3 and 14 days of immersion were performed at 15 kV. The EDX was realised with 8 regions of interest in the respective EDX spectrum: C, N, O, Na, Mg, P, Ca and Cl.

Cell adhesion and morphology

Samples were prepared by first fixing them overnight with 2.5% glutaraldehyde (Sigma-Aldrich, Steinheim, Germany). Cells were then stained with 1% osmium tetroxide (Sigma-

Aldrich, Taufkirchen, Germany) for 0.5 h. Next, subsequent dehydration steps with 35%, 60%, 80%, and 100% isopropanol were performed, and the samples were dried by critical point drying (Leica EM CPD030, Wetzlar, Germany) to reach a water-free state. The concept of critical point drying is that the organic solvent is replaced by liquid CO_2 at a pressure of 50 bar and a temperature of 8°C. After the complete replacement, the chamber is heated, resulting in increased pressure due to evaporating CO_2. After reaching the critical point, the pressure is released very slowly, and a dry sample is obtained [120]. Dry samples were mounted on aluminium stubs, and SEM images were taken by Zeiss Ultra 55 (Carl Zeiss GmbH, Oberkochen, Germany) scanning electron microscope with low voltage (2kV with the SE2 detector).

Degradation interface of Mg-2Ag, Mg-10Gd, and pure magnesium in the presence and absence of osteoblast cells

Samples were prepared by the critical point drying as described previously. Measurements were obtained by an Auriga (Zeiss, Oberkochen, Germany) and the Energy Dispersive X-ray Spectroscopy (EDX) device Apollo XP from EDAX (Ametek GmbH, Wiesbaden, Germany). SEM images were taken at 2 kV accelerating voltage with the SE2 detector. Cross-sections of the samples were prepared by ion beam milling at 30 kV using a gallium-focused ion beam (FIB) attached to the Auriga. To prevent damage to the cells and the degradation layer and to obtain a precise cutting along the degradation layer, a layer of platinum was deposited by the Gas-Injection-System (GIS) on the surface. Five EDX line scans were performed directly after FIB milling at 15 KV to define the vertical element distribution of the degradation layer on the cross-sections. EDX was realised with 8 regions of interest in the respective EDX spectrum (C, N, O, Na, Mg, P, S and Ca) complemented by the alloying elements of the respective sample (Ag and Gd). Each degradation layer cross-section was analysed. To obtain a high counting rate for the EDX analysis, an SEM aperture of 120 µm in diameter was used in high current mode.

3.8. Cell viability by LIVE/DEAD (viability/cytotoxicity) staining assay

Cell coverage and viability was analysed by using LIVE/DEAD (Life technologies, Darmstadt, Germany) assay. Three samples were used from each material at 4 and 14 days of immersion time. The staining solution was prepared by adding 4 µL Calcein AM (live) and 10 µL Ethidium homodimer-1 (dead) to 10 mL of PBS. Samples were washed first with phosphate buffered solution (PBS) to eliminate non-adherent cells and then immersed with 1.5 mL/sample of staining solution under cell culture conditions for 20 minutes. Afterwards, the staining solution was replaced by DMEM, and samples were visualised by fluorescent microscopy (Nikon, eclipse Ti, Düsseldorf, Germany). The filters used included Fluorescence

Isothiocynate; FITC (Ex: 465-495 nm; Em: 515-555 nm; Mirror at 505 nm) and Texas red (Ex: 540-580 nm; Em: 600-660 nm; Mirror at 595 nm).

The principle of this method is that live cells are distinguished by the presence of ubiquitous intracellular esterase activity. This activity can be determined by the enzymatic conversion of the virtually nonfluorescent cell-permeant Calcein AM to the intensely fluorescent Calcein. The polyanionic dye Calcein is retained within live cells, producing an intense uniform green fluorescence in live cells (EX/EM ~495 nm/~515 nm). EthD-1 enters cells with damaged membranes and undergoes a 40-fold enhancement of fluorescence upon binding to nucleic acids, producing a bright red fluorescence in dead cells (EX/EM ~495 nm/~635 nm). EthD-1 is excluded by the intact plasma membrane of live cells. The determination of cell viability depends on these physical and biochemical properties of cells, and it can be calculated by:

$$Viability\ (\%) = \frac{\left(\frac{live\ cells}{live\ cells + dead\ cells}\right)_{sample}}{\left(\frac{live\ cells}{live\ cells + dead\ cells}\right)_{control}} \times 100 \quad (2)$$

3.9. Cytotoxicity assessment by measuring Lactate Dehydrogenase (LDH)

An LDH cytotoxicity detection kit (Roche Diagnostic GmbH, Mannheim, Germany) was used to measure the LDH activity release from the damaged cells to the medium based on a colorimetric method. The principle is that the LDH activity is determined in an enzymatic way. First, NAD^+ is reduced to $NADH/H^+$ by the LDH catalysed conversion of lactate to pyruvate. Second, the catalyst (diaphorase) transfers H/H^+ from $NADH/H^+$ to the tetreazolium salt, which is reduced to formazan. Therefore, the amount of colour formed in the assay is proportional to the damaged cells. This assay indicates the damage to the plasma membrane of cells induced by the degradation of the studied materials. The measurements were obtained at 1, 2, 3, 7, and 14 days of incubation. A standard curve was prepared for each measured 96-well plate to quantify the LDH in the extract. The standard curve was generated by adding L-lactate dehydrogenase (L-LDH) from a bovine heart (Sigma-Aldrich, Steinheim, Germany) to the used immersion medium, and this solution was then serially diluted to obtain a gradual series of concentrations. The controls consisted of medium alone and samples without cells. In addition, cells alone were used as a “low control” (i.e., low or normal LDH release) and cells with Triton X-100 (Sigma-Aldrich, Steinheim, Germany) were used as a “high control” (i.e., high LDH release) at each measured time point. The assay consisted of adding 100 µL of these samples, standards, and controls to 100 µL of the substrate buffer. The samples were then incubated in the dark at room temperature for 20 minutes, and the absorbance was measured at 490 nm with a reference at 620 nm using a SUNRISE absorbance reader (Tecan GmbH, Grailsheim, Germany).The cytotoxicity was calculated according to the following formula:

$$Cytotoxicity\ (\%) = \frac{experiment\ value - low\ control}{high\ control - low\ control} \times 100 \quad (3)$$

3.10. Double staining for bone mineralisation (Osteo-Image) and cell DNA (DAPI)

The Osteo-Image (Lonza, Walkersville, USA) was used as a specific stain for hydroxyapatite (HA). Three samples per condition, **SC** (samples with cells), **SNC** (samples with no cells), **CC** (cells control), and **MC** (medium control) were used to identify the possibility of HA precipitation under cell culture conditions and to evaluate the mineralisation matrix deposition based on the differentiated osteoblasts on each alloy. The L929 mouse fibroblast cell line was used as a cell control to assess the role of osteoblasts in changing the chemistry of the degradation interface by mediating HA precipitation. The staining protocol started with removing the plate from the incubator and allowing it to reach room temperature (RT). The medium was then removed, and the discs were washed once with PBS. The samples were subsequently fixed with 3.7% formaldehyde (Sigma-Aldrich, Taufkirchen, Germany) at RT for 20 minutes and then washed twice with Osteo-Image wash buffer (diluted 1:10 in deionised water). One millilitre of the staining reagent (diluted 1:100 in staining reagent dilution buffer) was added to each sample, and the mixture was incubated at RT for 30 minutes in the dark. The staining reagent was then removed, and the samples were washed three times with wash buffer. The samples were analysed under a fluorescence microscope with a FITC filter. To obtain an image of the entire disc, large images (6 x 6) with 4x magnification and a 5% overlap between the acquired images were collected. To visualise the cell-HA distribution, **SC** and **CC** samples were also stained with DAPI (4´,6-Diamidino-2-Phenylindole Dihydrochloride) (Sigma-Aldrich, Taufkirchen, Germany). Following the protocol, 5 mg of the reagent were first dissolved in 10 mL of doubled distilled H_2O. Subsequently, 100 µL of this solution was added to 9.9 mL of methanol (Promochem, LGC standards GmbH, Wesel, Germany) to obtain the working solution. Each sample was immersed in 1 mL of the working solution and incubated for 15 min at 37°C in the dark. The samples were analysed by fluorescence microscopy with a DAPI filter (Ex: 340-380 nm; Em: 435-485 nm; Mirror at 400 nm).

The Osteo-Image staining was evaluated by quantifying the mineralisation matrix shown in the large images in monochromatic mode (FITC) using ImageJ software [121]. The images were converted to binary images and then segmented by histogram thresholding to isolate the stained areas. The amount of staining in the image was measured in area percentage.

3.11. Solubility calculations

Following simple solubility concepts, the possibility of precipitation was calculated for four different Ca-PO_4 phases in the immersion medium at a pH of 8.3 (as a random specified value), and pCO_2= 0.05 atm. The used concepts are explained in detail in the bibliography

[111, 122, 123]. Briefly, the ionic strength of the immersion medium was calculated and used for an estimation of the activity of the specified anions and cations according to the extended Debye-Hückel formula for ionic activity because DMEM as used immersion medium has an ionic strength of 0.15 mol/L. The ionic activity product (I_{AP}) was then calculated for each specific phase and used to calculate the thermodynamic saturation level (S). This parameter represents a direct measure of the thermodynamic driving force for the precipitation of the particular phase. It is calculated by:

$$ln\frac{I_{Ap}}{K_{sp}} = ln\ S \qquad (4)$$

where I_{AP} is the ionic activity product, K_{sp} is the solubility constant at 37°C, and S is the saturation level.

A saturation index is defined by:

$$SI = log(S) \qquad (5)$$

3.12. Statistics

Statistical analyses were performed using the SigmaStat package (Systat software GmbH, Erkrath, Germany; version 11.0). Standard analyses comparing more than two conditions were conducted by using one way analysis of variance (ANOVA). The tests used are mentioned with the experiment results.

4. Results

4.1. Microstructure characterisation of the studied materials

Discs of pure mg, Mg-2Ag and Mg-10Gd with diameters of 10 mm were analysed in terms of grain size, optical microstructure and grain distribution (Figure 4.1).The optical microstructures of all materials showed similar grain-size distribution for the disc surfaces (transverse direction of extrusion), indicating homogenous material and complete recrystallization after extrusion. Mg-2Ag displayed the largest average grain size at 37±19 µm compared to Mg-10Gd at 31±17 µm and pure Mg at 30±15.

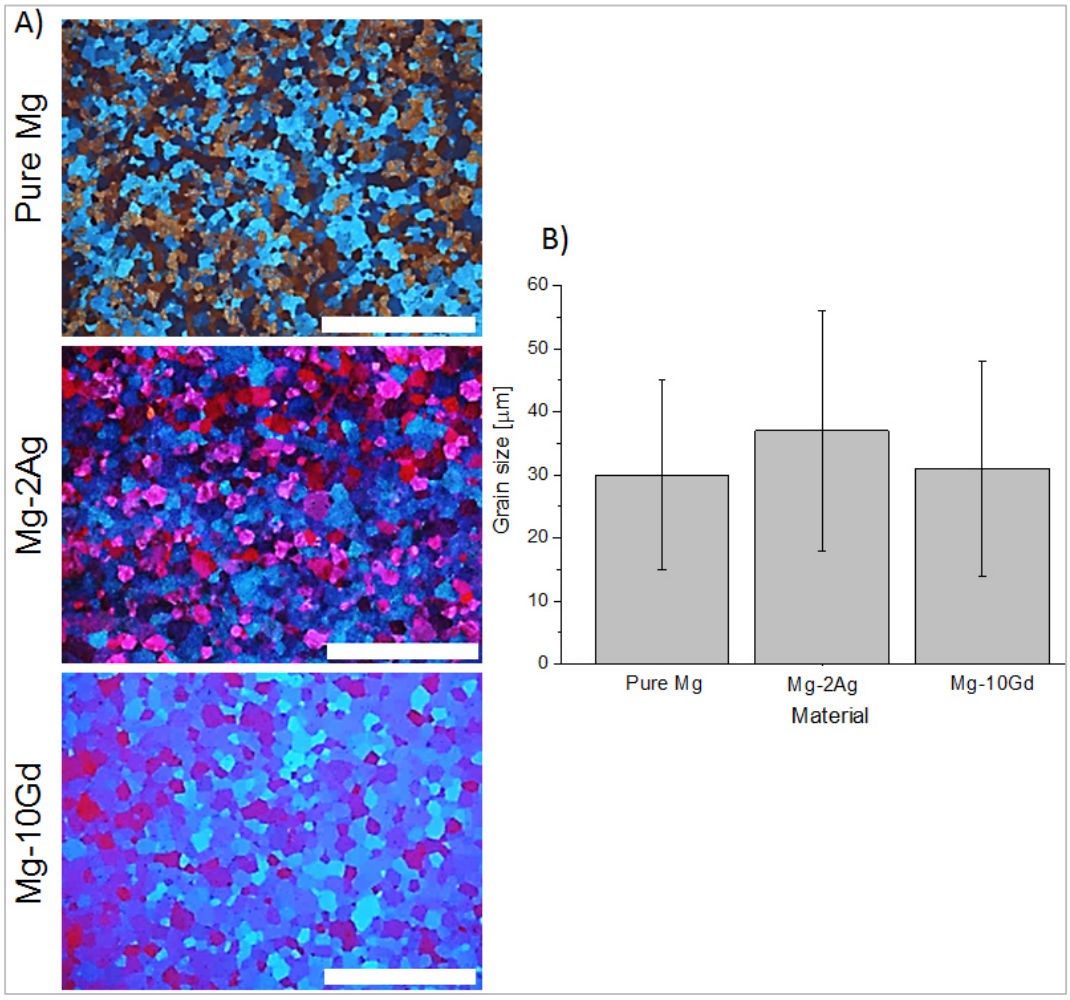

Figure 4.1: A) The optical microstructures of the discs surface detected by an optical microscope equipped with a digital camera. **B)** The estimated average grain sizes of pure Mg, Mg-2Ag, and Mg-10Gd. Scale bars represents 500 µm.

4.2. Influence of salt composition on magnesium degradation

The experiments in this section are divided into two aspects

(1) Define the influence of salt constitutes on magnesium degradation using HBSS as a simple salt solution and then adding each specific salt first individually and then with other salts (following the bottom-up concept). For this, calcium chloride, magnesium sulphate, and sodium bicarbonate salts were chosen

(2) Study the influence of two cell culture media other than HBSS (Table 2.1) on magnesium degradation and compare the resulting effects. The results in this section should confirm the findings in section 1 and address the influence of the distinctive high phosphorous concentration in RPMI

4.2.1. Salt constitutes' influence on pure magnesium degradation

In this section the influence of three salts was studied. Samples were labelled according to the conditions as following:

A. $NaHCO_3$

(1) Base solution (BS): HBSS + 10% FBS
(2) BS + 1150 mg/L $NaHCO_3$
(3) BS + 3350 mg/L $NaHCO_3$

B. $CaCl_2$

(4) BS + 264 mg/L $CaCl_2$
(5) BS + 1150 mg/L $NaHCO_3$ + 264 mg/L $CaCl_2$
(6) BS + 3350 mg/L $NaHCO_3$ + 264 mg/L $CaCl_2$

C. $MgSO_4$

(7) BS + 200 mg/L $MgSO_4$
(8) BS + 1150 mg/L $NaHCO_3$ + 200 mg/L $MgSO_4$
(9) BS + 3350 mg/L $NaHCO_3$ + 200 mg/L $MgSO_4$

D. *$MgSO_4$ + $CaCl_2$*

(10) BS + 264 mg/L $CaCl_2$ + 200 mg/L $MgSO_4$
(11) BS + 1150 mg/L $NaHCO_3$ + 264 mg/L $CaCl_2$ + 200 mg/L $MgSO_4$
(12) BS + 3350 mg/L $NaHCO_3$ + 264 mg/L $CaCl_2$ + 200 mg/L $MgSO_4$

Degradation rate, pH and osmolality

The calculated degradation rate after 72 and 240 hours are shown in Figure 4.2 A. The comparison between the two immersion times shows that within uncertainties, the weight loss for each sample is in the same range at both time points. This can be further observed in Figure 4.2 B, which shows that common points between these two immersion times exceeded 60% of the total significant points measured by ANOVA on ranks with Dunn's multiple comparison post hoc test. The pH value and osmolality were measured at each medium exchange point (see Table 4.1 and Figure 4.3). A general trend was observed with an initial increase in the pH value as the degradation began and then reached saturation after 144 hours. Figure 4.2 shows that adding $MgSO_4$ alone seemed to have a negligible effect on the degradation process (compare samples 1-7, 2-8, and 3-9 in Figure 4.2). $NaHCO_3$ had a stronger effect than $MgSO_4$. Osmolality gradually increased with the increase in the $NaHCO_3$ concentration (see Figure 4.3 A) and the presence of $NaHCO_3$ in a relatively high concentration slightly increased the degradation rate (compare samples 1-2-3 in Figure 4.2). The degradation process was most strongly influenced by $CaCl_2$. Figure 4.2 clearly shows that the presence of $CaCl_2$ significantly reduced the degradation rate. In addition, the presence of $CaCl_2$ reduced the influence on the surrounding environment during immersion, as seen in Figure 4.3 B.

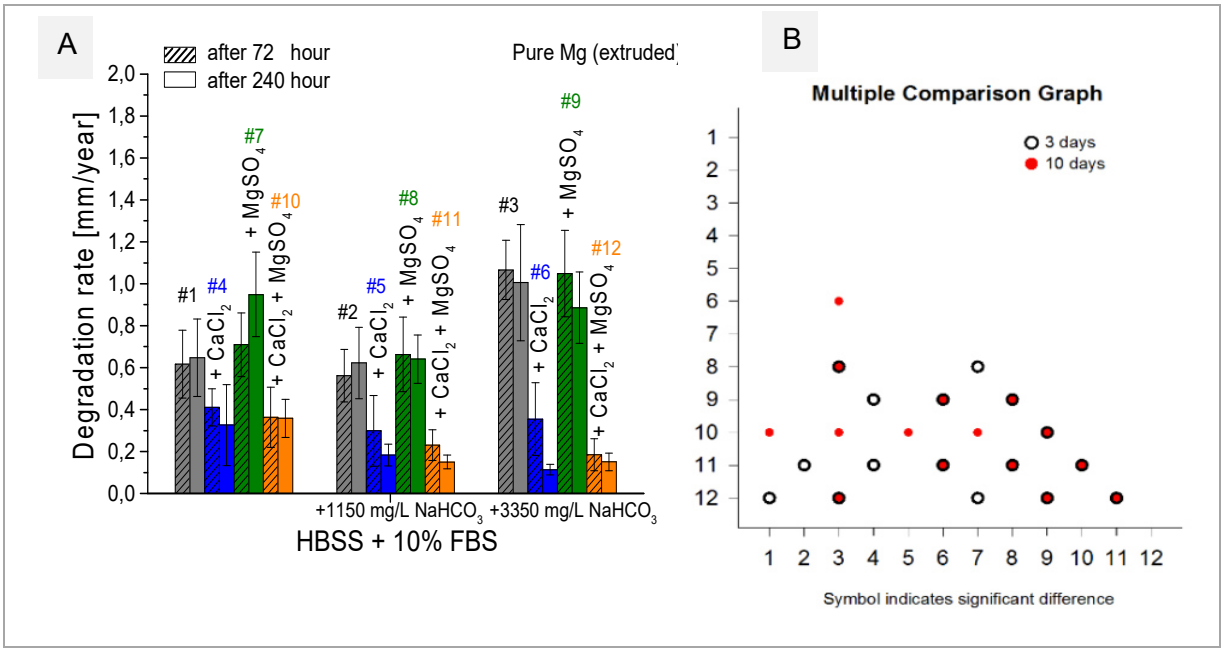

Figure 4.2: (A) shows the degradation rate [mm/year] after immersion for 72 and 240 h in the immersion media under cell culture conditions. The numbers over the columns represent the condition numbering in text. The basic solution is HBSS + 10% FBS. **(B)** presents the multiple comparison graph between the different conditions at the same time point. Common points between the two immersion times (72 and 240 hours) exceeded 60% of total significant differences measured by ANOVA on ranks with Dunn's multiple comparison post hoc test (significance level = $P<0.05$).

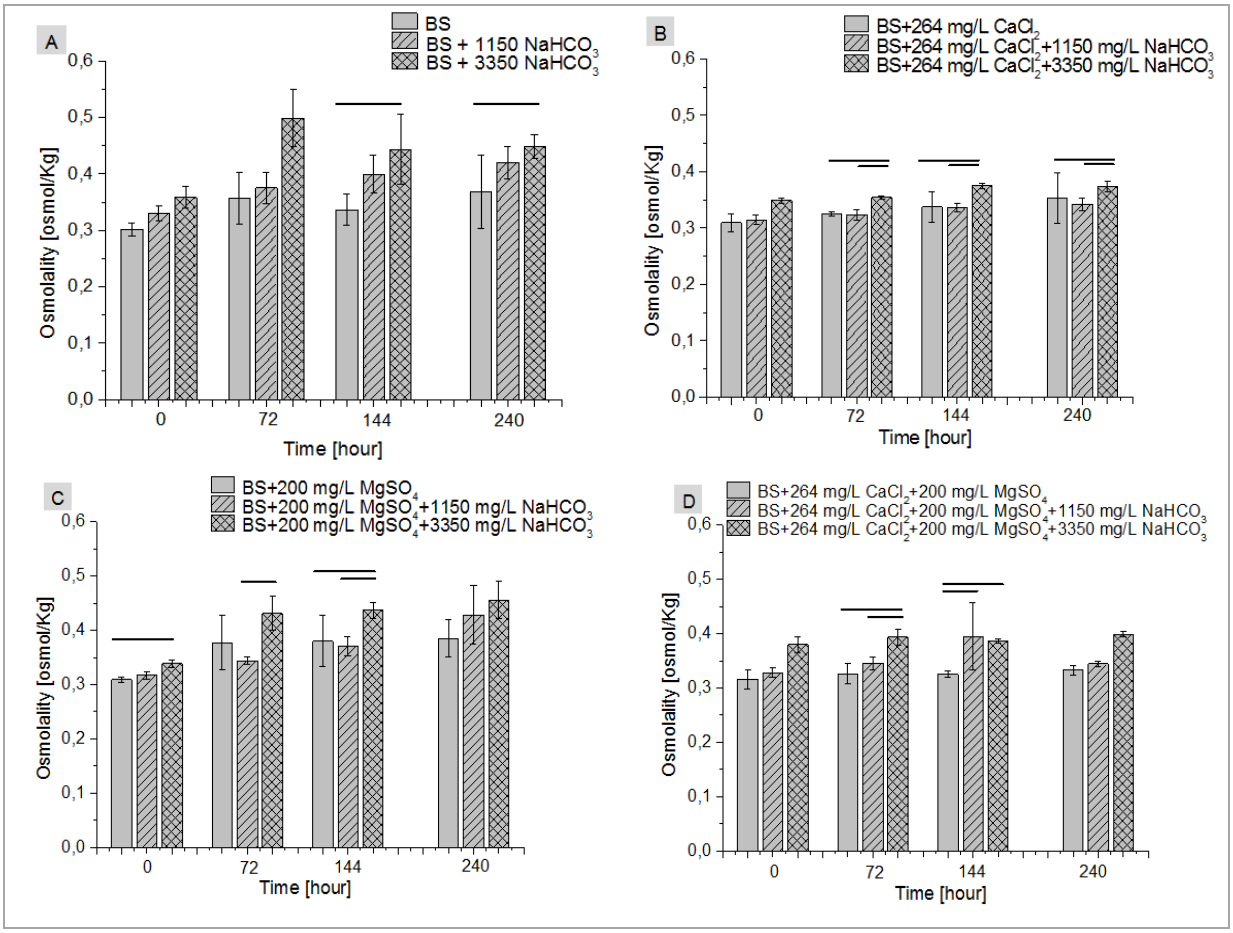

Figure 4.3: Osmolality measurements during 240 hours of immersion under cell culture conditions. BS refers to the basic formulation medium for all conditions (HBSS + 10% FBS). Significant differences between the immersion conditions at the same time point are marked by lines (ANOVA on ranks with Dunn's multiple comparison post hoc test; significance level $P < 0.05$).

Table 4.1: pH values of immersion media before (0 h) and after immersion of Mg discs for 72, 144, and 240 h. The basic solution for all conditions was HBSS + 10% FBS (standard deviation < 0.05 are not shown).

Immersion media		0 h	72 h	144 h	240 h
1	Basic solution (HBSS + 10% FBS)	7.8	8.6 ± 0.3	9.1 ± 0.4	8.8 ± 0.3
2	Basic solution + 1150 mg/L $NaHCO_3$	8.4	8.7 ± 0.2	9.0	9.0
3	Basic solution + 3350 mg/L $NaHCO_3$	8.6	8.7 ± 0.2	8.9 ± 0.1	8.9 ± 0.1
4	Basic solution + 264 mg/L $CaCl_2$	7.8	8.3 ± 0.2	8.5 ± 0.2	8.4 ± 0.1
5	Basic solution + 1150 mg/L $NaHCO_3$ + 264 mg/L $CaCl_2$	8	8.5 ± 0.2	8.1 ± 0.1	8.3 ± 0.1
6	Basic solution + 3350 mg/L $NaHCO_3$ + 264 mg/L $CaCl_2$	8.3	8.5 ± 0.1	8.2	8.2 ± 0.2
7	Basic solution + 200 mg/L $MgSO_4$	8.0	8.5 ± 0.3	8.9 ± 0.2	8.9 ± 0.1
8	Basic solution + 1150 mg/L $NaHCO_3$ + 200 mg/L $MgSO_4$	8.2	8.9 ± 0.4	8.7	8.7 ± 0.1
9	Basic solution + 3350 mg/L $NaHCO_3$ + 200 mg/L $MgSO_4$	8.4	9.0 ± 0.2	8.6 ± 0.1	8.7 ± 0.1
10	Basic solution + 264 mg/L $CaCl_2$ + 200 mg/L $MgSO_4$	8	8.4 ± 0.1	8.9 ± 0.1	9.0 ± 0.4
11	Basic solution + 1150 mg/L $NaHCO_3$ + 264 mg/L $CaCl_2$ + 200 mg/L $MgSO_4$	8.2	8.4 ± 0.1	8.5	8.6 ± 0.1
12	Basic solution + 3350 mg/L $NaHCO_3$ + 264 mg/L $CaCl_2$ + 200 mg/L $MgSO_4$	8.6	8.8±0.1	8.7	8.7±0.1

Element concentration in immersion media

Table 4.2 shows the concentrations of Ca, P, and Mg in the immersion media after three days of immersion. The effect of the different inorganic salts on the element concentrations was easily observed. In the absence of $CaCl_2$, both $MgSO_4$ and $NaHCO_3$ had similar effects on the degradation rate, with both increasing the Mg concentration by ~30 mM and reducing the Ca and P concentrations by ~0.2 mM and ~0.6 mM, respectively. In comparison, $CaCl_2$ had a lower effect on Mg concentration, which is related to the lower degradation rate. However, after 72 hours, the amount of calcium was highly reduced (by 0.6-0.8 mM), whereas the reduction of P was lower (0.1-0.4 mM) than that observed for solutions without calcium (0.4-0.7 mM).

Table 4.2: ICP-MS results for the concentrations of Mg, Ca, and P in the immersion medium before and after 72 h of immersion. The basic solution for all conditions was HBSS+ 10% FBS.
*concentrations calculated according to concentrations provided by formulation data sheets
** measured data

Condition		Initial*			72 hours**		
		Mg [mM]	Ca [mM]	P [mM]	Mg [mM]	Ca [mM]	P [mM]
1	Basic solution (HBSS + 10% FBS)	-	0.3	0.8	17.9	0.1	0.4
2	Basic solution + 1150 mg/L $NaHCO_3$	-	0.3	0.8	35.3	0.1	0.1
3	Basic solution + 3350 mg/L $NaHCO_3$	-	0.3	0.8	34.6	0.1	0.1
4	Basic solution + 264 mg/L $CaCl_2$	-	2.1	0.8	9.8	1.3	0.4
5	Basic solution + 1150 mg/L $NaHCO_3$ + 264 mg/L $CaCl_2$	-	2.1	0.8	11.4	1.2	0.4
6	Basic solution + 3350 mg/L $NaHCO_3$ + 264 mg/L $CaCl_2$	-	2.1	0.8	6.8	1.5	0.7
7	Basic solution + 200 mg/L $MgSO_4$	0.8	0.3	0.8	37.9	0.1	0.1
8	Basic solution + 1150 mg/L $NaHCO_3$ + 200 mg/L $MgSO_4$	0.8	0.3	0.8	58.4	0.1	0.2
9	Basic solution + 3350 mg/L $NaHCO_3$ + 200 mg/L $MgSO_4$	0.8	0.3	0.8	42.4	0.1	0.2
10	Basic solution + 264 mg/L $CaCl_2$ + 200 mg/L $MgSO_4$	0.8	2.1	0.8	13.7	1.1	0.4
11	Basic solution + 1150 mg/L $NaHCO_3$ + 264 mg/L $CaCl_2$ + 200 mg/L $MgSO_4$	0.8	2.1	0.8	8.0	1.5	0.4
12	Basic solution + 3350 mg/L $NaHCO_3$ + 264 mg/L $CaCl_2$ + 200 mg/L $MgSO_4$	0.8	2.1	0.8	8.0	1.5	0.5

Chemical element mapping, XRD, FTIR and EMPA of the corroded layer

All samples were subjected to chemical element mapping (Figures 4.4-4.7), FTIR microspectroscopy (Figure 4.8), and electron microprobe analysis (Table 4.3). The detected amounts of K and N were negligible for all samples (< 0.01 wt%), and therefore, the corresponding data are not shown in Figures 4.4-4.7 and 4.11 or in Tables 4.3 and 4.5. It should be noted that although HBSS does not contain calcium or sulphur, these two elements were detected in the interface layer of all samples due to fact that FBS contains low concentrations of both elements.

The XRD patterns obtained from all samples surface consisted primarily of an amorphous halo and for some samples, of a few very broad low-intensity diffraction peaks, indicating

that the formed layers are amorphous and/or contain nanocrystallites that are insufficiently large to be detected by in-house XRD equipment.

Samples immersed in BS + x $NaHCO_3$, x = 0, 1150, and 3350 mg/L

As expected, the interface layer is rich of oxygen, and the content of Mg is reduced (see Figure 4.4). All three samples contain carbon in the interface layer, as shown by both element mappings (Figure 4.4) and the IR reflection spectra (Figure 4.8a). In addition, the IR spectroscopic data indicate that carbon is derived from carbonate rather than from oxalate. The predominance of Mg over Ca and Na (see Table 4.3) shows that the phase is $MgCO_3$. The total oxide values of the samples exposed to BS and BS + 3350 mg/L $NaHCO_3$ correspond well to the value of $MgCO_3$ expected to be detected by EMPA, whereas that of the sample immersed in BS + 1150 mg/L $NaHCO_3$ is lower, which is likely due to the high porosity of the interface layer. The presence of two IR reflection peaks arising from the longitudinal optic (LO) and transverse optic (TO) components of the CO_3 stretching mode is typical of crystalline carbonate phases, while a single IR peak due to the TO component in the IR reflection spectra measured in backscattering geometry is characteristic of amorphous carbonate phases. Therefore, the IR data in Figure 4.8a suggest that the layer formed after immersion in BS + 1150 mg/L $NaHCO_3$ is predominantly amorphous, while the other two samples also exhibit crystalline $MgCO_3$. The sample exposed to BS + 1150 mg/L $NaHCO_3$ differed from the samples exposed to BS and BS + 3350 mg/L $NaHCO_3$ in the higher content of phosphate (see Table 4.3 and Figure 4.8a). The CaO/P_2O_5 ratio, however, does not match that of apatite, suggesting that this sample contains predominantly magnesium phosphate and/or calcium phosphate of another structure type.

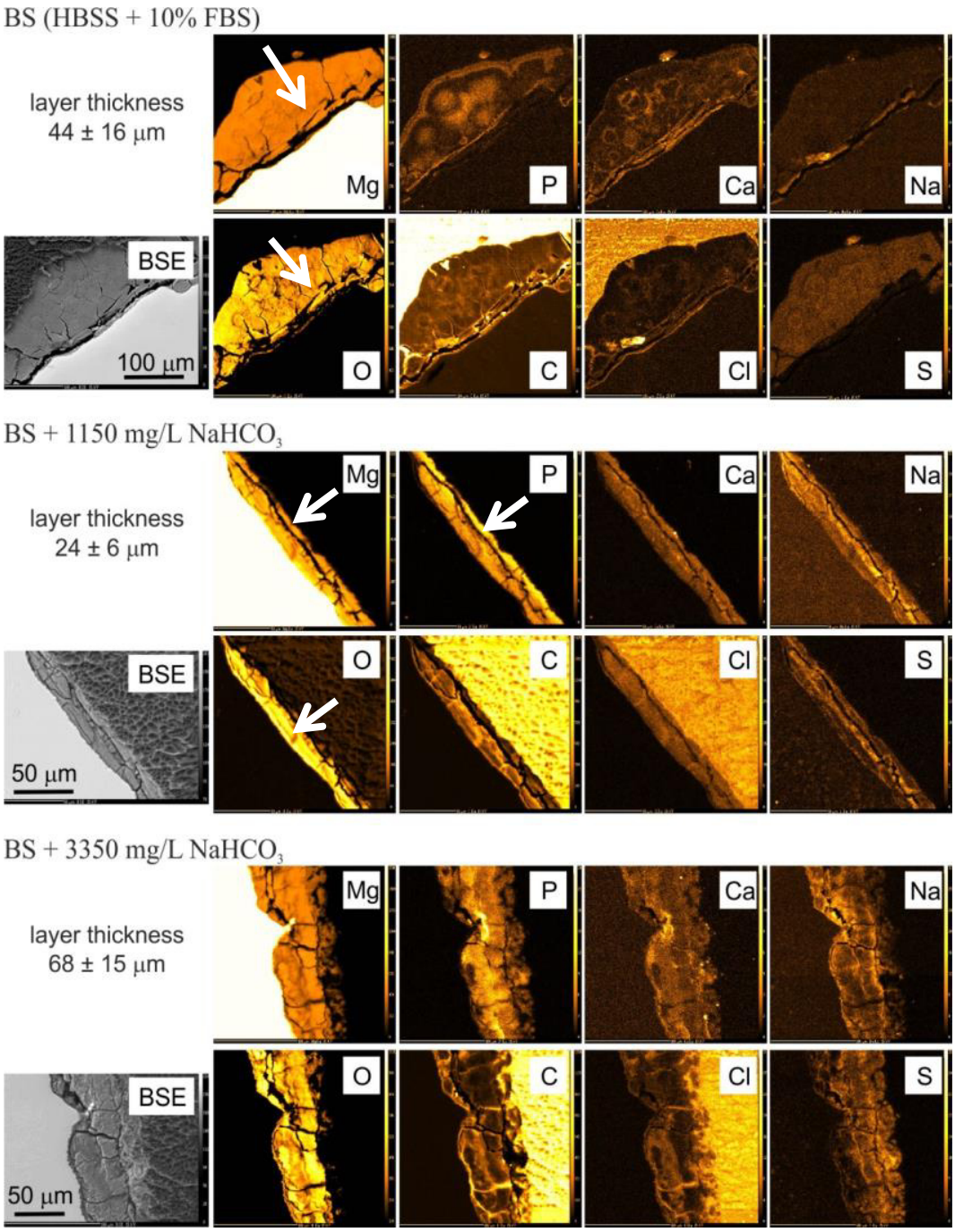

Figure 4.4: Backscattered electron (BSE) images and chemical element mappings of Mg immersed in basic solution (BS) with different concentrations of $NaHCO_3$. The corresponding values of the interface layer thicknesses are averaged over 50 readouts across each sample. The scale of mappings is the same as that of the corresponding BSE images. The non-corroded bulk of the Mg discs appears brightest in the BSE images, the outer corroded layers appear greyish, and the darkest parts of the BSE images correspond to the resin in which the cross-section cuts were embedded. Arrows in the figure in the case of 1150 mg/L $NaHCO_3$ indicate layer richness with Mg and O, and P.

Samples immersed in BS + 264 mg/L CaCl2 + x NaHCO3, x = 0, 1150, and 3350 mg/L

Overall, these samples exhibited a thinner interface layer (Figure 4.5) compared to BS + *x* $NaHCO_3$ (Figure 4.4), which is consistent with the $CaCl_2$-induced reduction of the degradation rate (Figure 4.2). The interface layer of all three samples immersed in BS + 264 mg/L $CaCl_2$ + x $NaHCO_3$ contained amorphous $MgCO_3$ (see Figure 4.8b) and phosphate (Figure 4.8b and Table 4.3). Within the uncertainties, the CaO/P_2O_5 ratio is closer to that of apatite, suggesting that the formed phosphate phase can be apatite-type. The element mappings (Figure 4.5) revealed a zonation of the interface layer in respect to P and Ca for *x* = 0 and 1150 mg/L $NaHCO_3$, with the outer rim being richer in those two elements than the inner rim of the layer.

Samples immersed in BS + 200 mg/L $MgSO_4$ + x $NaHCO_3$, x = 0, 1150, and 3350 mg/L

The interface layers formed in the presence of $MgSO_4$ were in general thicker (see Figure 4.6) than those formed in the above-discussed solutions (Figures 4.4 and 4.5). The degradation layer showed heterogeneous morphology and pits features, which were observed for all samples immersed in $MgSO_4$-containing media (see Figures 4.6 and 4.7). This was less pronounced when $CaCl_2$ was present in the immersion media, likely because of the opposite protecting effect of Ca. In the case low concentration (*x* = 0, and 1150 mg/L) of $NaHCO_3$, the addition of $MgSO_4$ to the basic solution enhanced the formation of phosphate on the account of carbonate phases (Figure 4.8c and Table 4.3). The CaO/P_2O_5 ratio (Table 4.3) suggests the presence of magnesium phosphate rather than apatite-type calcium phosphate in the interface layer. However, for high concentration of $NaHCO_3$ (*x* = 3350 mg/L), both IR reflection spectroscopy (Figure 4.8) and EMPA (Table 4.3) revealed that the chemistry of the interface layers with and without $MgSO_4$ were the same and were dominated by $MgCO_3$.

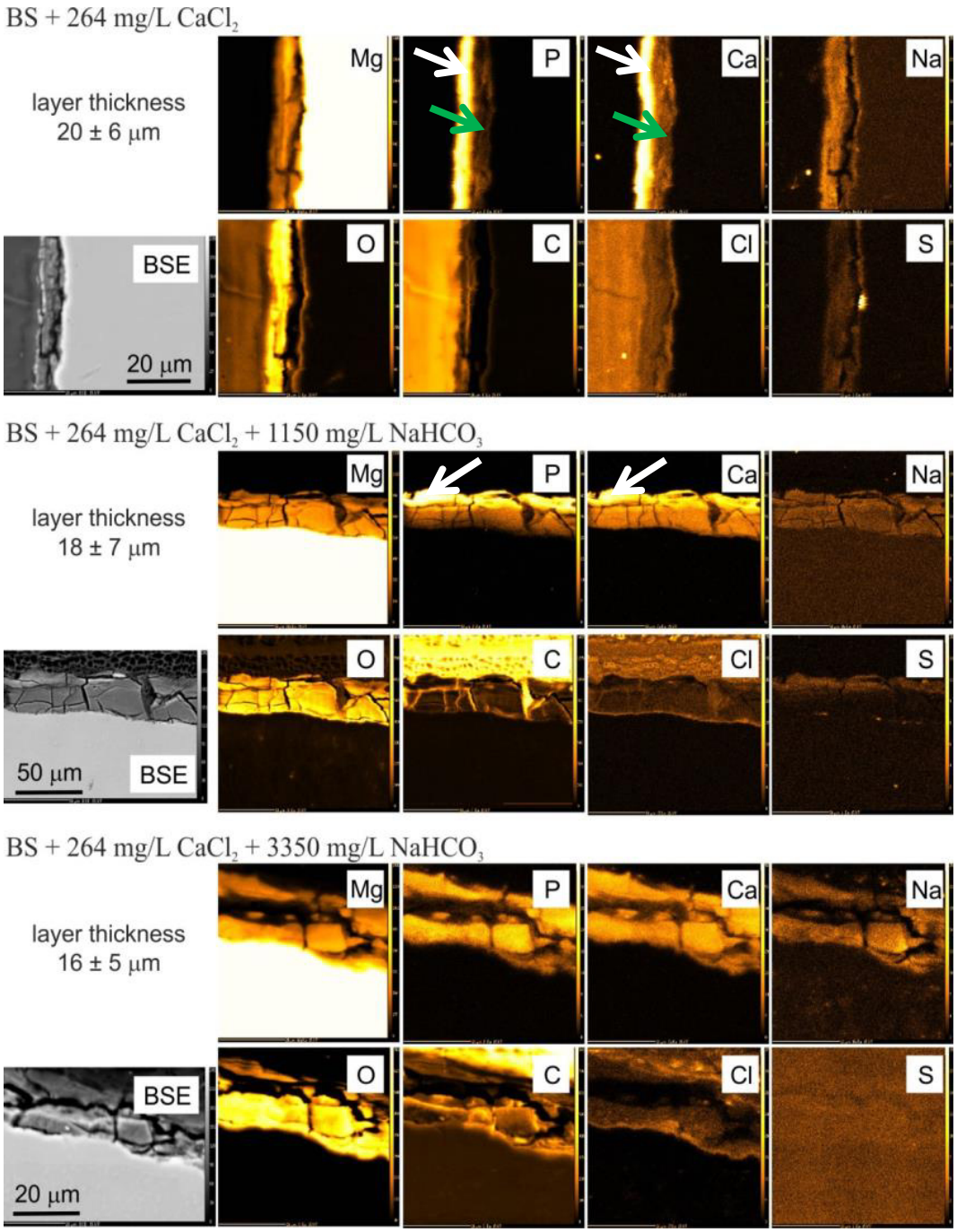

Figure 4.5: Backscattered electron (BSE) images and chemical element mappings of Mg immersed in basic solution (BS) with different concentrations of $NaHCO_3$ in the presence of $CaCl_2$. The arrows in the figures refer to the zonation in the degradation interface and to the corresponding Ca and P precipitations.

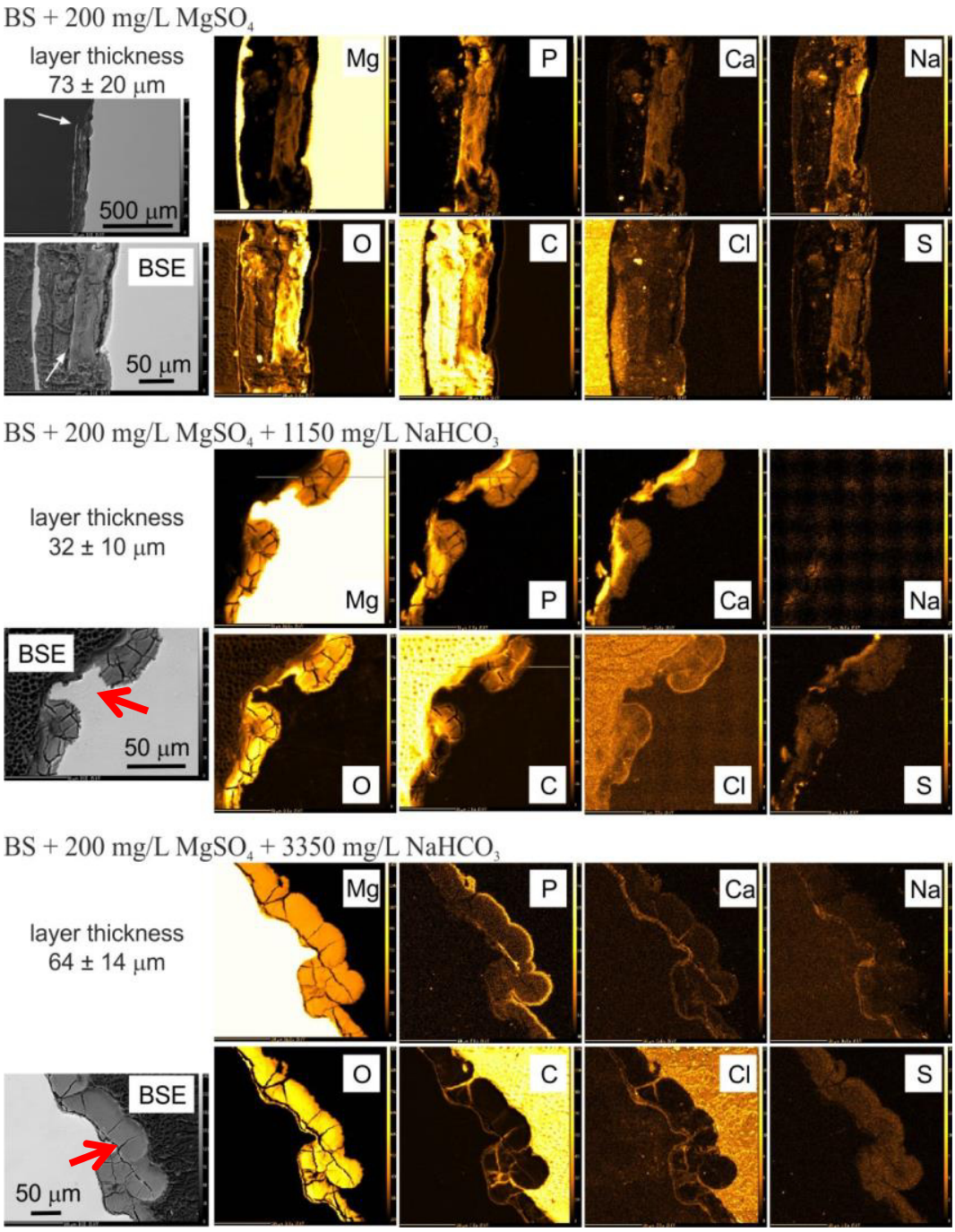

Figure 4.6: Backscattered electron (BSE) images and chemical element mappings of Mg immersed in basic solution (BS) with different concentrations of $NaHCO_3$ in the presence of $MgSO_4$. The arrows in the figure indicate pit formation and heterogeneous degradation morphology.

Samples immersed in BS + 264 mg/L $CaCl_2$ + 200 mg/L $MgSO_4$ + x$NaHCO_3$, x = 0, 1150, and 3350 mg/L

As mentioned above, this series of samples exhibited inhomogeneous degradation morphology (Figure 4.7), which is most likely due to the presence of sulphate. The interface layer obtained after immersion in media containing all three buffering salts was relatively thin (Figure 4.7), which emphasises the dominant role of $CaCl_2$ in controlling the degradation rate. Element mappings indicated the presence of carbon in the interface layer, but amorphous carbonate was detected by IR spectroscopy only for *x* = 1150 mg/L (see Figure 4.8d), suggesting that this is not the predominant phase for this series of samples. Oxalate IR peaks were not detected. IR spectra (Figure 4.8d) as well as EMPA (Table 4.3) indicated the presence of phosphate, in particular for the media containing $NaHCO_3$, but for x = 1150 mg/L, the dispersion was very high. The combined EMPA and IR data suggest that the low total oxide values are due to hydrous species and/or porosity rather than presence of carbonate. Crystalline $Mg(OH)_2$ generates a sharp feature at 3704 cm^{-1} in the IR reflection spectra, but such a signal was not detected for the samples studied here. Only a very broad IR band centred near 3500 cm^{-1} was detected (not shown) for samples immersed in solutions containing all three buffering salts. This suggests the presence of H_2O molecules embedded in interstitial spaces of magnesium oxide and magnesium-calcium-phosphorous oxides, which for this series prevailed over carbonate.

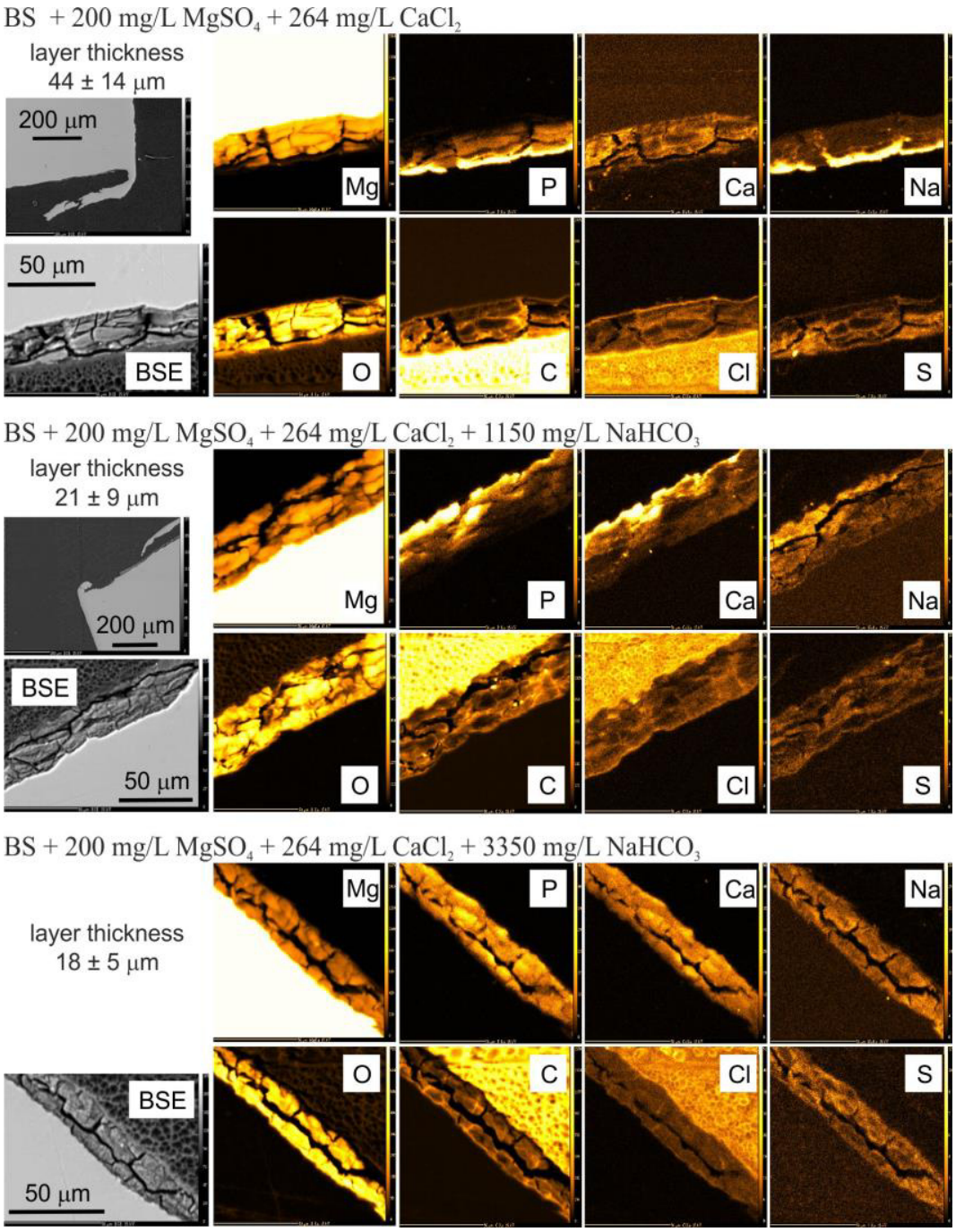

Figure 4.7: Backscattered electron (BSE) images and chemical element mappings of Mg immersed in basic solution (BS) with different concentrations of $NaHCO_3$ in the presence of both $CaCl_2$ and $MgSO_4$.

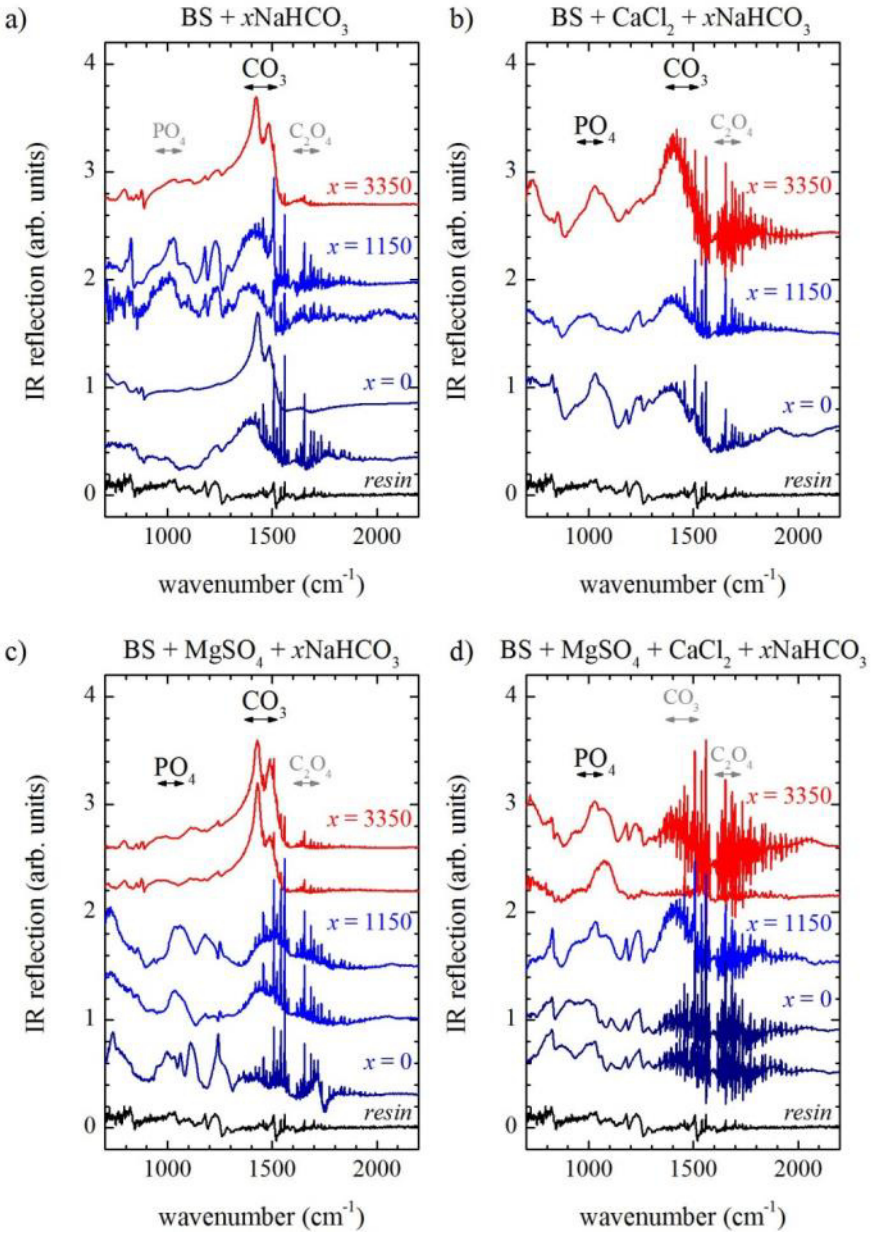

Figure 4.8: IR reflection spectra of the oxidised layer of Mg immersed in basic solution (BS) with different concentrations *x* of $NaHCO_3$ **(a)**; BS + 264 mg/L $CaCl_2$ with different concentrations *x* of $NaHCO_3$ **(b)**; BS + 200 mg/L $MgSO_4$ with different concentrations *x* of $NaHCO_3$ **(c)**; and BS + 200 mg/L MgSO4 + 264 mg/L $CaCl_2$ with different concentrations *x* of $NaHCO_3$ **(d)**; *x* = 0, 1150, 3350 mg/L. For some samples, two representative spectra are shown due to the strong inhomogeneity of the interface layer. The IR reflection spectrum of resin, in which the samples were embedded, is also give for comparison. Double arrows indicate the spectral ranges of the most intense IR reflection peaks of calcium/magnesium phosphate (PO_4), carbonate (CO_3), and oxalate (C_2O_4). The dominant chemical species in the corresponding group of corroded Mg samples are labelled in black whilst those with negligible concentration are in grey.

Table 4.3: Mean values of chemical elements detected by EMPA in the interface layer of Mg immersed in different media, along with the expected values for reference compounds with nominal chemical composition (in oxide wt%). Total oxides detectable by EMPA are less than the common value of 99-101 wt% when there are light elements with Z < 7 (e.g., H, C) and/or porosity. Points with total oxide value less than 33 wt% were excluded from the statistical averaging.

	Points	MgO (wt%)	P_2O_5 (wt%)	CaO (wt%)	Na_2O (wt%)	SO_2 (wt%)	Cl (wt%)	Total oxide (wt%) via EMPA
immersion medium								
BS	19	48 ± 6	0.30 ± 0.21	0.34 ± 0.25	0.15 ± 0.19	0.21 ± 0.12	0.07 ± 0.22	49 ± 6
BS + 1150 mg/L $NaHCO_3$	4	24 ± 5	8.3 ± 1.9	2.1 ± 0.9	0.31 ± 0.14	0.3 ± 0.3	0.35 ± 0.02	35.5 ± 2.6
BS + 3350 mg/L $NaHCO_3$	11	42 ± 8	2.1 ± 1.0	0.35 ± 0.15	0.15 ± 0.17	0.24 ± 0.11	0.07 ±0.09	45 ± 8
BS + 264 mg/L $CaCl_2$	13	48 ± 11	2.1 ± 1.5	1.3 ± 0.6	0.25 ±0.17	0.03 ± 0.17	0.27 ± 0.10	52 ± 10
BS + 264 mg/L $CaCl_2$ + 1150 mg/L $NaHCO_3$	16	34 ± 8	8 ± 6	9 ± 4	0.22 ± 0.07	0.08 ±0.09	0.10 ± 0.03	51 ± 7
BS + 264 mg/L $CaCl_2$ + 3350 mg/L $NaHCO_3$	7	39 ± 11	5.0 ± 1.7	4.3 ± 1.9	0.44 ± 0.20	0.04 ±0.03	0.32 ±0.09	49 ± 13
BS + 200 mg/L $MgSO_4$	9	30 ± 5	9.7 ± 2.1	1.44 ± 0.15	0.32 ± 0.13	0.25 ± 0.13	0.08 ± 0.03	42 ± 6
BS + 200 mg/L $MgSO_4$ + 1150 mg/L $NaHCO_3$	9	28 ± 6	8 ± 3	3.5 ± 2.9	0.25 ± 0.07	0.18 ± 0.02	0.15 ± 0.04	40 ± 4
BS + 200 mg/L $MgSO_4$ + 3350 mg/L $NaHCO_3$	23	47.5 ± 8.4	0.22 ± 0.08	0.14 ± 0.08	0.032 ± 0.019	0.19 ±0.06	0.011 ±0.010	48 ± 8
BS + 200 mg/L $MgSO_4$ + 264 mg/L $CaCl_2$	11	59 ± 6	1.3 ± 1.0	0.86 ± 0.18	0.22 ± 0.08	0.10 ± 0.08	0.22 ± 0.16	61 ± 6
BS + 200 mg/L $MgSO_4$ + 264 mg/L $CaCl_2$ + 1150 mg/L $NaHCO_3$	12	42 ± 9	5 ± 5	2.8 ± 2.8	0.32 ± 0.24	0.09 ± 0.05	0.29 ±0.23	51 ± 8
BS + 200 mg/L $MgSO_4$ + 264 mg/L $CaCl_2$ + 3350 mg/L $NaHCO_3$	6	26 ± 3	7.3 ± 1.3	5.0 ± 0.9	0.41 ± 0.17	0.17 ± 0.06	0.31 ±0.07	39 ± 4
Reference compounds								
$MgCO_3$		~ 47						~ 47
$Mg(OH)_2$		~ 66						~ 66
$MgC_2O_4.H_2O$		~ 33						~ 33
$Ca_5(PO_4)_3OH$			~ 42	~52				~ 94
$NH_4MgPO_4.6H_2O$		~ 16	~ 29					~ 54

4.2.2. Influence of cell culture media composition on pure magnesium degradation

Degradation rate, pH, and osmolality

Online pH measurements are shown in Figure 4.9A. The pH for the controls showed higher values on DMEM of approximately 7.7, followed by RPMI at 7.3 and HBSS at 6.6. When the samples were immersed in these media, the pH changes in HBSS were the highest from 8.8 to 9, followed by DMEM, which decreased from an initial pH of 8.8 to approximately 8 at the end of immersion. The RPMI with magnesium samples showed many changes at the first 24 hours, after which the pH was almost stable in the range of 8 to 7.8.

The degradation rate after immersion for 3 and 14 days in DMEM, RPMI, and HBSS were calculated by the weight loss method. The results in Figure 4.9B show that the degradation rate in HBSS was significantly higher than those in in RPMI and DMEM. Samples immersed in DMEM after 3 days had a degradation rate of approximately 0.35 [mm/year], whilst in RPMI, the rate was approximately 0.22 [mm/year]. After 14 days, the degradation rates in both media (RPMI and DMEM) were comparable.

Osmolality changes over the 14-day immersion time are shown in Table 4.4. The results show that DMEM had the highest values compared to the other two media. When magnesium was immersed in the media, changes in HBSS were the highest, followed by RPMI and DMEM.

Table 4.4: Osmolality values [Osmoles/kg] of the extract at the medium exchanging points. Measurements were performed on HBSS, DMEM, and RPMI with magnesium and on media alone as controls.

Condition	Immersion time [day]				
	0	3	7	11	14
HBSS + Pure Mg	0.302 ± 0.011	0.368 ± 0.056	0.328 ± 0.007	0.393 ± 0.072	0.396 ± 0.005
HBSS control	0.301± 0.012	0.274 ± 0.004	0.283 ± 0.002	0.247 ± 0.004	0.243 ± 0.001
DMEM + Pure Mg	0.366 ± 0.008	0.365 ± 0.005	0.352 ± 0.003	0.346 ± 0.002	0.327 ± 0.003
DMEM control	0.355 ± 0.002	0.356 ± 0.002	0.344 ± 0.003	0.342 ± 0.002	0.322 ± 0.002
RPMI + Pure Mg	0.281 ± 0.001	0.285 ± 0.002	0.280 ± 0.004	0.244 ± 0.004	0.241 ± 0.002
RPMI control	0.262 ± 0.002	0.265 ± 0.002	0.269 ± 0.002	0.235 ± 0.001	0.235 ± 0.002

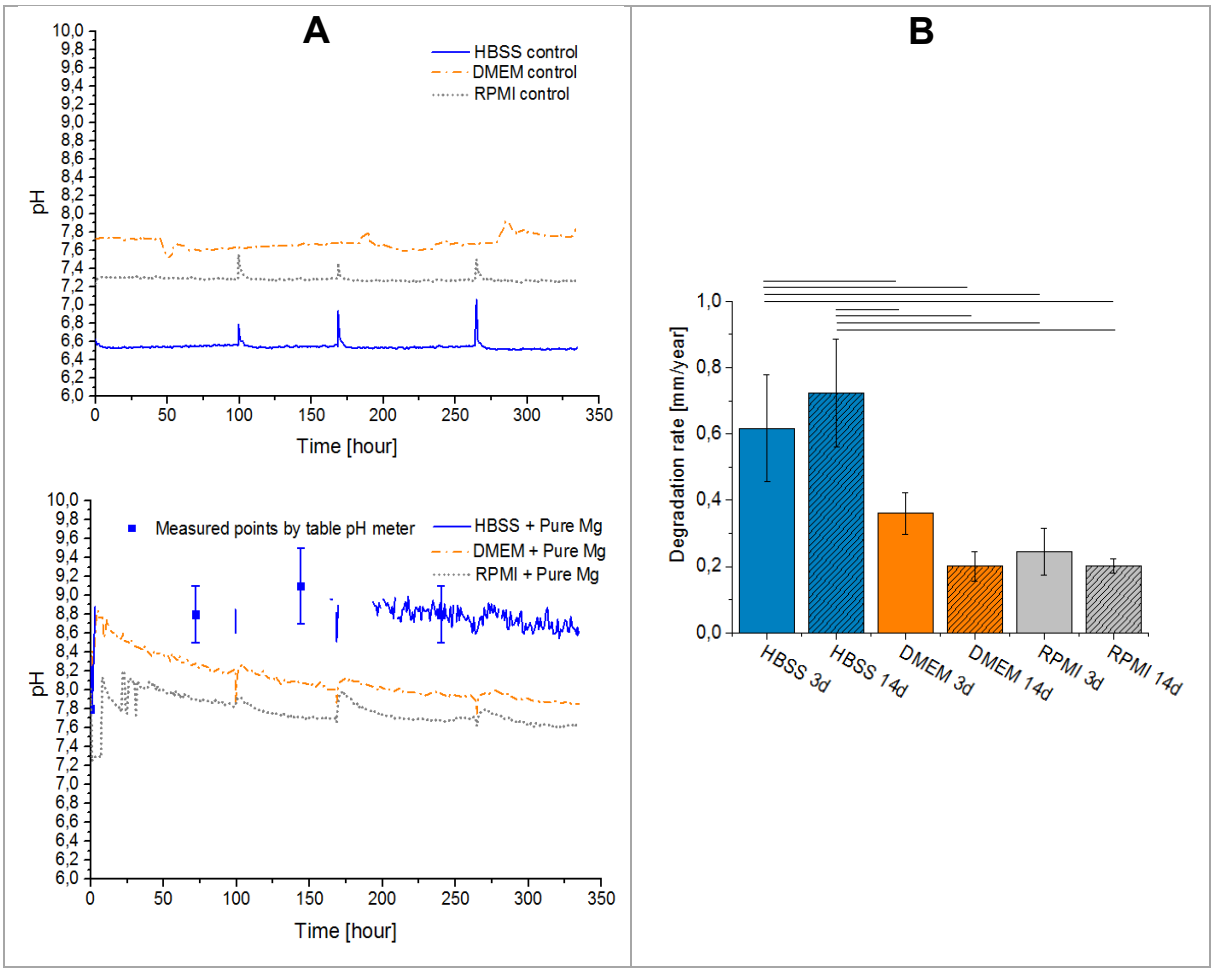

Figure 4.9: (A) pH changes during the immersion time in HBSS, DMEM, and RPMI. **(B)** Degradation rate for samples after immersion for 4 and 14 days. The significant differences between the immersion media are marked by lines (ANOVA on ranks with Tukey's multiple comparison test; significance level < 0.05).

Chemical element mapping, FTIR and EMPA of the corroded layer

Images of the degradation morphologies resulting from immersion in DMEM, RPMI, and HBSS after 3 and 14 days of immersion were obtained by SEM. EDX area mapping was performed at 15 kV to obtain a rough idea of the dominating chemical elements on the sample surfaces treated in different media (see Figure 4.10). Samples treated in HBSS showed some Cl, Mg, and O presence after 3 days. After 14 days, the surface was covered with needle-shaped crystal precipitations containing Mg, Na, O, and Cl. Samples immersed in DMEM showed Mg, O, Na, and Ca on the surface, whilst samples immersed in RPMI showed fewer degradation features and basically Mg, Na, Ca, O, and P chemical elements, and after 14 days, P was highly quantified on the degraded surface.

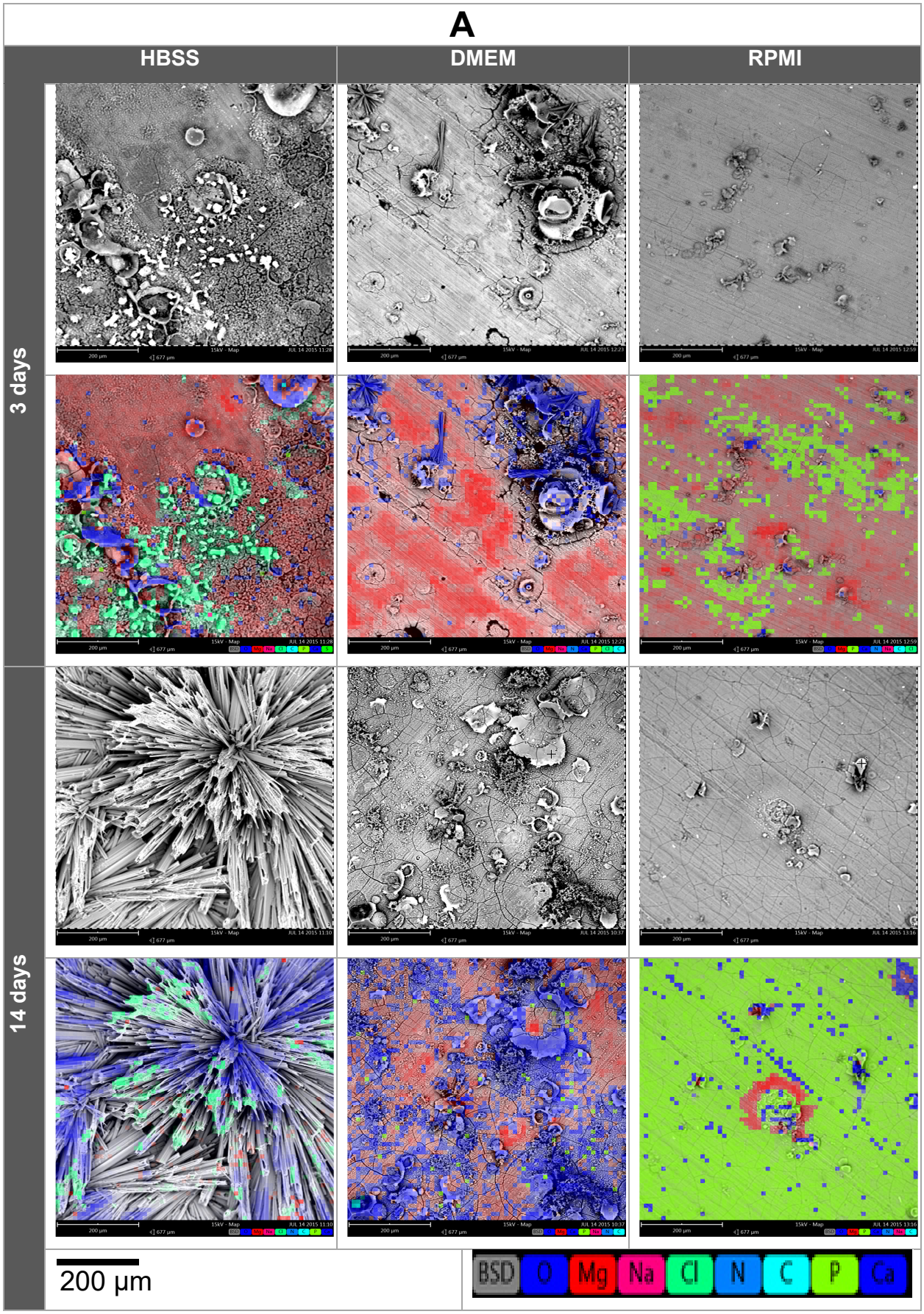
A
HBSS
DMEM
RPMI
3 days
14 days
200 µm
BSD
O
Mg
Na
Cl
N
C
P
Ca

B

HBSS (3 days)

Area measurement

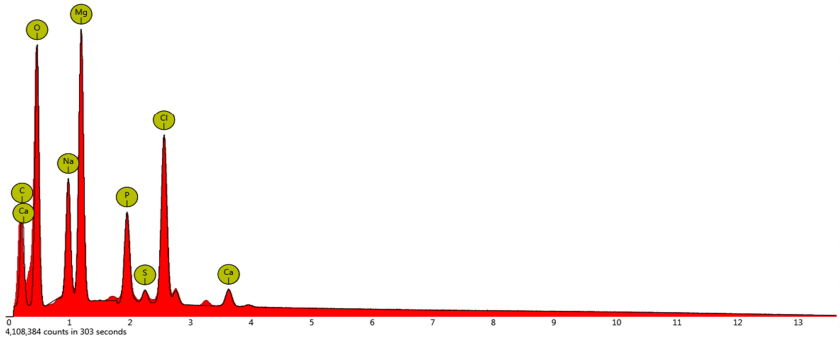

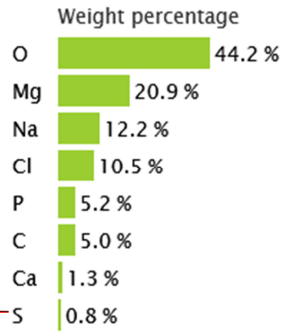

Point measurement

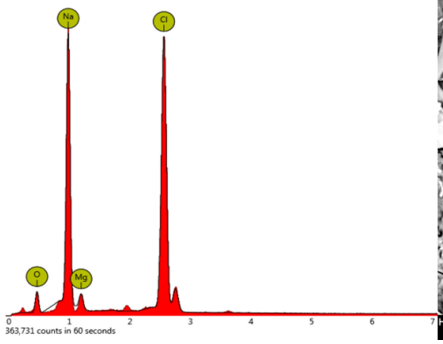

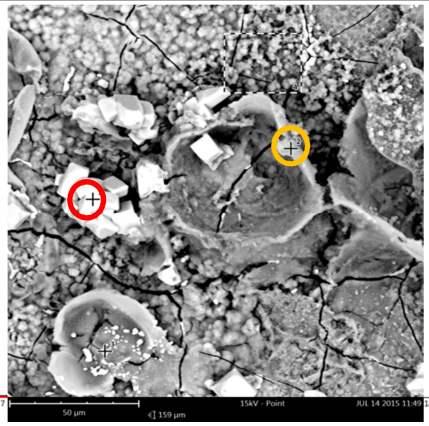

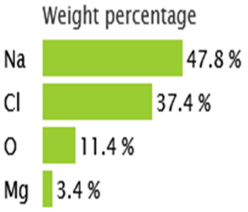

Point measurement

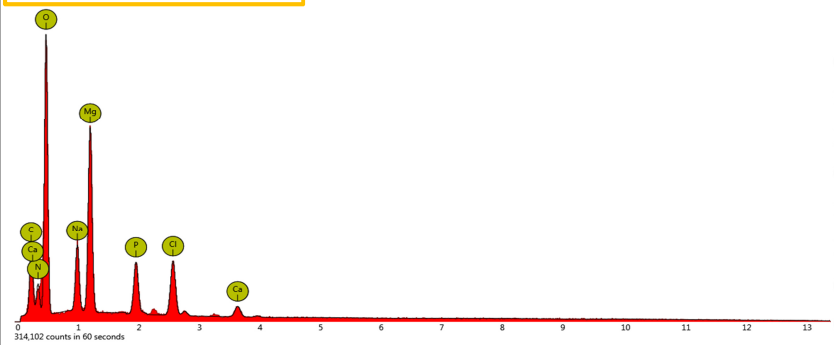

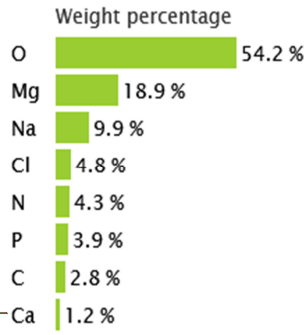

HBSS (14 days)

Area measurement

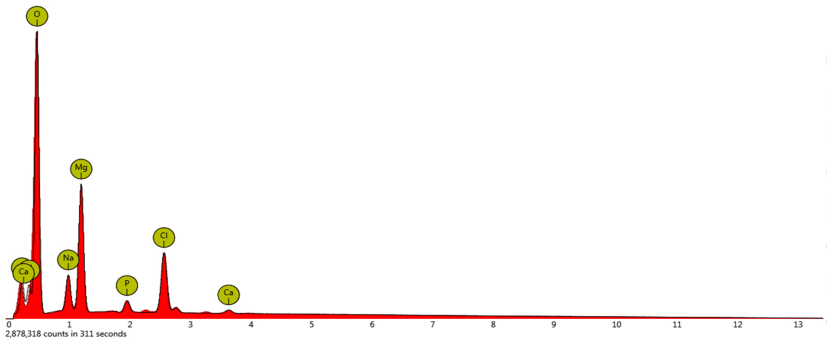

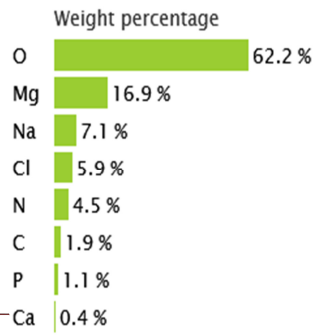

DMEM (3 days)

Area measurement

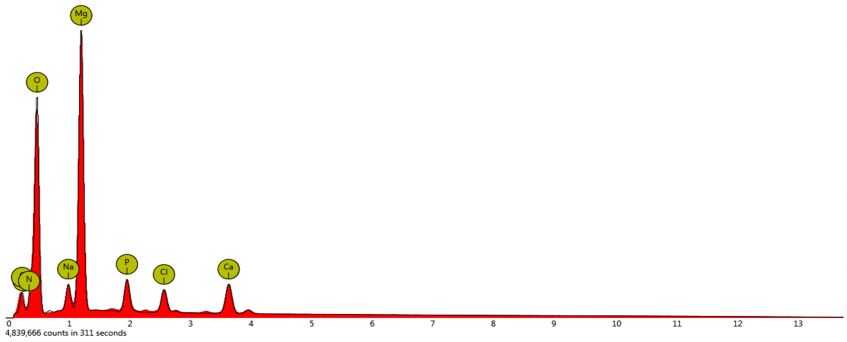

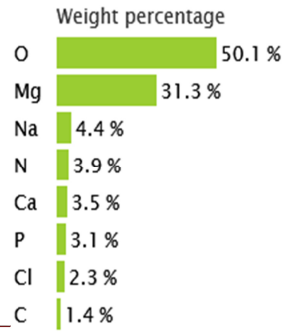

Area measurement

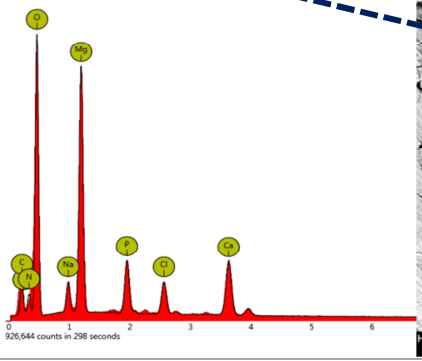

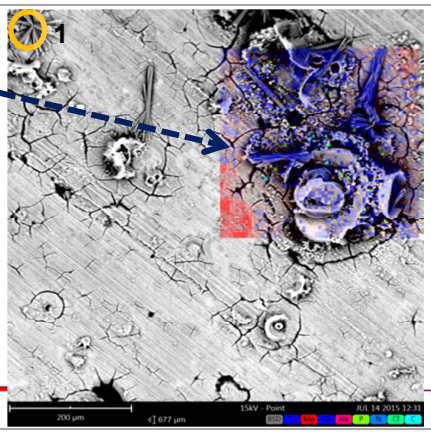

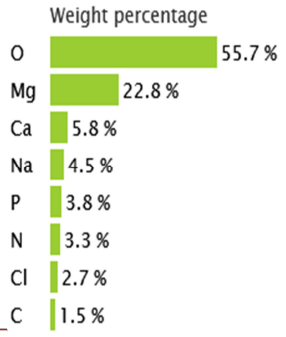

Point measurement

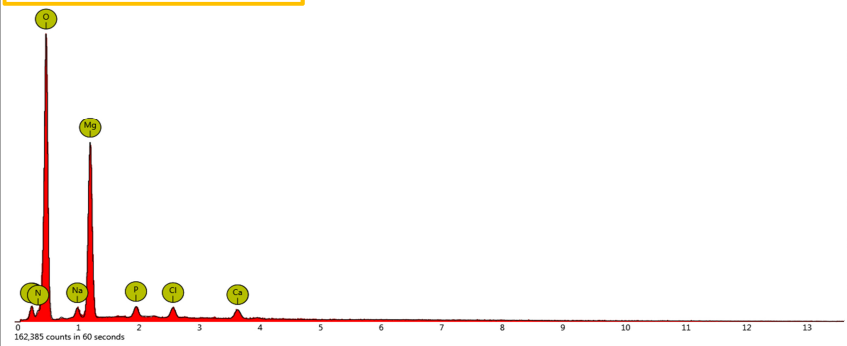

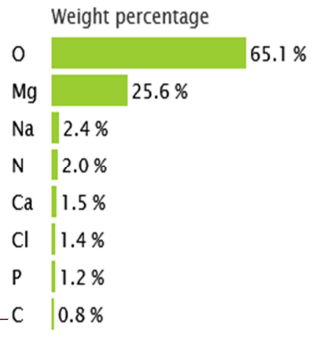

DMEM (14 days)

Area measurement

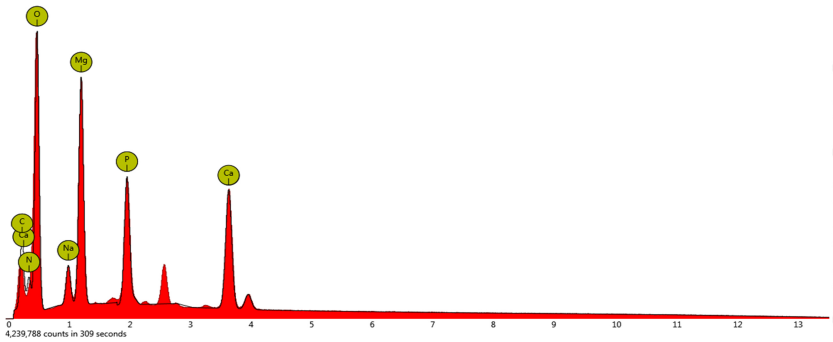

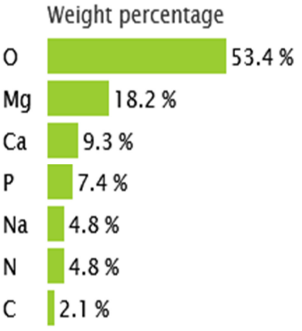

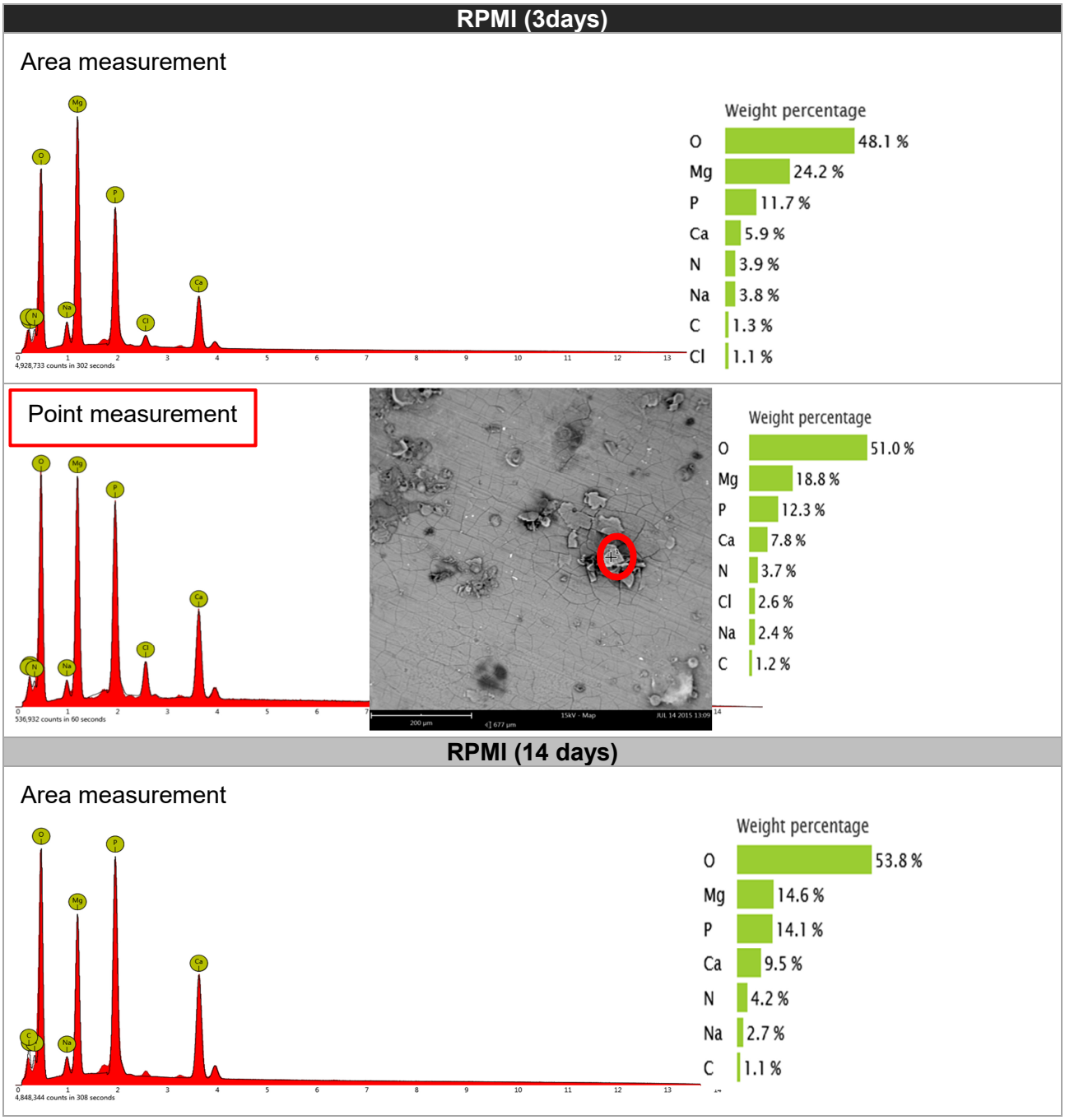

Figure 4.10: A: Images on the degraded surface morphologies obtained by SEM, and EDX element mapping with 15 kV on samples after immersion for 3 and 14 days in HBSS, DMEM, and RPMI. **B:** Elements wt% and their corresponding spectra measured by EDX on the areas presented in (A) and on points of interest.

Electron microprobe analysis (EMPA) measurements were performed to check the element concentrations at a higher resolution. Mapping on the cross-sections was performed after 14 days of immersion to check the element distributions across the degradation layer.

HBSS

Samples immersed in HBSS showed at degradation layer high in Mg, O, and C, as revealed by both element mapping (Figure 4.11) and IR reflection spectra (Figure 4.12). In addition, the IR spectroscopic data indicate that carbon is derived from carbonate. The predominance of Mg over Ca and Na (see Table 4.5) shows that the formed phase is $MgCO_3$. Similar to SEM, after 3 days, Na-Cl precipitations were also observed in the degradation layer (see the arrow in Figure 4.11). The tested samples with these two measurements were immersed for 10 days instead of 14 as an exception for this specific condition.

DMEM

The degradation interface for the samples immersed in DMEM showed heterogeneous and layer zonation in its morphology. Close to the metallic bulk, the precipitation of Ca was correlated with P, Na and O, and the interface was also rich with C. FTIR results showed amorphous $MgCO_3$ (see Figure 4.12) and phosphate (see Figure 4.12, and Table 4.5). The EMPA analysis shown in Table 4.5 indicated the formation of Mg-Ca-P oxides.

RPMI

Like DMEM, a similar element distribution correlation was observed for samples immersed in RPMI. FTIR show amorphous $MgCO_3$ and phosphate. The EMPA analysis shown in Table 4.5 indicated the presence of magnesium phosphate as the predominant phase. The layer also showed some precipitation in which Cl, Mg and O were the main contents (see Figure 4.11). In general, samples immersed in RPMI showed a thinner degradation layer compared to the samples immersed in the other two media (Figure 4.11).

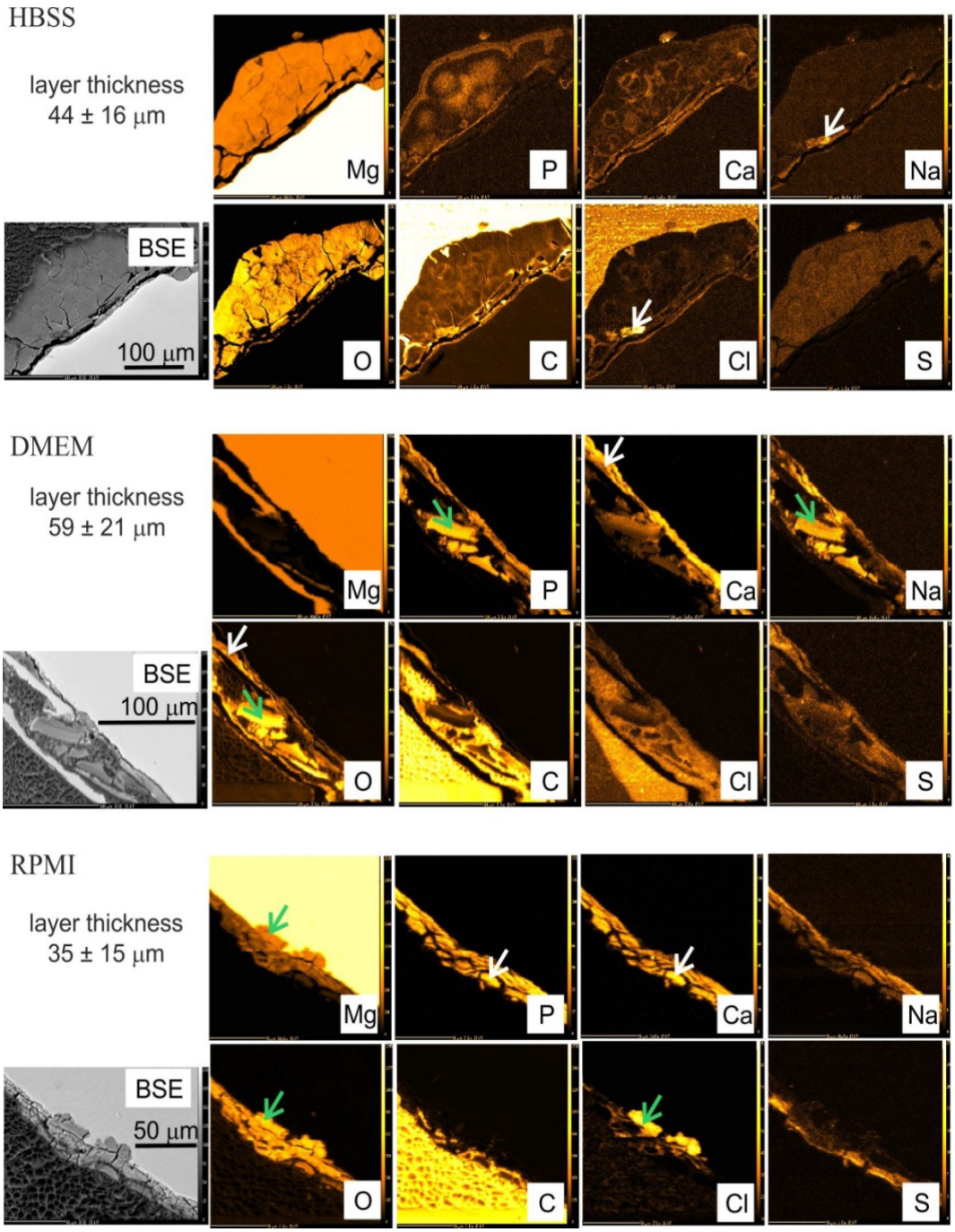

Figure 4.11: Backscattered electron (BSE) images and chemical mappings of Mg samples immersed in HBSS, DMEM, and RPMI.

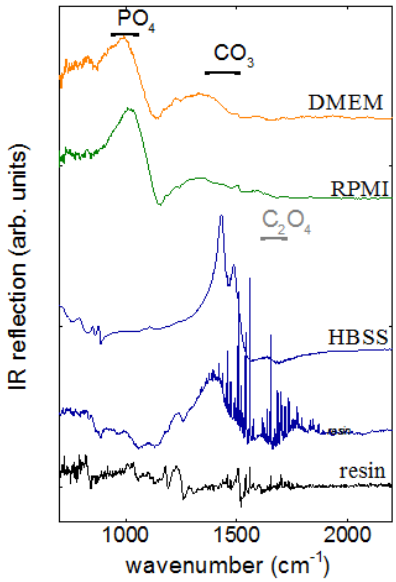

Figure 4.12: IR reflection spectra of the oxidised layer of pure magnesium samples immersed in HBSS, DMEM, and RPMI. The IR reflection spectrum of resin, in which the samples were embedded, is given for comparison. Double arrows indicate the spectral ranges of the most intense IR reflection peaks of calcium/magnesium phosphate (PO_4), carbonate (CO_3), and oxalate (C_2O_4).

Table 4.5: Mean values of chemical elements detected by EMPA in the interface layer of Mg immersed in different media, along with the expected values for reference compounds with nominal chemical compositions (in oxide wt%). Total oxides detectable by EMPA are less than the common value of 99-100 wt% when there are light elements with Z<7 (e.g., H, C) and/or porosity. Points with total oxide value less than 33 wt% were excluded from the statistical averaging.

	Points	MgO (wt%)	P_2O_5 (wt%)	CaO (wt%)	Na_2O (wt%)	SO_2 (wt%)	Cl (wt%)	Total oxide (wt%) via EMPA
Immersion medium:								
HBSS	19	48 ± 6	0.30 ± 0.21	0.34 ± 0.25	0.15 ± 0.19	0.21 ± 0.12	0.07 ± 0.22	49 ± 6
DMEM	10	24 ± 8.6	25.4 ± 8.2	6.05 ± 2.73	0.9 ± 0.6	0.29 ± 0.14	0.15 ± 0.01	57 ± 9
RPMI	11	16.7 ± 6.7	25.2 ± 4.4	11.15 ± 1.9	0.9 ± 0.3	0.4 ± 0.13	0.43 ± 0.21	55 ± 8.8
Reference compounds:								
$MgCO_3$		~ 47						~ 47
$Mg(OH)_2$		~ 66						~ 66
$MgC_2O_4.H_2O$		~ 33						~ 33
$Ca_5(PO_4)_3OH$			~ 42	~52				~ 94
$NH_4MgPO_4.6H_2O$		~ 16	~ 29					~ 54

4.3. Magnesium degradation under osteoblast cells interaction

The direct interaction between the human primary osteoblast cells and magnesium materials was studied. Pure magnesium as a control and two magnesium alloys (Mg-2Ag and Mg-10Gd were selected for this part of experiments. The reason for using osteoblasts is to determine whether their role in mineralisation can influence the composition and morphology of the degradation interface. The fibroblasts L929 cell line was used as a cell control. The following abbreviations were used in this part of the experiment to refer to the used conditions.

SNC: **S**amples with **N**o **C**ells **MC**: **M**edium **C**ontrol

SC: **S**amples with **C**ells **CC**: **C**ell **C**ontrol

Degradation rate

The degradation rates by weight loss after immersion for 4 and 14 days are shown in Figure 4.13. The results show the influence of time on degradation, which is significantly higher for short-term immersion (4 days) than it is for long-term immersion (14 days) for all materials. The influence of cells was more apparent after 14 days of immersion than after 4 days of immersion. Specifically, decreases in the degradation rate was observed for the pure Mg (with a reduction factor; 4 d = 95.3%, 14 d = 70.4%) and Mg-10Gd (4 d = 95.6%, 14 d = 84%) compared with the negative control. By contrast, the degradation rate increased when Mg-2Ag was incubated with cells (4 d = 103.4%, 14 d = 116.3%).

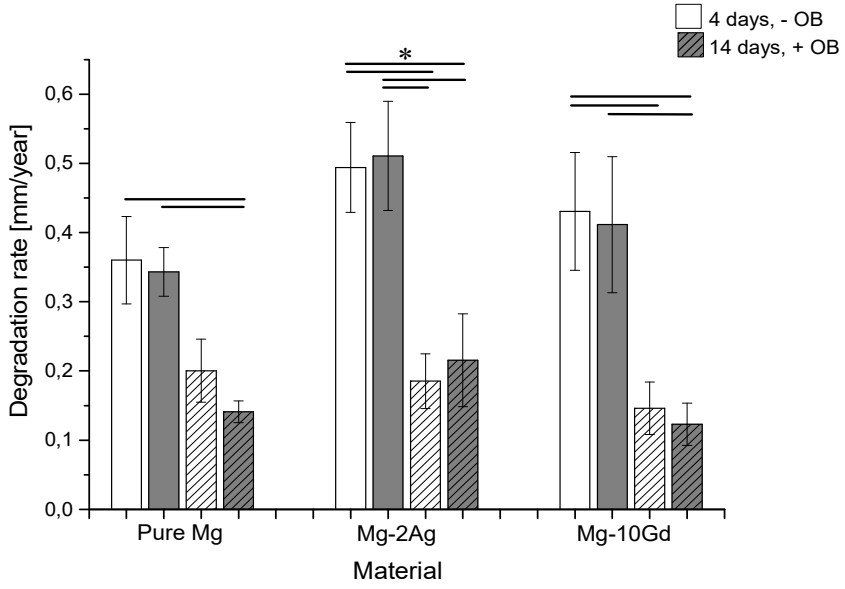

Figure 4.13: Mean degradation rate [mm/year] according to the weight loss method after 4 and 14 days of immersion for pure Mg, Mg-2Ag and Mg-10Gd discs with and without OB cells. Significant differences between the conditions of Mg-10Gd and pure Mg were detected using a one way analysis of variance (ANOVA) on ranks with Dunn's multiple comparison post hoc test at a significance level of $p < 0.05$. Differences between the conditions of Mg-2Ag were analysed with ANOVA and the Holm-Sidak post hoc test at a significance level of $p < 0.001$ (*).

Online pH and osmolality

The pH changes over the immersion time for the different materials were measured online (Figure 4.14). Incubation with cells slightly decreased the pH of the controls, which was consistent with the behaviour of L929 cells during the first 125 hours of incubation. The plotted results showed that the pH values for all studied materials ranged from 8 to 9. Cells influenced the first 250 hours of immersion depending on the studied alloy. Mg-2Ag with cells showed higher pH values than the negative control (**SNC**), and this difference was also noted for pure Mg after 72 hours of immersion with cells. However, the opposite effect was observed when Mg-10Gd was incubated with cells. The osmolality (Table 4.6) tended to inversely correlate with the immersion time for all alloys incubated with cells. After 14 days, the osmolality values of experimental samples were in the range of the control value, which indicates a reduction in the dissolving material resulting from the formation of a low-solubility layer on the material surface. Incubation with L929 cells did not significantly change the pH for any of the materials, which can be explained by the natural tendency of these cells to deposit a continuous layer on the material that minimises the interaction between the material and the medium.

Table 4.6: Osmolality changes [Osmol/Kg] during the immersion period with pure Mg, Mg-2Ag, and Mg-10Gd with and without OB cells.

Condition	Immersion time [day]				
	1	4	8	11	14
Control	0.355 ± 0.001	0.357 ± 0.002	0.345 ± 0.003	0.341 ± 0.002	0.324 ± 0.002
Control cells	-	0.373 ± 0.002	0.364 ± 0.005	0.348 ± 0.001	0.325 ± 0.002
Pure Mg	0.366 ± 0.008	0.365 ± 0.005	0.352 ± 0.004	0.347 ± 0.004	0.327 ± 0.002
Pure Mg + OB	-	0.363 ± 0.007	0.355 ± 0.007	0.353 ± 0.003	0.325 ± 0.004
Mg-2Ag	0.361 ± 0.005	0.367 ± 0.008	0.355 ± 0.006	0.349 ± 0.003	0.327 ± 0.002
Mg-2Ag + OB	-	0.365 ± 0.009	0.350 ± 0.009	0.354 ± 0.005	0.325 ± 0.003
Mg-10Gd	0.360 ± 0.004	0.365 ± 0.008	0.355 ± 0.008	0.345 ± 0.003	0.328 ± 0.002
Mg-10Gd + OB	-	0.360 ± 0.004	0.343 ± 0.004	0.350 ± 0.007	0.325 ± 0.003

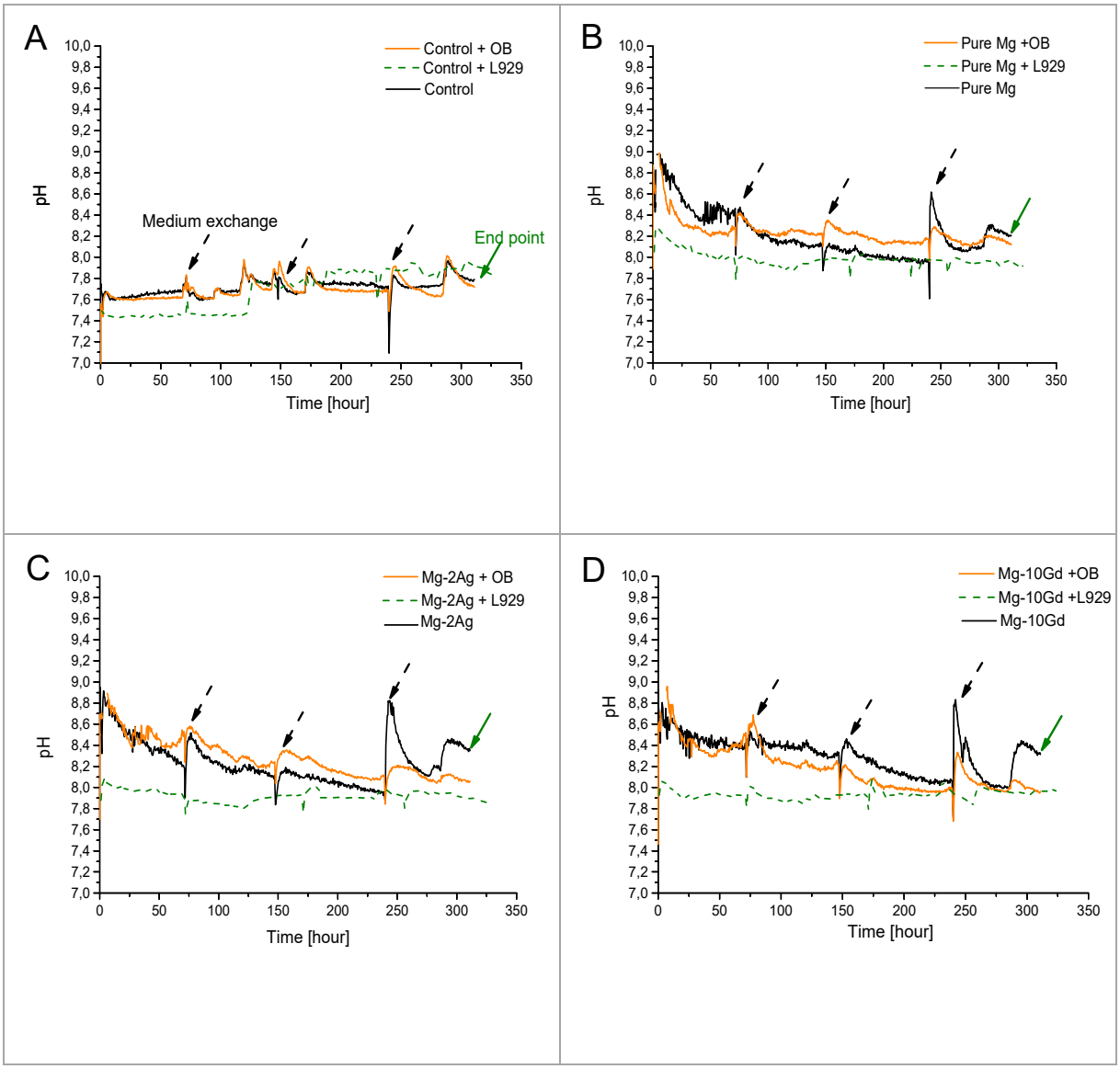

Figure 4.14: Online pH measurements during 336 hours of immersion. Controls in tissue culture well plate **(A)**, pure Mg **(B)**, Mg-2Ag **(C)**, and Mg-10Gd **(D)**. Arrows in the figure indicate the medium exchange and the end points of the immersion test.

Cell viability and morphology

The cell viability was analysed by Live/Dead staining (Figure 4.15). The results showed that the cells were mostly alive. Images obtained after 4 days of immersion at 4x magnification show a better distribution of the cells on pure Mg and Mg-10Gd than on Mg-2Ag; however, the cells appeared to be more developed and better distributed on all materials after 14 days (Figure 4.15, 4x magnification).

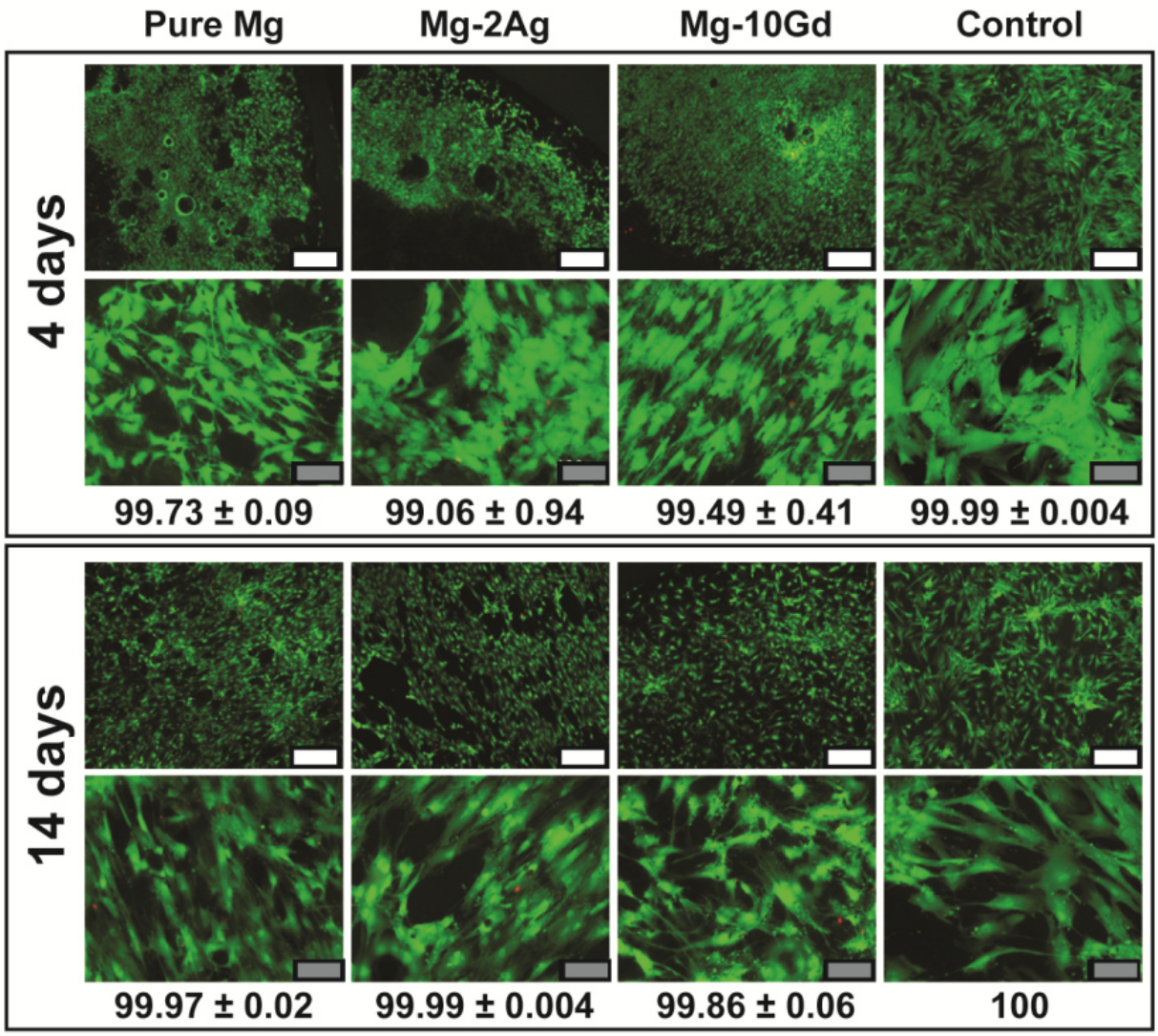

Figure 4.15: Osteoblast cell viability by Live/Dead staining after 4 and 14 days of immersion in direct contact with pure Mg, Mg-2Ag, Mg-10Gd, and the control on tissue culture plates. White and grey scale bars represent 500 and 100 µm, respectively.

The SEM images (Figure 4.16) revealed the cell morphology and adherence to the studied materials. Images of cells obtained after 4 days of incubation on Mg-2Ag revealed cell-surface blebbing. These features were less apparent on pure Mg. After 14 days, the images of all materials showed developed and spread of cell morphology.

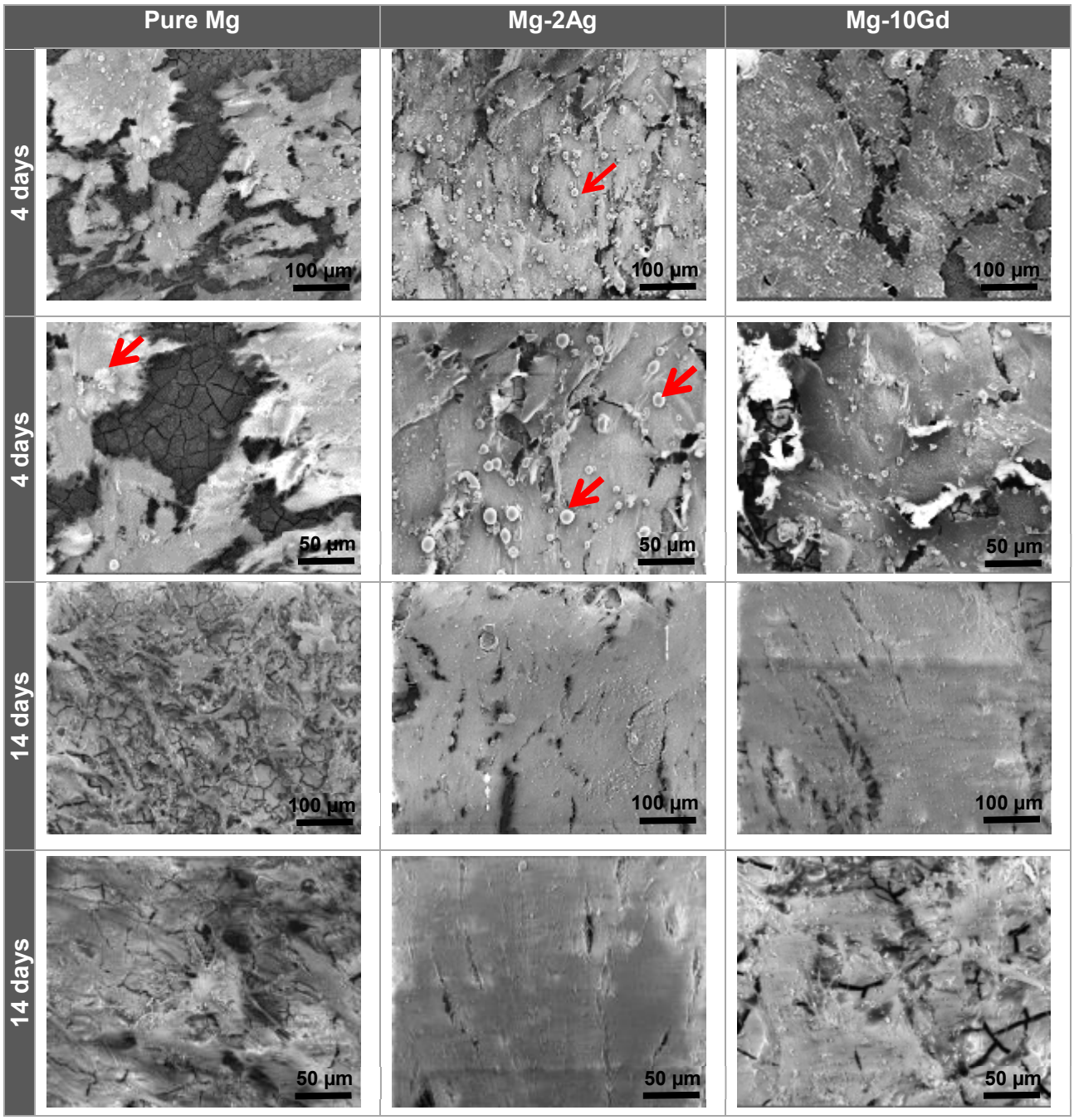

Figure 4.16: SEM images of cell morphology and coverage after 4 and 14 days of immersion in direct contact with pure Mg, Mg-2Ag and Mg-10Gd. Arrows indicate blebs on the cell surface.

Cytotoxicity assessment by measuring Lactate dehydrogenase (LDH)

The LDH activity in the immersion medium was measured to assess the cytotoxicity induced by the degradation of the studied materials after 1, 2, 3, 7, and 14 days of immersion. At days 7 and 14, the quantified LDH activity was approximately 0%, and therefore, only the activities at days 1, 2 and 3 are shown in Figure 4.17. After 1 day of immersion, the cytotoxicity of Mg-2Ag was higher than that of the other materials, and this cytotoxicity increased further after 2 days of immersion. This finding indicates the high initial material-medium interaction for this alloy, which induced cell damage; however, this influence decreased after 3 days of immersion. With pure Mg, the initial degradation influenced the viability of cells by approximately 5% after one day of immersion; this influence increased to approximately 33% at days 2 and 3 of immersion and decreased thereafter. The influence of Mg-10Gd degradation on cell damage was the highest on day 2, with a mean of approximately 34%.

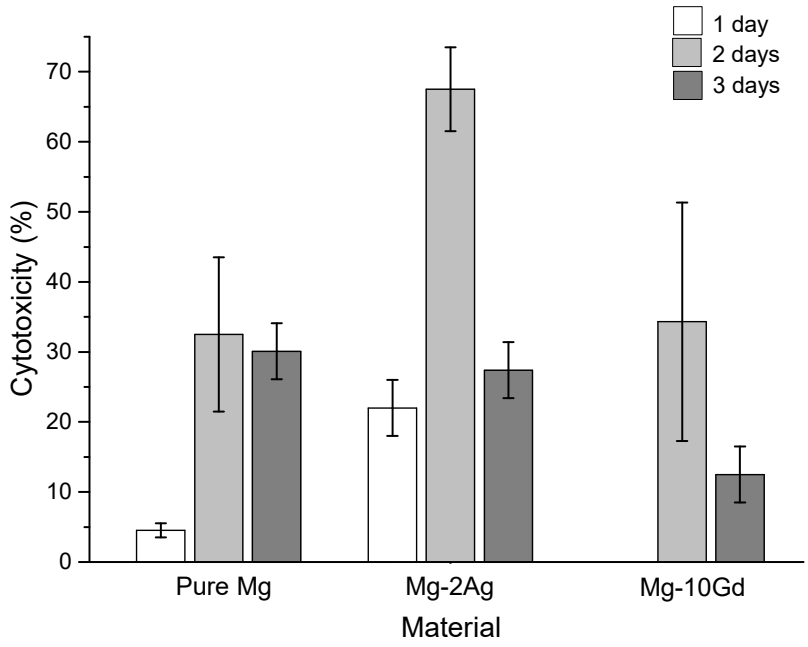

Figure 4.17: LDH release from the cells induced by the degradation of pure magnesium, Mg-2Ag, and Mg-10Gd. The measurements were obtained after 1, 2, 3, 7, and 14 days of immersion. LDH values at 7 and 14 days (not shown) were approximately 0%.

Mineralisation and cell distribution

Osteo-Image, a specific stain for hydroxyapatite (HA), was used to assess the mineralisation of osteoblasts (Figure 4.18). This stain was used to determine the role of osteoblasts in mineralisation, which can chemically alter the degradation interface composition. The results obtained for the negative controls (**SNC**) showed that the medium composition and cell culture conditions synergistically induced the formation of HA, which increased over time. Specifically, the quantified values were pure Mg = 0.9%, Mg-2Ag = 0.1%, and Mg-10Gd = 0.4% at 4 days and pure Mg = 2.8%, Mg-2Ag = 0.2%, and Mg-10Gd = 6.9% at 14 days. The influence of cells on HA formation is shown in Figure 4.18B. The amount of HA was highest on Mg-10Gd, followed by pure Mg and then Mg-2Ag. The amount of HA in the presence of cells on Mg-10Gd and pure Mg increased by factors of 4 and approximately 3, respectively. In general, the formation of HA on pure Mg showed a clustered distribution, whilst it was homogeneously distributed over the entire sample surface on Mg-10Gd. The Osteo-Image results of samples with L929 cells were comparable to those of the negative control samples (**SNC,** see Figure 4.18 A and C).

Figure 4.19 shows the high magnification multichannel images for DAPI (presented in grey) and Osteo-Image (green). These colours were selected to simplify colour discrimination. A mineralised matrix and cell distribution were evident on the Mg-10Gd samples after 4 days, and these phenomena were more apparent after 14 days, with overlapping deposits between the cells and the HA. However, HA formation induced by cells appeared to be slower on Mg-2Ag, which showed HA staining after 14 days (with a stained area of 2.3%) that was comparable to that observed on pure Mg (2.2%) and Mg-10Gd (4%) at 4 days.

Condition	Pure Mg	Mg-2Ag	Mg-10Gd
A **14 days without cells**	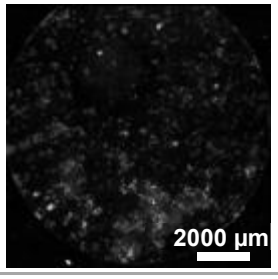	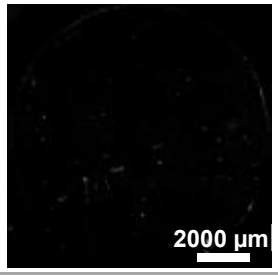	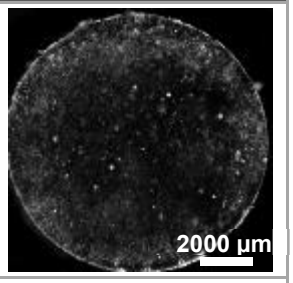
Stained area (%)	2.8 ±1.9	0.2 ± 0.1	6.9 ± 5.1
B **14 days (+OB)**	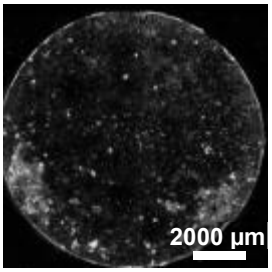	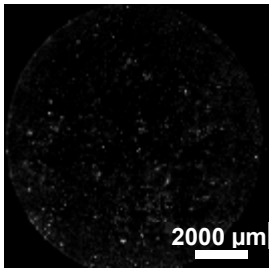	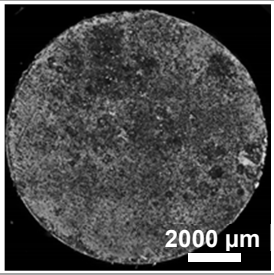
Stained area (%)	9.8 ± 3.9	2.3 ±1.2	27.1±10.3
C **14 days (+L929)**	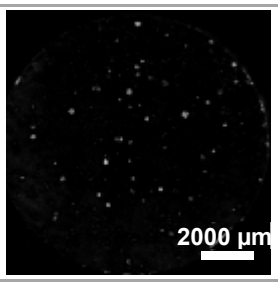	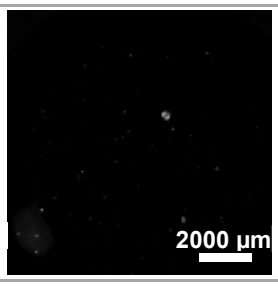	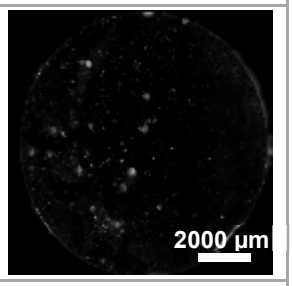
Stained area (%)	3.6 ± 2	0.5 ± 0.3	1.9 ±1.5

Figure 4.18: Fluorescent images of the stained hydroxyapatite (HA) on the different materials in monochromatic mode (i.e., mineralisation appears white) after 14 days of immersion; **(A)** without cells, **(B)** with primary human osteoblasts, and **(C)** with the L929 mouse fibroblast cell line. The stained area is estimated as the percentage of the shown field of view (values represent the mean of triplicate measurements for each condition).

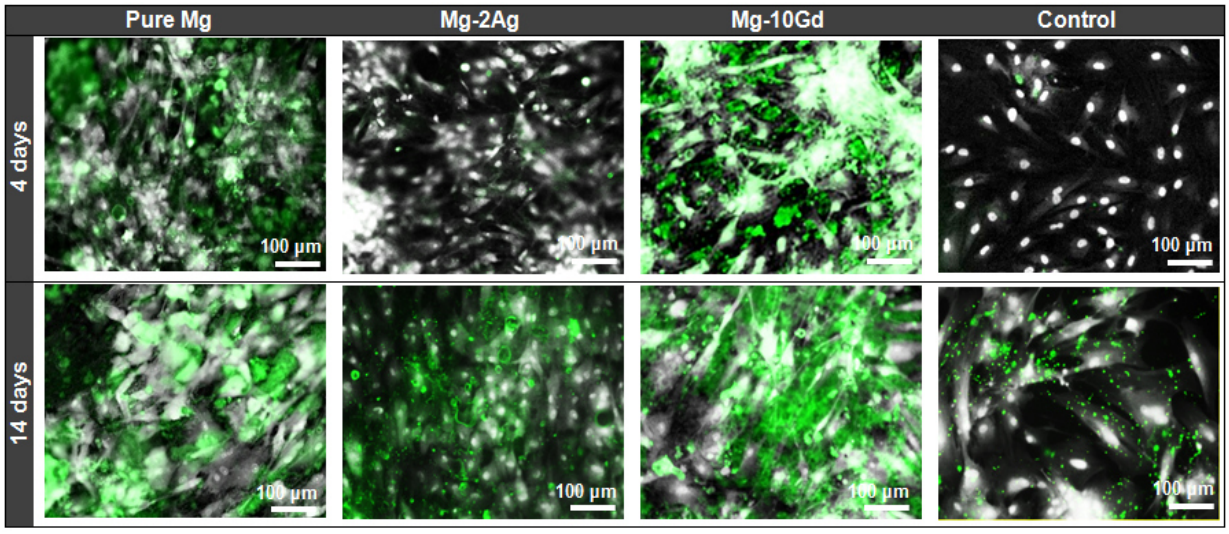

Figure 4.19: Fluorescent images at high magnification after 4 and 14 days of immersion. Cells stained with DAPI are shown in white/grey, and the mineralised matrix stained with Osteo-Image is shown in green.

Analysis of the degradation surface and interface with SEM/FIB/EDX

The morphologies of the degraded material surface before and after chromic acid treatment are shown in Figure 4.20 A and B. The black spots on the surface (Figure 4.20 B) were identified by SEM to be pits and grooves on the surface due to degradation (Figure 4.20 C). The presence of cells on the samples generally increased the formation of these degradation features on the surface (arrows in Figure 4.20 B) and particularly on Mg-2Ag, whose entire surface was covered by these features. In general, Mg-10Gd showed the least degraded surface despite the presence of a few corrosion features, followed by pure Mg. By contrast, the Mg-2Ag surface was highly affected.

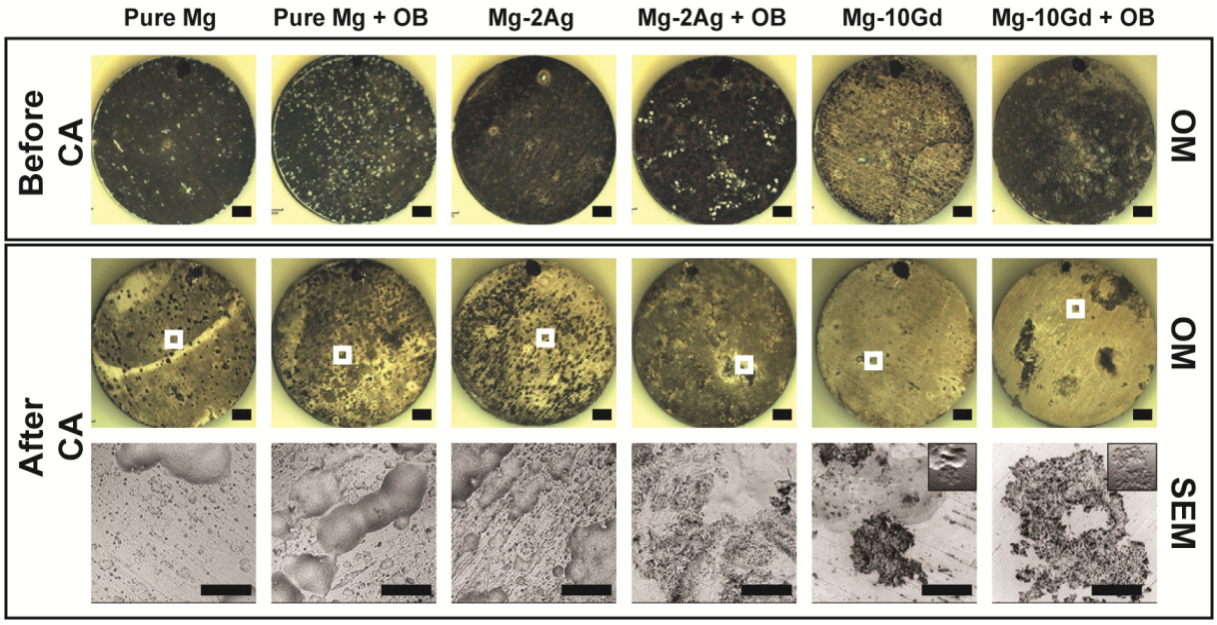

Figure 4.20: Degradation surface morphology after 14 days of immersion. CA refers to chromic acid, and OM indicates images obtained with optical microscope. The black spots on top of each sample are markers to define a coordinated position. The scale bar on the OM images represents 1 mm. SEM images of the points of interest defined by the white square on the OM images were obtained; the scale bar on the SEM images represents 200 µm

Figure 4.21 shows the FIB-processed cross-sections of the **SNC** and **SC** samples on and near the cells. SEM images of the cross-section were also obtained at high magnification. The degradation layer thickness indicated that the cells significantly influenced the degradation interface of Mg-10Gd. The degradation layer was almost six times thinner than the negative control (**SNC**) layer and showed deep cracks of approximately 80 µm in depth. This influence of cells was less pronounced for the other two materials that were studied. The EDX line measurements of the degradation interface are shown in Figure 4.21. In this figure, the results for the different cross-sections of the same material are scaled (normalised) to one another and named **AB** to compare the element distribution along the degradation interface in depth for scans performed from the top (point A) to the material bulk

(point B). The element quantification of sections directly on cells showed relatively minor increases in S, N, and C that coincided with the physical presence of cells. In addition to these elements, pure Mg showed a degradation layer rich in Ca-associated P and O that was observed near cells rather than directly on cells. This localisation can be linked to the degradation morphology of this material in the presence of cells (Figure 4.20). Specifically, the formation of pits and grooves on the surface may disturb optimum cell adhesion and result in a non-homogenous influence of cells on mineralisation. This Ca-P deposition was also observed on Mg-10Gd in the presence of cells. In this case, the formed degradation layer was rich in Gd (see Figure 4.21). The EDX scans of Mg-2Ag differed from those of the other two alloys. Specifically, the levels of Ca and P on the different sections were almost the same, which may indicate that cells were minimally active on this alloy, and their role in mineralisation was not easily detected with EDX.

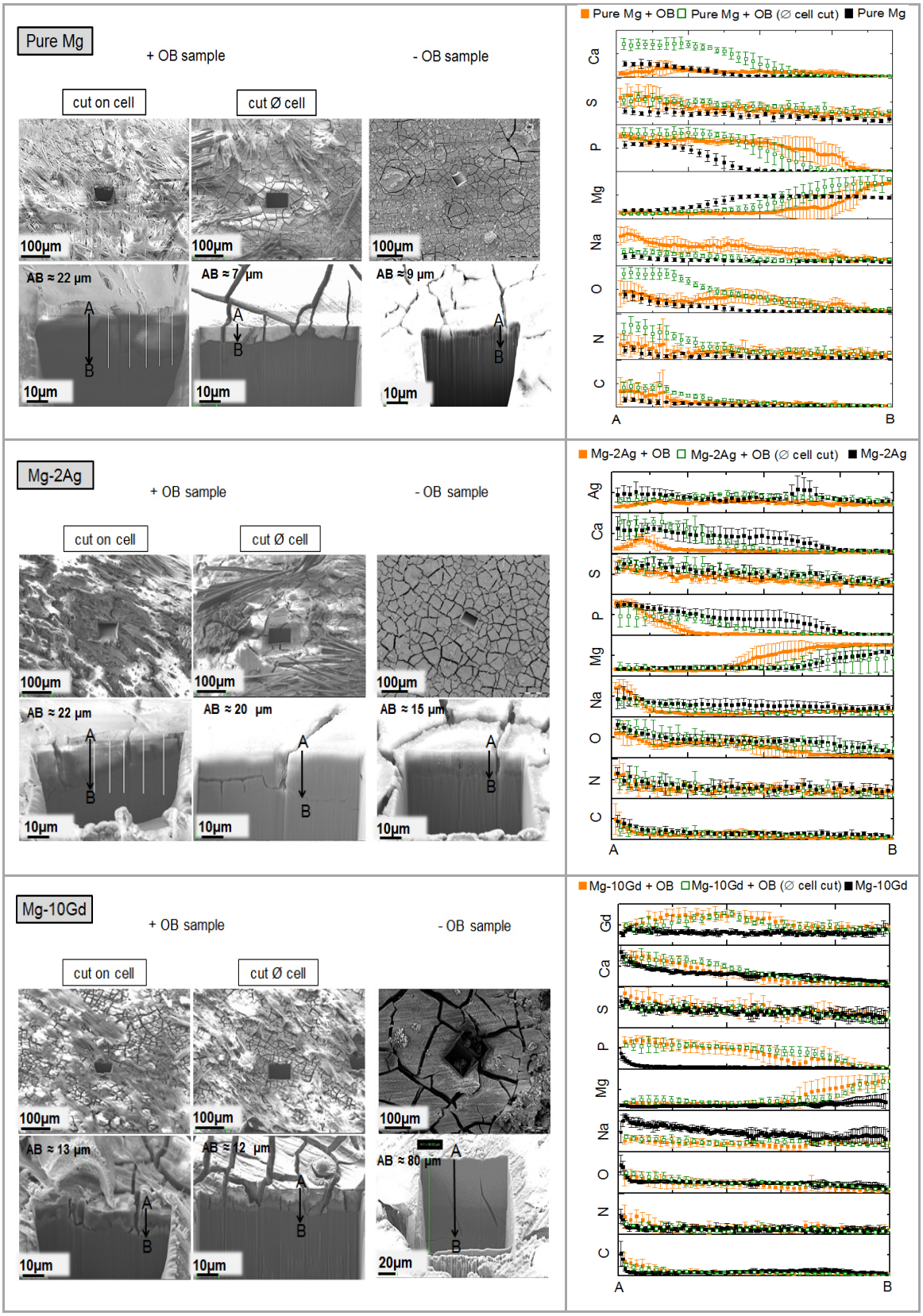

Figure 4.21: SEM images of the processed cross-sections of samples with and without OB cells on and near the cell. The charts show the EDX line scan measurements on the processed cross-sections. |AB| values represent the cross-section thickness. EDX line scans start at point (A) and end at point (B).

Chemical element mapping, FTIR and EMPA of the corroded layer

To determine the cell influence on the chemical composition of the degradation interface, a pure magnesium sample (the control material) with osteoblasts was further subjected to chemical element mapping, FTIR microspectroscopy (Figure 4.22), and electron microprobe analysis (Table 4.7). Samples were immersed for 14 days in DMEM. Chemical element mapping on the degradation cross-section showed the corresponding Ca and P element distributions. The degradation interface was also rich in C, N, S and O. FTIR measurements show two signals around CO_3 and PO_4, indicating the precipitations based on these phases. The EMPA analysis showed a CaO/P_2O_5 ratio close to apatite with high MgO content, suggesting that Mg-rich apatite is a predominant chemical composition for this sample.

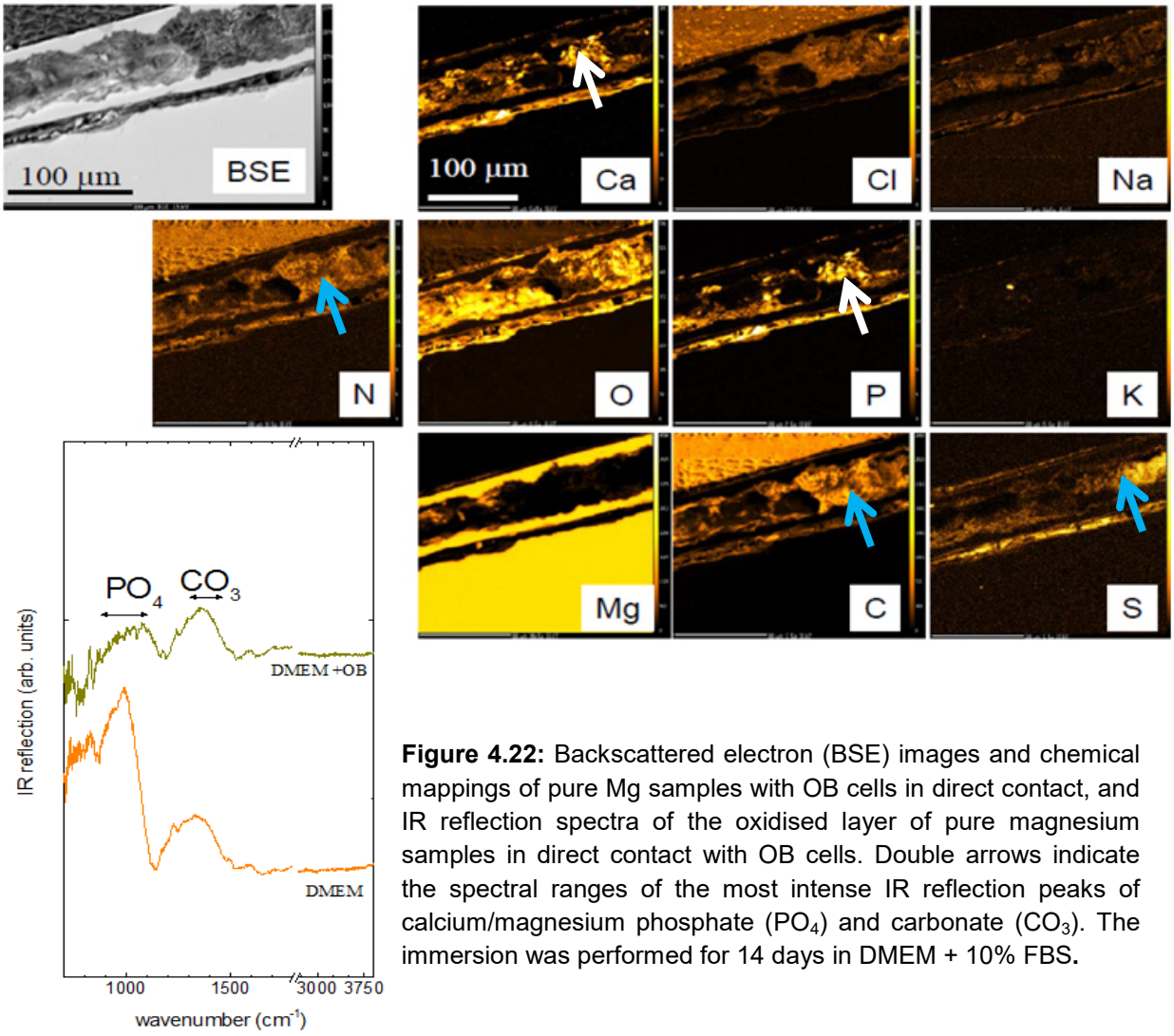

Figure 4.22: Backscattered electron (BSE) images and chemical mappings of pure Mg samples with OB cells in direct contact, and IR reflection spectra of the oxidised layer of pure magnesium samples in direct contact with OB cells. Double arrows indicate the spectral ranges of the most intense IR reflection peaks of calcium/magnesium phosphate (PO_4) and carbonate (CO_3). The immersion was performed for 14 days in DMEM + 10% FBS.

Table 4.7: Mean values of chemical elements detected by EMPA in the interface layer of pure magnesium in direct contact with OB cells, along with the expected values for reference compounds with nominal chemical compositions (in oxide wt%). Total oxides detectable by EMPA are less than the common value of 99-100 wt% when there are light elements with Z<7 (e.g., H, C) and/or porosity. Points with total oxide value less than 33 wt% were excluded from the statistical averaging. The results from the material without cells are presented for comparison.

	Points	MgO (wt%)	P_2O_5 (wt%)	CaO (wt%)	Na_2O (wt%)	SO_2 (wt%)	Cl (wt%)	Total oxide (wt%) via EMPA
Immersion medium:								
DMEM	10	24 ± 8.6	25.4 ± 8.2	6.05 ± 2.7	0.9 ± 0.6	0.3 ± 0.1	0.15	57 ± 9
DMEM + OB	7	14.01 ± 6.9	2.2 ± 1.5	2.6 ± 1.5	0.18 ± 0.8	0.1	0.34 ± 0.1	33.30 ± 7.2
Reference compounds:								
$MgCO_3$		~ 47						~ 47
$Mg(OH)_2$		~ 66						~ 66
$MgC_2O_4.H_2O$		~ 33						~ 33
$Ca_5(PO_4)_3OH$			~ 42	~52				~ 94
$NH_4MgPO_4.6H_2O$		~ 16	~ 29					~ 54

4.4. Degradation layer thickness under all immersion conditions

To get an illustration about the influence of the different conditions on the degradation layer thickness, the degradation layer thickness for pure magnesium samples was measured in the different immersion conditions (see Figure 4.23). The results were obtained from 50 measured points on the sample cross-sections using an optical microscope. Calcium influence in reducing the layer thickness was observed when the immersion was performed under a simple salt condition. In cell culture media where higher complexity is existent due to the presence of other organic constitutes, which are essential for cell growth and activity, a relatively thicker degradation layer was observed when comparing these conditions to calcium and sulphate additions to HBSS conditions. The difference between RPMI and DMEM can be a result of the difference in bicarbonate, which is higher in DMEM Glutamax than in RPMI-1640, besides the differences in the organic constitutes. Culturing osteoblasts directly on the sample surface seemed to reduce the layer thickness. One can assume that cell layer formation and adhesion lead to less interaction between the immersion medium and the material, which leads to this reduction in layer thickness.

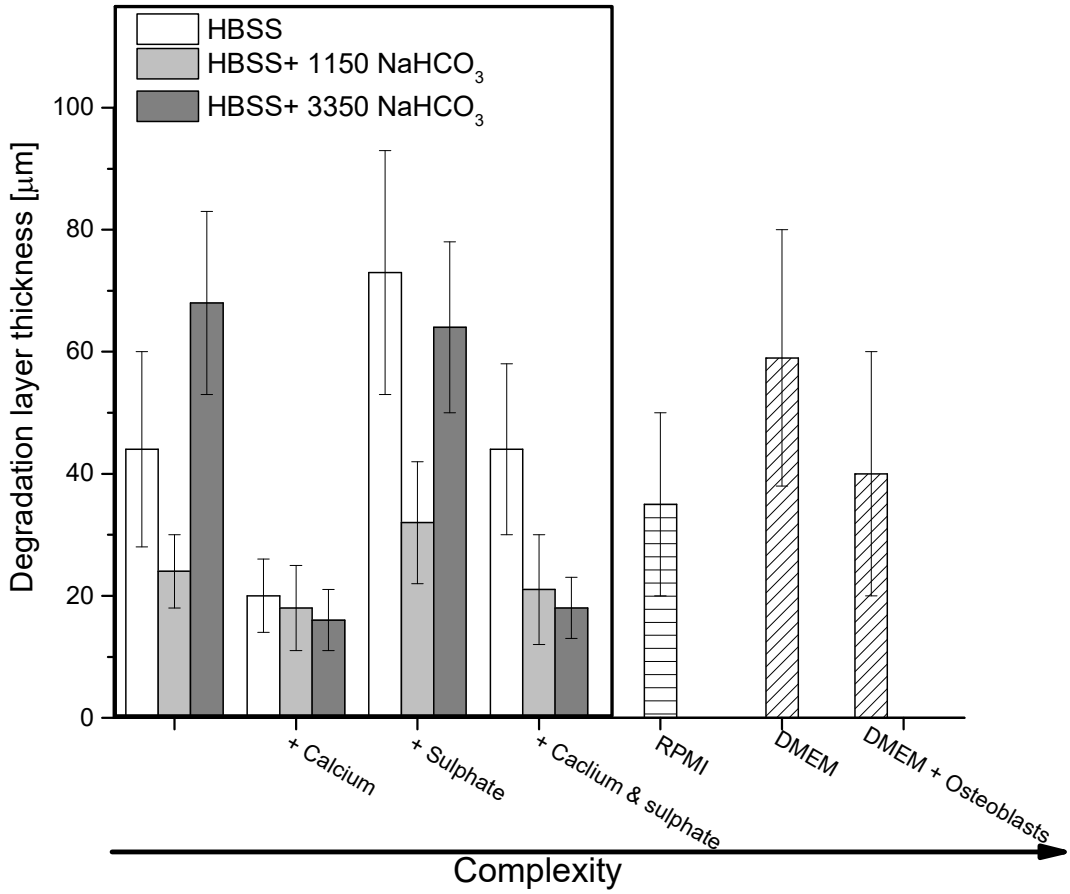

Figure 4.23: The degradation layer thickness of pure magnesium samples immersed in the different studied conditions. Measurements are the mean of 50 measured points on the sample cross-sections using an optical microscope.

5. Discussion

5.1. Influence of salts on pure magnesium degradation

Many early papers studied the degradation of magnesium alloys and revealed a lack of correlation between *in vivo* and *in vitro*. Thereafter, many *in vitro* studies focused on filling this gap by simulating physiological conditions using cell culture formulations, which leads to more complexity in the degradation process and its products. In this section, the aim is to first determine the influence of three important buffering salts used in cell culture media on Mg degradation. To accomplish this, a simple salt solution (HBSS) without calcium or magnesium plus 10% FBS was used as a base solution. Environmental conditions were controlled by performing the immersion under physiological parameters (37°C, 20% O_2, 5% CO_2, 95% rH). Based on these preliminary findings, the results of using more complex salt formulation in two cell culture media is discussed, and the influence of high phosphate concentration in the immersion media is defined.

5.1.1. Influence of sodium bicarbonate

Sodium bicarbonate is dissolving readily in water. Increasing the concentration of bicarbonate from 4.2 mM to 22 mM and then to 44 mM had no significant influence on the degradation rate for samples 1-3 (Figure 4.2). The main degradation product for these samples was $MgCO_3$ (Figure 4.8 and Table 4.3). This can be explained by the following reactions:

Oxidation of Mg:

$$Mg_{(s)} \rightarrow Mg^{2+}_{(aq)} + 2e^- \quad (1)$$

Reduction of water:

$$2H_2O_{(l)} + 2e^- \rightarrow H_{2(g)} + 2OH^-_{(aq)} \quad (2)$$

Precipitation of $MgCO_3$ according to the following reaction:

$$Mg^{2+}_{(aq)} + HCO_3^-{}_{(aq)} \rightarrow MgCO_{3\,(s)} + H^+_{(aq)} \quad (3)$$

Based on these formulas, the global reaction is:

$$Mg_{(s)} + HCO_3^-{}_{(aq)} + H_2O_{(l)} \rightarrow MgCO_{3\,(s)} + H_{2(g)} + OH^-_{(aq)} \quad (4)$$

This was found in other studies where degradation was performed under physiological conditions with a supplement of 5% CO_2. Therefore, the global reaction is shifted to the right and $MgCO_3$ formation is more forced [124, 125]. This explains the presence of $MgCO_3$ in all corroded samples. Furthermore, the continuous supplement of CO_2 in combination with HCO_3^- is a buffering system comparable to blood. The following reactions are included [126]:

$$CO_{2(g)} + 2H_2O_{(l)} \leftrightarrow HCO_3^-{}_{(aq)} + H_3O^+_{(aq)} \qquad pK2=6.31 \qquad (5)$$

$$HCO_3^-{}_{(aq)} + OH^-_{(aq)} \leftrightarrow H_2O_{(l)} + CO_3^{2-}{}_{(aq)} \qquad pK1=10.25 \qquad (6)$$

This system has an equilibrium pH = 8.28 given by pH = 0.5 (p*K1* + p*K2*). The pH value increased after the magnesium discs were immersed for 10 day in all solutions, which can be explained by equation 6.

The composition of the degradation products revealed that for sample 1, the main performed product was crystalline $MgCO_3$. An increase in the bicarbonate concentration (sample 2) led to predominantly amorphous $MgCO_3$ integrated with Mg/Ca phosphate. A further increase of HCO_3^- seemed to suppress these phosphate phases on the account of carbonate. For samples 1-3, $MgCO_3$ was the main performed product. Its solubility constant can be estimated according to [127]:

$$K_{sp}\ (MgCO_3) = [Mg^{2+}] + [CO_3^{2-}] \qquad (7)$$

where $[CO_3^{2-}]$ is calculated from the equation:

$$[CO_3^{2-}] = C_{total}\ (CO_3^{2-})\ K_{a1}\ K_{a2} / [H^+]^2 + [H^+]\ K_{a1} + K_{a1}\ K_{a2} \qquad (8)$$

where K_{a1} and K_{a2} are the dissociation constants of H_2CO_3 and HCO_3^-, and C_{total} is the total carbonate concentration in the media, which for samples 1, 2 and 3 is 4.2, 22, and 44 mM, respectively. According to equation 7, the higher the $[CO_3^{2-}]$ concentration, the more stable $MgCO_3$ is formed [128]. Equation 8 shows that the CO_3^{2-} concentration depends on pH because with increasing C_{total} concentration, pH increases, which explains the initial pH values for all solutions [129]. However, during the immersion, the pH value increased by the degradation process and was controlled by the buffering system of CO_2. This effect was better pronounced for all samples with x $NaHCO_3$ additions (i.e., x=1150, 3350 mg/L additions) due to a higher HCO_3^- presence.

5.1.2. Influence of calcium chloride

Calcium and phosphate have an important role in the biomineralisation process. HBSS without calcium or magnesium was used with x $NaHCO_3$ (x=0, 1150, 3350 mg/L). The calcium addition reduced the degradation rate. This effect was more pronounced by increasing the bicarbonate concentration (see Figure 4.2, samples 4 and 6 after 240 hours). It is well known that carbonate has a role in contributing to and structuring Ca-PO_4 precipitates on the magnesium surface [130]. This can be observed by the higher values of CaO wt% in the interface layer for samples 5 and 6 compared to sample 4 (Table 4.3) as well as by the fact that the CaO/P_2O_5 ratio for samples 5 and 6 is close to that of apatite, which indicates the formation of carbonate apatite-based precipitations that are comparable to those discussed in [130].

Amorphous $MgCO_3$, and Ca-PO_4 phases was detected from samples with calcium additions. These depositions can be the substrate of apatite precipitation. This was reported in some biological cases in which apatite had poor crystallinity and nonstoichiometry and was explained by the presence of a significant number of foreign ions, such as Mg^{2+}, HCO_3^-, Na^+ and Cl^-. Some of these ions enter in the apatite crystal lattice whilst others are only adsorbed on the apatite surface [131]. These types of precipitates had an influence on protecting the implant surface from further excess oxidisation over time because their deposition forms a homogenous protecting layer with low solubility on the magnesium surface [131-133]. This explains the decreases in the degradation rate (Figure 4.2) and magnesium concentration (Table 4.2) in the immersion media when comparing samples 1 and 4, for example.

5.1.3. Influence of magnesium sulphate

Adding magnesium sulphate within the physiological range had no significant influence on the degradation rate (see Figure 4.2). $MgSO_4$ is highly soluble in water, meaning that it will dissociate to its ionic species Mg^{2+} and SO_4^{2-}. One can assume that the free magnesium ion might react in the same way of that dissolved from metal by oxidisation, whilst sulphate had an influence on the morphology of the interface layer by forcing its inhomogeneity and inducing pitting. This could be observed for all samples exposed to sulphate (see Figure 4.6 and Figure 4.7, samples 7-11). This is comparable to other studies in which sulphate was found to stimulate magnesium dissolution with n=2 stoichiometry (Mg^{2+}) [134, 135]. Zeng et al. studied the influence of sulphate on AZ31 magnesium alloy degradation in a saline solution (NaCl concentration: 153 mM) and found that an increase in sulphate concentration (0.24, 0.48, 0.81 mM) accelerated the hydrogen evolution and induced severe pitting corrosion. The main degradation product was $MgO/Mg(OH)_2$ in a simple salt solution in the absence of phosphate and bicarbonate [136, 137]. However, in this thesis work, the immersion conditions were close to the physiological ones in which carbonate and phosphate salts exist. IR spectra for samples immersed in presence of magnesium sulphate showed amorphous Mg-PO_4 with noisy signals around $MgCO_3$. This signal was better pronounced and less noisy when the bicarbonate concentration was increased, where a crystalline magnesium carbonate phase was detected. This crystalline phase formation had further influence on reducing Mg concentration in the immersion medium after 3 days (Table 4.2).

5.1.4. Influence of calcium chloride and magnesium sulphate together

In comparison, the degradation rate for samples of this conditions were in the same range as those of samples in which $CaCl_2$ was the significant salt added, but with more heterogeneous morphology and porosity of the interface layer caused by SO_4^{2-} (Figure 4.7).

The FTIR results in Figure 4.8d showed the effect for both $CaCl_2$, with its role in Ca-PO_4 formation, and $NaHCO_3$, with its contribution to enhance $MgCO_3$ precipitation. This is well noted in sample 11, where two peaks correspondent to these phases were measured.

5.1.5. Influence of salt complexity in cell culture media (DMEM and RPMI)

In this section, the results of using three media (the composition is shown in Table 3.3) are discussed. It should be noted that the $NaHCO_3$ concentrations of 4.2, 22, and 44 mM for samples 1, 11, and 12 are comparable to HBSS (the basal medium in section 1), RPMI, and DMEM, respectively. The degradation rate showed that DMEM and RPMI had significantly lower values compared to HBSS, and this can be related to the influence of calcium on $NaHCO_3$, which was discussed in section 5.1.2. Online pH values for media controls shown in Figure 4.9 A can be explained with equation 8, where the higher concentration of carbonate led to higher pH values in the immersion medium [127, 129]. However, when the degradable pure magnesium samples were immersed in the media, this behaviour changed. The highly corrosive HBSS led to a high pH and therefore to higher osmolality values, whereas the low values of degradation in RPMI combined with the moderate bicarbonate buffering effects showed the lowest pH values compared to the other two media. In agreement with these results, Xin et al. suggested that bicarbonate concentration has a crucial role in degradation. When the bicarbonate concentration exceeded 12 mM, a rapid surface passivation due to magnesium bicarbonate precipitation occurred, but for lower values, degradation was not prevented. Jang et al. studied the influence of a high bicarbonate concentration (maximum 50 mM) on magnesium alloy AZ31 (as drawn) and found that increasing the bicarbonate concentration increased the magnesium degradation and the degradation layer thickness with micro-cracks [138]. This was comparable to the layer thickness results in Figure 4.23.

The chemical composition of the degradation interface in these cell culture media was further examined (see Figures 4.10 - 4.12 and Table 4.5). For the samples immersed in HBSS, the chemical composition was discussed in section 5.1.1. This composition was crystalline $MgCO_3$, which was confirmed with the SEM images on the sample surface (Figure 4.10). The results on samples immersed in DMEM and RPMI revealed PO_4 and CO_3 precipitations according to the IR reflection results (Figure 4.12). The EMPA analysis on DMEM (Table 4.5) showed no predominant phase and revealed the presence of Mg, Ca, and P oxides. Jang et al. reported a deposition of octacalcium phosphate and hydroxyapatite (HA) on a magnesium surface when PO_4^{2-} and Ca^{2+} were present together in a sodium salt solution. It was shown that this deposition increased corrosion resistance [138]. However, the precipitation of calcium phosphate from a supersaturated solution is complex phenomenon in which several phases can precede the formation of the most

thermodynamically stable phase [139]. In addition, the precipitation efficiency of the calcium phosphate phase is pH dependent and is reported to be higher at a controlled pH than at a drifting one [140]. Therefore, the buffering effect of the physiological conditions might positively affect this precipitation. Mekmene et al. studied the influence of the Ca/P molar ratio in an aqueous solution on calcium phosphate precipitation and reported that in the initial solution, Ca/P = 1.5 gave the highest calcium phosphate precipitation efficiency, but when the Ca/P was 1.00, calcium concentration was the limiting factor, and when the initial Ca/P was 2.00, phosphate concentration was the limiting factor [140]. In DMEM, the calculated initial Ca/P is 2.00, whilst in RPMI it is 0.07. This can explain the different oxide phases obtained by EMPA for DMEM. The high phosphorus concentration over calcium in RPMI composition produced magnesium phosphate precipitation as the predominant phase in the EMPA analysis (see Table 4.5). Another important factor that can influence the crystallinity of calcium phosphate is the presence of organic ligands in the immersion medium [141, 142]. For example, it was found that the presence of citrate affects both the crystal size and the degree of perfection of the lattice cell, where the HA was found to consist of small crystallites and to contain carboxyl groups and a higher concentration of impurities. However, the crystalline HAP formation was not totally inhibited [143]. This might explain the amorphous phases detected with the reflected IR because the immersion media were always supplemented with proteins (10% FBS).

In summary, a moderate bicarbonate addition (~ 22 mM) is influential in reducing degradation by the formation of $MgCO_3$, but when the bicarbonate is increased to a high concentration, degradation increased (i.e., DMEM compared to RPMI) and the degradation layer thickened (Figure 4.23). Sulphate had a role in increasing the degradation layer's heterogeneity. Calcium in the presence of phosphate (as one constitute in the media formulation) led to a reduction in degradation by forming a layer that primarily consisted of calcium phosphate. However, the defined structure and composition of this phase are dependent on the medium's initial Ca/P ratio; with a high phosphate concentration in the cell culture medium, the predominant detected phase was magnesium phosphate. Therefore, the salt composition of the cell culture medium should not be neglected.

5.2. Magnesium degradation under direct cell interaction

The influence of primary human osteoblasts on the degradation interfaces of Mg-2Ag, Mg-10Gd, and pure Mg were studied. It is clear that osteoblasts have a role in bone formation by inducing and regulating the mineralisation of the extracellular matrix, the inorganic part of which is based on hydroxyapatite [144, 145]. However, before stating any influence by the cells, it was important to give two introductory paragraphs. In the first paragraph (5.2.1), simple solubility calculations were performed and presented to justify the possibility of HA precipitation under cell culture conditions in DMEM. This is important in order to explain the results of the mineralisation staining and also the chemical composition of the degradation interface for control samples (samples without cells), and then state the active chemical influence of the cells. In the second paragraph (5.2.2), the influence of the microstructure was discussed since the different materials pure Mg, Mg-2Ag, and Mg-10Gd were mainly used in this part of the study, and it was found more relevant to discuss this influence in it.

5.2.1. Influence of the immersion medium composition on Ca-PO_4 precipitation

Numerous studies have shown that the formation of Ca-PO_4 is a complex phenomenon and may lead to the formation of different phases, such as dicalcium phosphate (DCP), octacalcium phosphate (OCP), β–tricalcium phosphate (β–TCP), and hydroxyapatite (HA), depending on the experimental conditions. The most important parameters that directly influence precipitation include temperature, phosphate and calcium concentrations, ionic strength, the presence of other interfering ions and macromolecules during precipitation, and pH. In our study, the pH changes were measured online throughout the immersion period (Figure 4.13). Samples without cells results demonstrated that the buffering system generally controlled the pH in a range of 8 to 9. Fernandez et al. studied the solubility isotherms for the $Ca(OH)_2$-H_2PO_4-H_2O system at 37°C and found that HA is the most stable phase at approximately pH 8.5, followed by β-TCP [110].

Table 5.1: Saturation level index for different Ca-PO_4 phases according to the immersion medium parameters.

Solution parameters			
Ionic strength 0.15 [M]	Temperature 37°C	Ca/PO_4 1.97	at pH 8.3
Saturation level (S)		**K_{sp} at 37°C**	**SI = log(S)**
HA: $(Ca^{2+})^5(OH^-)(PO_4^{-3})^3/\ K_{HA}$		7.36×10^{-60}	26.03
β–TCP: $(Ca^{2+})^3(PO_4^{-3})^2/K_{TCP}$		2.83×10^{-30}	12.36
OCP: $(Ca^{2+})\ ^4(H^+)(PO_4^{-3})^3/\ K_{OCP}$		1.05×10^{-47}	8.36
DCP: $(Ca^{2+})\ (PO_4^{-3})/\ K_{DCP}$		9.54×10^{-8}	0.30

The calculated saturation index indicated that all phases can exist at these specific conditions (Table 5.1). The most stable phase is HA, followed by β–TCP, OCP, and DCP. These calculations indicate the precipitation of possible Ca-PO_4 phases for the medium composition and conditions (i.e., pH and T) used in this study. However, sample degradation will continuously change the surrounding environment, and this change is likely very heterogeneous. For example, the pH may be higher near the material surface, which may affect the favourability of the precipitation of one phase over another. The influence of the dissolved Mg and other alloying elements from the samples was not considered, which can change the solution and either increase or reduce the nucleation and growth of different phases. For example, monovalent ions, such as HCO^{3-}, Na^{+} and Cl^{-}, can reportedly influence the nucleation and growth of precipitated apatite, as indicated in many studies in which amorphous apatite was detected in various biological tissues. This apatite exhibited poor crystallinity and was nonstoichiometric, which was explained by the presence of a significant number of foreign ions. Some of these ions enter the apatite crystal lattice, whilst others are only adsorbed to the apatite surface [130-132, 146]. Gadolinium is classified as a lanthanide element that has been shown to associate with bone [90-93]. This was shown in our results (see Figure 4.20) in which Gd was associated with Ca and P precipitation, whilst silver was dissolved mainly in the media (Figure 4.17, and 4.20). One important factor concerning silver is the presence of chloride in the immersion medium (in DMEM, 117.5 mM) because these ions were proven to increase silver dissolution [147].

5.2.2. The influence of microstructure on material degradation

Before discussing the influence of pure Mg, Mg-2Ag and Mg-10Gd degradation on the metabolic activity of the cells and consequently the influence of cells on degradation, it is important to state the influence of the studied materials' microstructures on their degradation. One can assume that the effect of the microstructure on degradation is more evident during short-term immersion, where the degradation products precipitate and other physiological influences, such as protein adhesion, are less effective compared to 14 days of immersion. The Mg-2Ag alloy showed a relatively slight increase in grain size compared to the other studied materials. Liu et al. studied the influence of the grain size of pure magnesium on corrosion resistance, where a cooling-rate controlled solidification was performed to obtain the different microstructures with different grain sizes [53]. They found that corrosion resistance improved as the grain size decreased; this improvement was attributed to the ability of the fine grains' microstructures to produce a more uniform and dense degradation product layer on the surface. This can explain the results at 3 days of immersion, when a relatively higher degradation rate was observed on Mg-2Ag compared to the other two materials. Another important parameter that influences degradation behaviour

is the presence of secondary phases. Tie et al. reported that after heat treatment on the Mg-2Ag alloy, the secondary phases were dissolved in the matrix (α-Mg) and galvanic corrosion induced by the existence of these phases was hindered [59]. Many studies on Mg-Gd binary systems have reported the presence of Mg_5Gd and/or GdH_2 as intermetallic phases after heat treatment [37, 148]. These metallic phases have an influence on strengthening the alloy; however, their presence can induce galvanic corrosion. This can explain the slight increase in the degradation rate for Mg-10Gd at 3 days compared to pure Mg.

5.2.3. The interaction (material degradation - cell metabolic activity)

The presence of a degradable material can influence the natural functions of osteoblasts. Recent work has investigated the influence of pure magnesium degradation on primary human osteoblasts in a direct contact test for four weeks in a differentiating medium. Specifically, osteocalcin, osteopontin and bone sialoprotein were upregulated, which clearly indicated an active mineralisation process. When this experiment was carried out with titanium samples, the gene expression levels of these proteins were lower, which revealed that magnesium itself influenced osteoblasts and induced osteoinductive properties [149]. These findings suggest a mechanism by which the cells in our study changed the chemical composition of the degradation interface, although osteogenic differentiation factors were not used in our medium. Alternatively, the metabolic activity of the cells may affect the degradation interface because this activity is combined with the formation and release of lactate into the surrounding environment. This action can negatively influence the degradation of magnesium materials by lowering the pH. Kanan et al. studied the influence of L929 fibroblast-derived cell line on the Mg-Ca alloy. The maximum immersion time was 48 hours. The study showed that pH values were lower when samples were immersed with cells than without cells. This difference was explained by the influence of lactic acid, which is produced during cell metabolism; consequently, an increase in the degradation rate was observed [79]. L929 cells were included in our study as a control and to assess the specificity of the influence of the materials on the OB metabolic activity and vice versa. As shown in Figure 4.14 A, the pH values were lower for the L929 samples than for the OB samples during the first 125 hours, indicating a particularly high initial proliferation rate of L929 cells compared with OB. As a result of this rapid proliferation, more lactate was formed, which decreased the pH. In this part of the experiment, the material/OB cell interaction on the degradation interface was determined, and the following observations were made for each studied material.

Pure Mg

The LDH activity in the medium was low during the first day of immersion, suggesting that the reactivity between the material and the medium was initially low; however, the cytotoxicity subsequently increased on days 2 and 3 and decreased thereafter, indicating that the cells tolerated degradation influence. This high initial metabolic activity within the first days of immersion was combined with low pH values for the **SC** sample compared with the negative control. The pH of the **SC** sample was maintained at approximately 8.3 thereafter. In addition to their role in mineralisation, OB can adhere and extend to form a cell layer that might decrease the interaction between the material and the medium and consequently control or even reduce the pH. The SEM images of pure magnesium samples after 14 days of immersion showed a non-continuous cell layer that likely resulted from the degradation morphology of the magnesium samples (see Figure 4.20). Those findings on the surface morphology corroborated the EDX line measurements of the **SC** cross-sections; specifically, the influence of cells on mineralisation was non-homogenous and resulted in a layer richer in Ca and P near the cells than underneath the cells (see Figure 4.21).

Mg-2Ag

Mg-2Ag showed a relatively high degradation rate induced by the microstructure of this alloy and the relatively high concentration of impurities (Table 3.1). One can assume that this initial high material degradation was combined with Ag^+ release into the immersion medium. The LDH activity measurements showed the influence of this initial reactivity on cytotoxicity, which was high during the first two days of immersion compared with pure Mg and Mg-10Gd (Figure 4.17); however, the LDH activity subsequently decreased as immersion continued. The SEM images of Mg-2Ag after 4 days of immersion corroborated the cytotoxicity results, showing blebs indicating cell stress or damage (blebbing). It has been previously reported that bleb formation is not only a hallmark of apoptosis or necrosis but also indicates cells injured by physical or chemical stress [150, 151]. These cytotoxic effects seemed to delay the effect of OB on mineralisation, as shown in Figure 4.18 and in the EDX line measurement in Figure 4.21. Moreover, cells on this alloy negatively impacted the degradation process, as shown by an increase in the pH combined with an increase in material degradation. Many studies have shown that silver nanoparticles are cytotoxic in different *in vitro* and *in vivo* systems [152, 153]. Albers et al. concluded that cytotoxicity to both primary mouse OB and murine osteoclasts (OC) is primarily mediated by silver ion release. Their study also described the negative effect of Ag^+, which decreased the differentiation and viability OB and OC [154]. These findings were consistent with a study by Contreras et al., who used $Ag(NH_3)_2F$ salt as a donor for Ag^+ ions, which were cytotoxic to mouse MC3T3-E1 osteoblasts. Specifically, $Ag(NH_3)_2F$ induced cell death after 24 h in 50%

of the cells at a concentration of 0.0096 mM, which is almost 5 times lower than the concentration reported by Albers [155]. These differences in the silver concentration tolerated by the cells are attributed to differences in the analytical assays, the silver salts that were used, and the cell culture systems. For example, other studies of different human cells showed that silver induced cell cycle progression, DNA damage, and apoptosis. However, at specific low concentrations, the cell proliferation, mitochondrial activity, and cell viability were not affected [156]. This can explain the initial cell damage observed on the Mg-2Ag alloy, which was then followed by cell proliferation rather than differentiation, as evidenced by the mineralisation shown in Figures 4.18 and 4.21.

Mg-10Gd

The potential effects of Gd on bone metabolism are not well understood. Zhang et al. studied the effect of $GdCl_3$ on the proliferation, differentiation and calcification of primary mouse osteoblasts *in vitro* [157]. The effect of Gd on bone metabolism was found to be complex, and the concentration and culture time are key factors for assessing the biological role of Gd. Wang et al. studied the influence of Gd complexed with inorganic polyphosphate (polyP) and compared the influence of polyP.Gd with polyP and $GdCl_3$ on hydroxyapatite formation in SaOS-2 cells *in vitro*. Those compounds were found to be non-toxic at concentrations of up to 30 µM. At a low concentration of 5 µM, it was found that polyP.Gd and to a lesser extent polyP and $GdCl_3$ caused HA crystal formation arranged in a nest-like shape, which suggests that Gd^{3+} causes an initiation of a differentiation pathway for osteoblasts with a sequential expression of specific osteoblast markers [158]. Those findings can be correlated to the results in our study in which Mg-10Gd degradation was minimally cytotoxic to OB after one day of immersion (Figure 4.17). The low pH values after 3 days of immersion compared with the negative control indicated the high metabolic activity of OB (Figure 4.14C). The results in Figure 4.17 show an increase in and homogenous distribution of mineralised matrix precipitation in the presence of cells. This observation corresponds with the EDX measurements of the cross-sections; i.e., the degradation interfaces near and underneath the cells exhibit associated Ca and P (see Figure 4.21).

For this part of the study, the following observations were recapitulated (see Figure 5.1) for each studied material by closely assessing the material/OB interaction at the degradation interface:

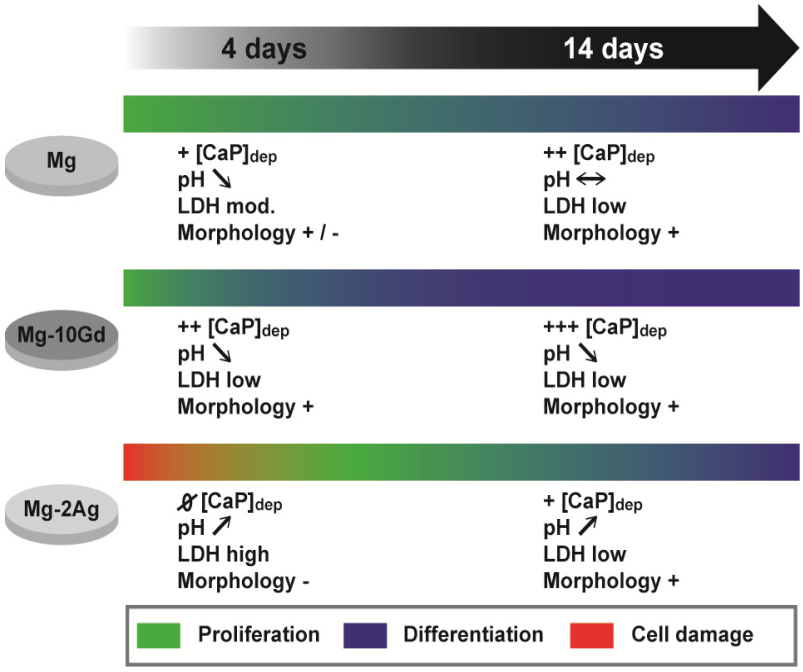

Figure 5.1: Recapitulation of all observations on pure Mg, Mg-2Ag, and Mg-10Gd with direct OB contact at 4 and 14 days of immersion. The results, including calcium – phosphate deposition ($[CaP]_{dep}$), pH, LDH activity and cell morphology, and their correlations with cells metabolic activity are presented.

Figure 5.2 plots cell cytotoxicity verses layer thickness. The layer thicknesses were determined from the measured points on the processed microcross-sections near to the cells, under the cells, and in the control samples without cells in Figure 4.21. It should be noted that the resulted layer thickness might be an influence of multiple parameters. In the case of Mg2Ag all conditions show comparable values, this might refer to the fact that the degradation behaviour of this material is the main influence on layer thickness and cell behaviour. In contrary the results of Mg10Gd show a completely change in layer thickness in presence of cells comparing to the control samples, which reflect that the cells had the main influence by rolling an active mineralisation process and forming passive adhesion layer. In comparison to Mg-10Gd, pure Mg show a thicker layer under the cell which might be related to cell cytotoxicity influence beside the cell presence which can increase the interface thickness. However near to the cell the layer was thinner and according to the EDX line scans more deposition of calcium phosphate phases, which reflected more active mineralisation influence near rather than under the cells.

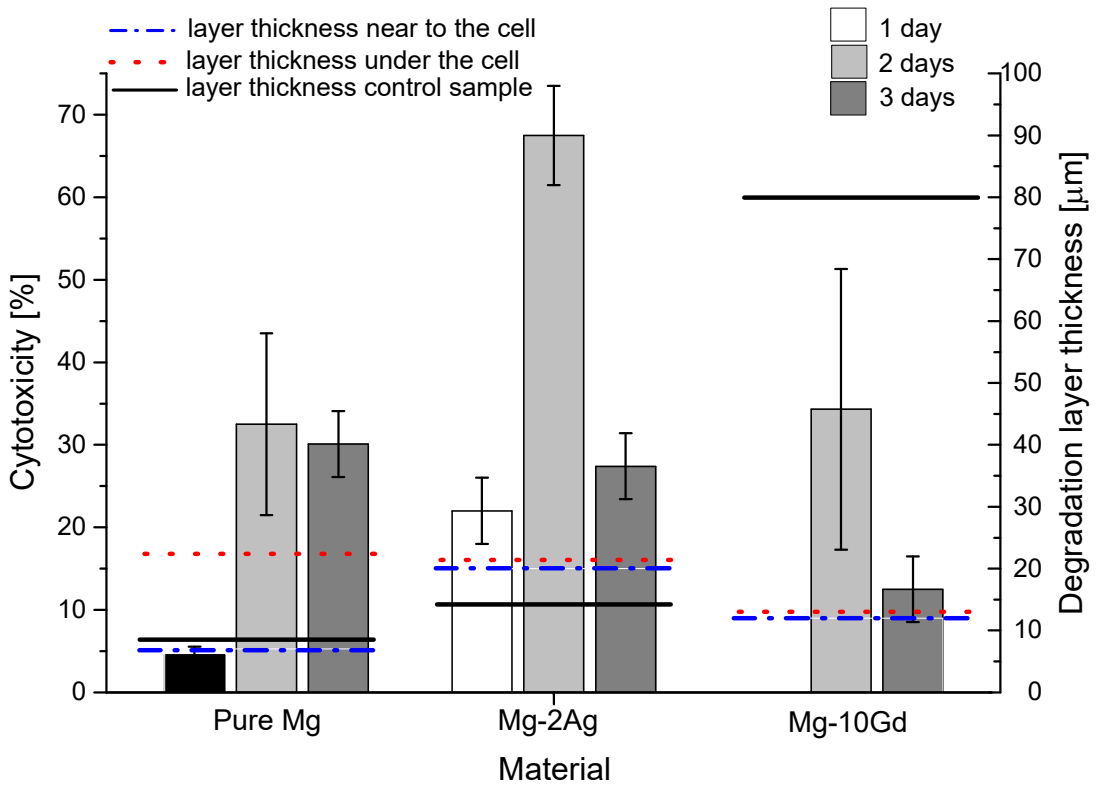

Figure 5.2: The cell cytotoxicity induced by the direct interaction of the different materials verses the degradation layer thickness under and near to the cell, and for control sample. Layers thicknesses were obtained from the FIB/EDX measurements after 14 days of samples immersion.

5.3. General Discussion

An illustration for magnesium degradation from simple to complex conditions

The typical mode of degradation in Mg-based biomaterials is through a corrosion process. Corrosion is generally induced by an electrochemical reaction with an electrolyte, leading to the formation of oxides, hydroxides, and hydrogen gas.

After coming in contact with fluid, magnesium is oxidised into metal cations following the anodic reaction (path 1 in Figure 5.2) [21]:

$$Mg_{(s)} \rightarrow Mg^{2+}_{(aq)} + 2\,e^{-} \quad (9)$$

Under water interaction and atmospheric conditions, the generated electrons are consumed by a cathodic reaction corresponding to the water reduction and hydrogen gas release (path 2 in Figure 5.2)[4]:

$$2\,H_2O_{(aq)} + 2\,e^{-} \rightarrow H_{2(g)}\uparrow + 2\,OH^{-}_{(aq)} \quad (10)$$

$Mg(OH)_2$ as a degradation product is the expected to form on the material surface according to the overall reaction (path 3 in Figure 5.2) [21]:

$$Mg^{2+}_{(aq)} + 2OH^{-}_{(aq)} \rightarrow Mg(OH)_{2\,(s)} \quad (11)$$

In the presence of chlorine, pitting corrosion through the magnesium base can occur, and $MgCl_2$ is formed (path 4 in Figure 5.2) [21]:

$$Mg_{(s)} + 2\,Cl^{-} \rightarrow MgCl_{2\,(s)} + 2\,e^{-} \quad (12)$$

Furthermore, chlorine can react with the degradation product $Mg(OH)_2$ (path 5 in Figure 5.2) [21]:

$$Mg(OH)_{2\,(s)} + 2\,Cl^{-}_{(aq)} \rightarrow MgCl_{2\,(s)} + 2OH^{-}_{(aq)} \quad (13)$$

The stability of the $Mg(OH)_2$ as a degradation product depends on the solution pH, where a more alkaline pH makes the precipitated film more passive [159]. The calculated pH in a saturated solution for $Mg(OH)_2$ precipitation is 10.32; therefore, lowering the pH by one degree will increase the dissociated Mg^{2+} from $Mg(OH)_2$ by a factor of 100 [127]. Therefore, under physiological conditions, where 5% CO_2 supplement and bicarbonate salt exist, the buffering agent (HCO_3^-/CO_3^{2-}) controls the pH in physiological range where $MgCO_3$ is more stable than $Mg(OH)_2$ [128]. This was found in the results, where $MgCO_3$ formation as the main degradation product, even with a low concentration of bicarbonate (4.2 mM, in the case of HBSS), was recorded (path 6 and 7 in Figure 5.2), where the overall reaction is:

$$Mg_{(s)} + HCO_3^{-}{}_{(aq)} + H_2O_{(l)} \rightarrow MgCO_{3\,(s)} + H_{2(g)}\uparrow + OH^{-}{}_{(aq)} \quad (14)$$

Furthermore, the cell culture media (CCM) are aggressive due to the high concentration of chlorine ions in addition to the presence of sulphate, which is critical to the metallic

degradation protective layer. The results of this work showed that sulphate did not increase the degradation, probably due to the formation of protecting precipitation layer, but increased the heterogeneity of this layer (path 8 in Figure 5.2) [134, 138].

As the complexity increases, other biomineralisation elements can exist. Elements such as phosphate can react with the dissolved Mg^{2+} to form magnesium phosphate precipitation (path 9 in Figure 5.2). This type of precipitation can further passivate the material surface and reduce the degradation (the solubility product of $Mg_3(PO_4)_2$ is 1.0×10^{-25} compared to 6.82×10^{-8} for $MgCO_3$) through a reaction based on [136]:

$$3\,Mg^{2+}_{(aq)} + 4\,OH^- + 2\,H_2PO^-_{4\,(aq)} + (n\text{-}4)H_2O \rightarrow Mg_3(PO_4)_2.\,nH_2O \qquad (15)$$

The existence of calcium in addition to phosphate ions leads to calcium phosphate-based apatite deposition on the undissolved carbonated degradation layer due to the localised alkalisation and saturation of calcium and phosphate in the surrounding bodily fluid (path 10 in Figure 5.2) [138]. The results showed that the formed apatite depositions had poor crystallinity, and nonstoichiometry primarily resulted from the presence of significant amounts of Mg^{2+}, CO_3^{2-}, and proteins [130, 133, 142, 143, 160]. The precipitation reaction base for HA is [111, 138]:

$$10\,Ca^{2+}_{(aq)} + 6\,H_2PO_4^{3-}{}_{(aq)} + H_2O \rightarrow Ca_{10}(PO_4)_6OH_{(s)} + 13\,H^+ \qquad (16)$$

Results of this work demonstrated that the Ca/P ratio of the simulating physiological media *in vitro* is critical for the apatite deposition. For example, this study showed that the low Ca/P value in RPMI due to the high phosphate concentration led to formation of magnesium phosphate- based precipitations over apatite.

Increasing the system complexity even more by including cells can lead to further alterations in the degradation according to the cells' specific natural roles. The influence is derived from the biochemistry reactions in which the cells are involved in. In addition, cell adhesion can passivate the material surface to some extent by simply reducing the material/medium interaction. With the progressing immersion time, the adhered proliferated cells can form tissues adjacent to the degradation product layer. The results of this work showed that osteoblasts lead to enrichment of the degradation interface layer of magnesium with apatite (path 11 in Figure 5.2). Furthermore, the results showed that the alloying elements for magnesium had cross-interactions with these cells.

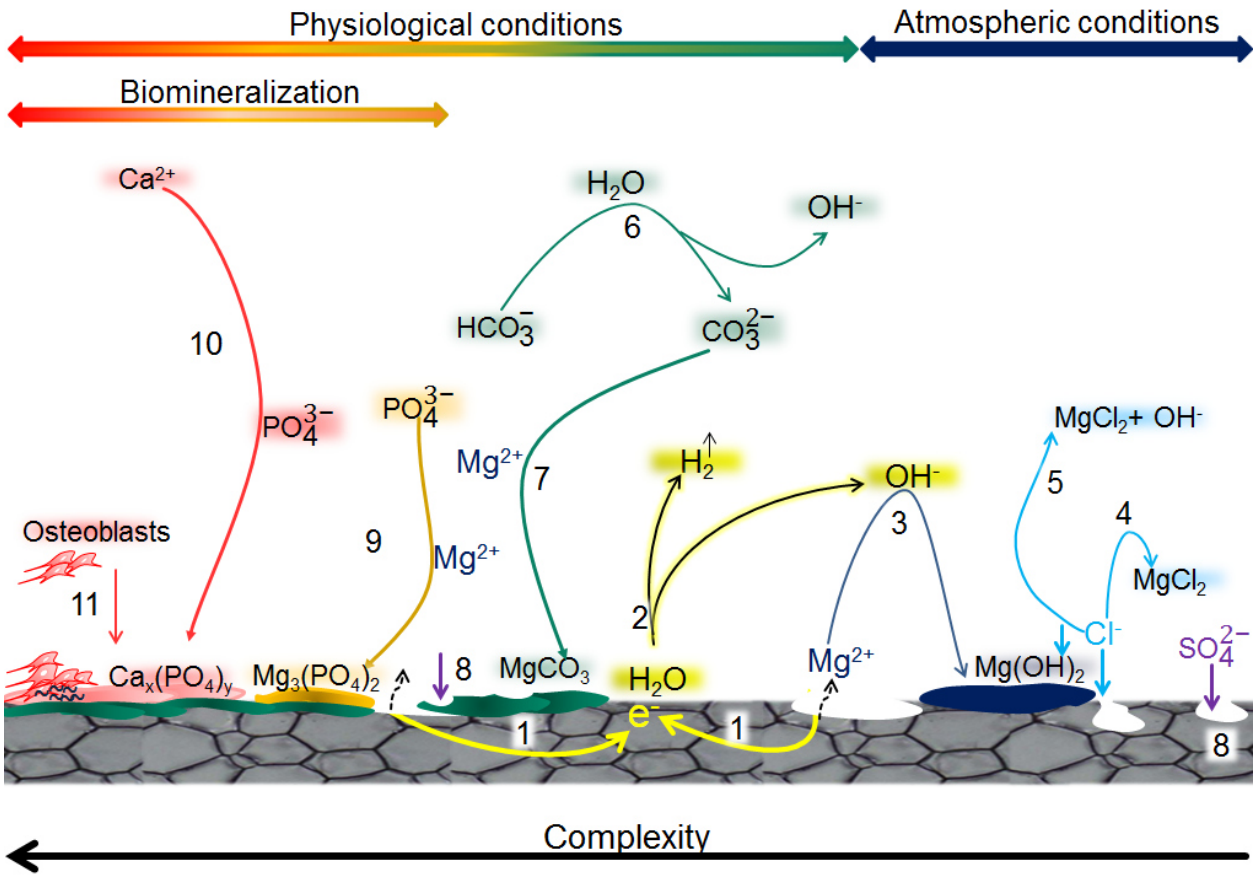

Figure 5.3: Schematic illustration of magnesium degradation from simple environmental to complex physiological conditions. The following reaction and product formations are illustrated: (1) Material dissolving by anodic reaction. (2) Water reduction and hydrogen release. (3) Formation of $Mg(OH)_2$. (4) Pitting corrosion and material degradation by Cl^-. (5) Reactivity of Cl^- with $Mg(OH)_2$. (6) The existence of CO_3^{2-} under physiological conditions that induce the formation of $MgCO_3$ (7). (8) The influence of sulphate ions on increasing the morphological heterogeneity of the degradation layer. The presence of biomineralisation elements in body fluid in which PO_4^{3-} will induce the formation of $Mg_3(PO_4)_2$ as a degradation product (9), and in combination with Ca^{2+}, this will induce the formation of calcium phosphate phases (10). (11) Osteoblast cells forcing the biomineralisation process and leading to hydroxyapatite formation.

6. Summary and conclusions

In this study, the influence of important inorganic salts in blood plasma on magnesium degradation was studied in. A simple salt solution (HBSS) without calcium or magnesium was used with 10% FBS as a base solution. Different immersion media were prepared by adding different salts ($NaHCO_3$, $CaCl_2$ and $MgSO_4$) whilst all other parameters were constant. Two salt formulations were chosen as references that correspond to those in DMEM as a cell culture medium and in blood plasma.

The results showed that: (i) $MgSO_4$ has no significant influence on the degradation process despite its influence on the morphology of the interface layer by increasing its heterogeneity; (ii) $CaCl_2$ has a major role in magnesium degradation, and its presence lowers the degradation rate by enhancing Ca-PO_4 precipitation, which works as a surface-protecting deposition; and (iii) $NaHCO_3$ alone does not significantly influence the degradation rate but in co-addition with $CaCl_2$, it assists $CaCl_2$ in enhancing the formation of Ca-PO_4-based precipitations.

Therefore, for the material characterisation *in vitro*, it is recommended that an immersion medium only be used when its formula is supplemented with Ca. Despite the fact that the degradation rate was not significantly influenced by adding x$NaHCO_3$ (x=1150, 3350 mg/L) to the other two salts, $NaHCO_3$ had an important chemical role in altering the deposition and structure of $MgCO_3$. Therefore, the use of cell culture media that have lower bicarbonate concentrations than DMEM, such as Minimum Essential Media α (Alpha-MEM), for advanced degradation profile characterisation is recommended. Results of performing the degradation under complex cell culture media referred also to the importance of the Ca/P ratio which should be chosen near to the physiological body fluid, since it is critical for the apatite phase precipitation.

In the study of osteoblast cells influence on degradation, the degradation interface was successfully analysed by processing microsections with FIB milling and then performing EDX line scans on the degradation layer cross-sections. The degradation interface was altered in the presence of osteoblasts by their metabolic activity and their natural role in mediating bone formation. The interface on Mg-10Gd was rich in Ca, P and Gd, which indicated that Gd itself potentially contributed to HA precipitation and increased bone mineralisation ability. A contrary role was reported for Mg-2Ag, in which initial cell stress and damage were shown and less mineralisation was observed on the surface. Pure magnesium revealed moderate behaviour that was between the two studied alloys.

Future studies to address other physiological influences (e.g., proteins and other types of cells) would be interesting to perform.

7. References

1. Mittal, R., et al., *Use of bio-resorbable implants for stabilisation of distal radius fractures: the United Kingdom patients' perspective.* Injury, 2005. **36**(2): p. 333-338.
2. Pillai, C.K. and C.P. Sharma, *Review paper: absorbable polymeric surgical sutures: chemistry, production, properties, biodegradability, and performance.* J Biomater Appl, 2010. **25**(4): p. 291-366.
3. Muffly, T.M., A.P. Tizzano, and M.D. Walters, *The history and evolution of sutures in pelvic surgery.* Journal of the Royal Society of Medicine, 2011. **104**(3): p. 107-112.
4. Zheng, Y.F., X.N. Gu, and F. Witte, *Biodegradable metals.* Materials Science and Engineering: R: Reports, 2014. **77**: p. 1-34.
5. Gonzalo, N. and C. Macaya, *Absorbable stent: focus on clinical applications and benefits.* Vascular Health and Risk Management, 2012. **8**: p. 125-132.
6. El-Omar, M.M., et al., *Update on In-stent Restenosis.* Curr Interv Cardiol Rep, 2001. **3**(4): p. 296-305.
7. Schomig, A., et al., *Four-year experience with Palmaz-Schatz stenting in coronary angioplasty complicated by dissection with threatened or present vessel closure.* Circulation, 1994. **90**(6): p. 2716-24.
8. Pina, S. and J.M.F. Ferreira, *Bioresorbable Plates and Screws for Clinical Applications: A Review.* Journal of Healthcare Engineering, 2012. **3**(2).
9. Luthringer, B.J., F. Feyerabend, and R. Willumeit-Romer, *Magnesium-based implants: a mini-review.* Magnes Res, 2014. **27**(4): p. 142-54.
10. Li, H., Y. Zheng, and L. Qin, *Progress of biodegradable metals.* Progress in Natural Science: Materials International, 2014. **24**(5): p. 414-422.
11. Saris, N.-E.L., et al., *Magnesium: An update on physiological, clinical and analytical aspects.* Clinica Chimica Acta, 2000. **294**(1–2): p. 1-26.
12. Vormann, J., *Magnesium: nutrition and metabolism.* Molecular Aspects of Medicine, 2003. **24**(1–3): p. 27-37.
13. Wolf, F.I. and A. Cittadini, *Chemistry and biochemistry of magnesium.* Molecular Aspects of Medicine, 2003. **24**(1–3): p. 3-9.
14. Hartwig, A., *Role of magnesium in genomic stability.* Mutation Research/Fundamental and Molecular Mechanisms of Mutagenesis, 2001. **475**(1–2): p. 113-121.
15. Okuma, T., *Magnesium and bone strength.* Nutrition, 2001. **17**(7–8): p. 679-680.
16. Yamasaki, Y., et al., *Action of FGMgCO3Ap-collagen composite in promoting bone formation.* Biomaterials, 2003. **24**(27): p. 4913-4920.
17. Zreiqat, H., et al., *Mechanisms of magnesium-stimulated adhesion of osteoblastic cells to commonly used orthopaedic implants.* J Biomed Mater Res, 2002. **62**(2): p. 175-84.
18. Yamasaki, Y., et al., *Synthesis of functionally graded MgCO3 apatite accelerating osteoblast adhesion.* J Biomed Mater Res, 2002. **62**(1): p. 99-105.
19. Witte, F., et al., *In vivo corrosion of four magnesium alloys and the associated bone response.* Biomaterials, 2005. **26**(17): p. 3557-63.
20. Wen, C.E., et al., *Processing of biocompatible porous Ti and Mg.* Scripta Materialia, 2001. **45**(10): p. 1147-1153.
21. Witte, F., et al., *Degradable biomaterials based on magnesium corrosion.* Current Opinion in Solid State and Materials Science, 2008. **12**(5-6): p. 63-72.

22. Clarke, B., *Normal bone anatomy and physiology.* Clin J Am Soc Nephrol, 2008. **3 Suppl 3**: p. S131-9.
23. Aubin, J., *Bone formation: maturation and functional activities of osteoblast lineage cells. Primer on the metabolic bone diseases and disorders of mineral metabolism.* 2006.
24. Weitzmann, M.N. and R. Pacifici, *Estrogen deficiency and bone loss: an inflammatory tale.* Journal of Clinical Investigation, 2006. **116**(5): p. 1186-1194.
25. Kini, U. and B.N. Nandeesh, *Physiology of Bone Formation, Remodeling, and Metabolism*, in *Radionuclide and Hybrid Bone Imaging*, I. Fogelman, G. Gnanasegaran, and H. Wall, Editors. 2012, Springer Berlin Heidelberg: Berlin, Heidelberg. p. 29-57.
26. Witte, F., *The history of biodegradable magnesium implants: A review.* Acta Biomaterialia, 2010. **6**(5): p. 1680-1692.
27. Mc, B.E., *Absorbable metal in bone surgery: A further report on the use of magnesium alloys.* Journal of the American Medical Association, 1938. **111**(27): p. 2464-2467.
28. Troitskii, V.V. and D.N. Tsitrin, *The resorbing metallic alloy 'Osteosinthezit' as material for fastening broken bone.* Khirurgiia, 1944. **8** (1944): p. 41–44.
29. Borodkin, V.S., et al., *Magnesium-base alloy for use in bone surgery*. 1972, Google Patents.
30. Kraus, T., et al., *Magnesium alloys for temporary implants in osteosynthesis: in vivo studies of their degradation and interaction with bone.* Acta Biomater, 2012. **8**(3): p. 1230-8.
31. Plaaß, C., et al., *Frühergebnisse von distalen Metatarsale-1-Osteotomien bei Hallux valgus unter Verwendung eines biodegradierbaren Magnesium-Implantates.* Fuß & Sprunggelenk, 2015. **13**(3): p. 148-155.
32. Modrejewski, C., et al., *Degradationsverhalten bioresorbierbarer Magnesium-Implantate bei distalen Metatarsale-1-Osteotomien im MRT.* Fuß & Sprunggelenk, 2015. **13**(3): p. 156-161.
33. Hall, E.O., *The Deformation and Ageing of Mild Steel: III Discussion of Results.* Proceedings of the Physical Society. Section B, 1951. **64**(9): p. 747.
34. Petch, N.J., *The cleavage strength of polycrystals.* The Journal of the Iron and Steel Institute, 1953. **174**: p. 25-28.
35. Murr, L.E. and S.S. Hecker, *Quantitative evidence for dislocation emission from grain boundaries.* Scripta Metallurgica, 1979. **13**(3): p. 167-171.
36. Dieter, G.E., *Mechanical metallurgy*. 1961, New York: McGraw-Hill.
37. Hort, N., et al., *Magnesium alloys as implant materials – Principles of property design for Mg–RE alloys.* Acta Biomaterialia, 2010. **6**(5): p. 1714-1725.
38. Alvarez-Lopez, M., et al., *Corrosion behaviour of AZ31 magnesium alloy with different grain sizes in simulated biological fluids.* Acta Biomater, 2010. **6**(5): p. 1763-71.
39. Kannan, M.B., *Influence of microstructure on the in-vitro degradation behaviour of magnesium alloys.* Materials Letters, 2010. **64**(6): p. 739-742.
40. Ng, W.F., M.H. Wong, and F.T. Cheng, *Stearic acid coating on magnesium for enhancing corrosion resistance in Hanks' solution.* Surface and Coatings Technology, 2010. **204**(11): p. 1823-1830.

41. Feng, A. and Y. Han, *The microstructure, mechanical and corrosion properties of calcium polyphosphate reinforced ZK60A magnesium alloy composites.* Journal of Alloys and Compounds, 2010. **504**(2): p. 585-593.
42. Feyerabend, F., et al., *Evaluation of short-term effects of rare earth and other elements used in magnesium alloys on primary cells and cell lines.* Acta Biomater, 2010. **6**(5): p. 1834-42.
43. Gu, X.N., et al., *A study on alkaline heat treated Mg-Ca alloy for the control of the biocorrosion rate.* Acta Biomater, 2009. **5**(7): p. 2790-9.
44. Pereda, M.D., et al., *Corrosion inhibition of powder metallurgy Mg by fluoride treatments.* Acta Biomater, 2010. **6**(5): p. 1772-82.
45. Seitz, J.-M., et al., *Comparison of the Corrosion Behavior of Coated and Uncoated Magnesium Alloys in an In Vitro Corrosion Environment.* Advanced Engineering Materials, 2011. **13**(9): p. B313-B323.
46. Shi, P., et al., *Improvement of corrosion resistance of pure magnesium in Hanks' solution by microarc oxidation with sol–gel TiO2 sealing.* Journal of Alloys and Compounds, 2009. **469**(1-2): p. 286-292.
47. Song, G., *Recent Progress in Corrosion and Protection of Magnesium Alloys.* Advanced Engineering Materials, 2005. **7**(7): p. 563-586.
48. Shaw, B.A., *Corrosion resistance of magnesium alloys.* ASM Handbook, 2003. **13a**.
49. Staiger, M.P., et al., *Magnesium and its alloys as orthopedic biomaterials: a review.* Biomaterials, 2006. **27**(9): p. 1728-34.
50. Ullmann, B., et al., *Influence of the grain size on the in vivo degradation behaviour of the magnesium alloy LAE442.* Proc Inst Mech Eng H, 2013. **227**(3): p. 317-26.
51. Minárik, P., et al., *Evolution of mechanical properties of LAE442 magnesium alloy processed by extrusion and ECAP.* Journal of Materials Research and Technology, 2015. **4**(1): p. 75-78.
52. Dumitru, F.D., O.F. Higuera-Cobos, and J.M. Cabrera, *ZK60 alloy processed by ECAP: Microstructural, physical and mechanical characterization.* Materials Science and Engineering: A, 2014. **594**: p. 32-39.
53. Liu, Y., et al., *Effects of grain size on the corrosion resistance of pure magnesium by cooling rate-controlled solidification.* Frontiers of Materials Science, 2015. **9**(3): p. 247-253.
54. Yang, L., et al., *Mechanical and corrosion properties of binary Mg–Dy alloys for medical applications.* Materials Science and Engineering: B, 2011. **176**(20): p. 1827-1834.
55. Zhang, E. and L. Yang, *Microstructure, mechanical properties and bio-corrosion properties of Mg–Zn–Mn–Ca alloy for biomedical application.* Materials Science and Engineering: A, 2008. **497**(1–2): p. 111-118.
56. Zhou, Y.-L., et al., *Microstructures, mechanical and corrosion properties and biocompatibility of as extruded Mg–Mn–Zn–Nd alloys for biomedical applications.* Materials Science and Engineering: C, 2015. **49**: p. 93-100.
57. Hofstetter, J., et al., *Assessing the degradation performance of ultrahigh-purity magnesium in vitro and in vivo.* Corrosion Science, 2015. **91**: p. 29-36.
58. Nayeb-Hashemi, A.A. and J.B. Clark, *The Ag-Mg (Silver-Magnesium) system.* Bulletin of Alloy Phase Diagrams. **5**(4): p. 348-358.
59. Tie, D., et al., *Antibacterial biodegradable Mg-Ag alloys.* Eur Cell Mater, 2013. **25**: p. 284-98; discussion 298.

60. Atiyeh, B.S., et al., *Effect of silver on burn wound infection control and healing: review of the literature.* Burns, 2007. **33**(2): p. 139-48.
61. Klasen, H.J., *A historical review of the use of silver in the treatment of burns. II. Renewed interest for silver.* Burns, 2000. **26**(2): p. 131-138.
62. Chang, J., et al., *Investigation of the corrosion for Mg–xGd–3Y–0.4Zr (x = 6, 8, 10, 12 wt%) alloys in a peak-aged condition.* Corrosion Science, 2008. **50**(1): p. 166-177.
63. Gao, L., R.S. Chen, and E.H. Han, *Effects of rare-earth elements Gd and Y on the solid solution strengthening of Mg alloys.* Journal of Alloys and Compounds, 2009. **481**(1–2): p. 379-384.
64. He, S.M., et al., *Microstructure and strengthening mechanism of high strength Mg–10Gd–2Y–0.5Zr alloy.* Journal of Alloys and Compounds, 2007. **427**(1–2): p. 316-323.
65. KubÁSek, J. and D. VojtĚCh, *Structural and corrosion characterization of biodegradable Mg–RE (RE=Gd, Y, Nd) alloys.* Transactions of Nonferrous Metals Society of China, 2013. **23**(5): p. 1215-1225.
66. Gu, X.-N. and Y.-F. Zheng, *A review on magnesium alloys as biodegradable materials.* Frontiers of Materials Science in China, 2010. **4**(2): p. 111-115.
67. Ambat, R., N.N. Aung, and W. Zhou, *Studies on the influence of chloride ion and pH on the corrosion and electrochemical behaviour of AZ91D magnesium alloy.* Journal of Applied Electrochemistry, 2000. **30**(7): p. 865-874.
68. Levesque, J., et al., *Design of a pseudo-physiological test bench specific to the development of biodegradable metallic biomaterials.* Acta Biomater, 2008. **4**(2): p. 284-95.
69. Rettig, R. and S. Virtanen, *Time-dependent electrochemical characterization of the corrosion of a magnesium rare-earth alloy in simulated body fluids.* Journal of Biomedical Materials Research Part A, 2008. **85A**(1): p. 167-175.
70. Müller, W.D., et al., *Magnesium and its alloys as degradable biomaterials: corrosion studies using potentiodynamic and EIS electrochemical techniques.* Materials Research, 2007. **10**: p. 5-10.
71. Liu, C., et al., *Degradation susceptibility of surgical magnesium alloy in artificial biological fluid containing albumin.* Journal of Materials Research, 2007. **22**(07): p. 1806-1814.
72. Xu, L., et al., *In vivo corrosion behavior of Mg-Mn-Zn alloy for bone implant application.* Journal of Biomedical Materials Research Part A, 2007. **83A**(3): p. 703-711.
73. Ramazan Alper Kaya, et al., *The effects of magnesium particles in posterolateral spinal fusion: an experimental in vivo study in a sheep model.* Journal of Neurosurgery: Spine, 2007. **6**(2): p. 141-149.
74. Persaud-Sharma, D. and A. McGoron, *Biodegradable Magnesium Alloys: A Review of Material Development and Applications.* J Biomim Biomater Tissue Eng, 2012. **12**: p. 25-39.
75. Shi, Z. and A. Atrens, *An innovative specimen configuration for the study of Mg corrosion.* Corrosion Science, 2011. **53**(1): p. 226-246.
76. Kirkland, N.T., N. Birbilis, and M.P. Staiger, *Assessing the corrosion of biodegradable magnesium implants: A critical review of current methodologies and their limitations.* Acta Biomaterialia, 2012. **8**(3): p. 925-936.
77. Witte, F., et al., *In vitro and in vivo corrosion measurements of magnesium alloys.* Biomaterials, 2006. **27**(7): p. 1013-8.

78. Willumeit, R., A. Mohring, and F. Feyerabend, *Optimization of cell adhesion on mg based implant materials by pre-incubation under cell culture conditions.* Int J Mol Sci, 2014. **15**(5): p. 7639-50.
79. Kannan, M.B., A. Yamamoto, and H. Khakbaz, *Influence of living cells (L929) on the biodegradation of magnesium-calcium alloy.* Colloids Surf B Biointerfaces, 2015. **126**: p. 603-6.
80. Liedberg, H. and T. Lundeberg, *Silver alloy coated catheters reduce catheter-associated bacteriuria.* Br J Urol, 1990. **65**(4): p. 379-81.
81. Johnson, J.R., et al., *Prevention of catheter-associated urinary tract infection with a silver oxide-coated urinary catheter: clinical and microbiologic correlates.* J Infect Dis, 1990. **162**(5): p. 1145-50.
82. Chu, C.S., et al., *Therapeutic effects of silver nylon dressings with weak direct current on Pseudomonas aeruginosa-infected burn wounds.* J Trauma, 1988. **28**(10): p. 1488-92.
83. Jung, W.K., et al., *Antibacterial Activity and Mechanism of Action of the Silver Ion in Staphylococcus aureus and Escherichia coli.* Applied and Environmental Microbiology, 2008. **74**(7): p. 2171-2178.
84. Markowska, K., A.M. Grudniak, and K.I. Wolska, *Silver nanoparticles as an alternative strategy against bacterial biofilms.* Acta Biochim Pol, 2013. **60**(4): p. 523-30.
85. Wan, A.T., et al., *Determination of silver in blood, urine, and tissues of volunteers and burn patients.* Clin Chem, 1991. **37**(10 Pt 1): p. 1683-7.
86. Rosenman, K.D., A. Moss, and S. Kon, *Argyria: clinical implications of exposure to silver nitrate and silver oxide.* J Occup Med, 1979. **21**(6): p. 430-5.
87. Drake, P.L. and K.J. Hazelwood, *Exposure-related health effects of silver and silver compounds: A review.* Annals of Occupational Hygiene, 2005. **49**(7): p. 575-585.
88. Sherry, A.D., P. Caravan, and R.E. Lenkinski, *A primer on gadolinium chemistry.* Journal of magnetic resonance imaging : JMRI, 2009. **30**(6): p. 1240-1248.
89. Johannsson, O., et al., *Action of various metallic chlorides on calcaemia and phosphataemia.* British Journal of Pharmacology and Chemotherapy, 1968. **33**(1): p. 91-97.
90. Kindberg, G.M., et al., *The fate of Gd and chelate following intravenous injection of gadodiamide in rats.* European Radiology, 2010. **20**(7): p. 1636-1643.
91. Gibby, W.A., K.A. Gibby, and W.A. Gibby, *Comparison of Gd DTPA-BMA (Omniscan) versus Gd HP-DO3A (ProHance) retention in human bone tissue by inductively coupled plasma atomic emission spectroscopy.* Invest Radiol, 2004. **39**(3): p. 138-42.
92. White, G.W., W.A. Gibby, and M.F. Tweedle, *Comparison of Gd(DTPA-BMA) (Omniscan) versus Gd(HP-DO3A) (ProHance) relative to gadolinium retention in human bone tissue by inductively coupled plasma mass spectroscopy.* Invest Radiol, 2006. **41**(3): p. 272-8.
93. Darrah, T.H., et al., *Incorporation of excess gadolinium into human bone from medical contrast agents.* Metallomics, 2009. **1**(6): p. 479-488.
94. Spencer, A.J., et al., *Gadolinium chloride toxicity in the rat.* Toxicol Pathol, 1997. **25**(3): p. 245-55.
95. Rees, J., et al., *Time course of stomach mineralization, plasma, and urinary changes after a single intravenous administration of gadolinium(III) chloride in the male rat.* Toxicol Pathol, 1997. **25**(6): p. 582-9.

96. Hirano, S. and K.T. Suzuki, *Exposure, metabolism, and toxicity of rare earths and related compounds.* Environmental Health Perspectives, 1996. **104**(Suppl 1): p. 85-95.
97. Abraham, J.L., et al., *Dermal inorganic gadolinium concentrations: evidence for in vivo transmetallation and long-term persistence in nephrogenic systemic fibrosis.* Br J Dermatol, 2008. **158**(2): p. 273-80.
98. Weinmann, H.J., et al., *Characteristics of gadolinium-DTPA complex: a potential NMR contrast agent.* AJR Am J Roentgenol, 1984. **142**(3): p. 619-24.
99. Brasch, R.C., *Inherent Contrast in Magnetic Resonance Imaging and the Potential for Contrast Enhancement: The 1984 L. Henry Garland Lecture.* Western Journal of Medicine, 1985. **142**(6): p. 847-853.
100. Haley, T.J., et al., *Toxicological and pharmacological effects of gadolinium and samarium chlorides.* British Journal of Pharmacology and Chemotherapy, 1961. **17**(3): p. 526-532.
101. Bruce, D.W., B.E. Hietbrink, and K.P. DuBois, *The acute mammalian toxicity of rare earth nitrates and oxides.* Toxicology and Applied Pharmacology, 1963. **5**(6): p. 750-759.
102. Jai Poinern, G.E., S. Brundavanam, and D. Fawcett, *Biomedical Magnesium Alloys: A Review of Material Properties, Surface Modifications and Potential as a Biodegradable Orthopaedic Implant.* American Journal of Biomedical Engineering, 2012. **2**(6): p. 218-240.
103. Song, G.L. and A. Atrens, *Corrosion Mechanisms of Magnesium Alloys.* Advanced Engineering Materials, 1999. **1**(1): p. 11-33.
104. ZENG, R., E. HAN, and W. KE, *Corrosion of Artificial Aged Magnesium Alloy AZ80 in 3.5 wt pct NaCl Solutions.* J. Mater. Sci. Technol, 2007. **23**(03): p. 353-358.
105. Ambat, R., N.N. Aung, and W. Zhou, *Evaluation of microstructural effects on corrosion behaviour of AZ91D magnesium alloy*. Corrosion Science, 2000. **42**(8): p. 1433-1455.
106. Liu, L.J. and M. Schlesinger, *Corrosion of magnesium and its alloys.* Corrosion Science, 2009. **51**(8): p. 1733-1737.
107. Zeng, R., et al., *Progress and Challenge for Magnesium Alloys as Biomaterials.* Advanced Engineering Materials, 2008. **10**(8): p. B3-B14.
108. Shewmon, P. and G. Sundararajan, *THE EROSION OF METALS.* Annual Review of Materials Science, 1983. **13**: p. 301-318.
109. Winzer, N., et al., *Stress corrosion cracking in magnesium alloys: Characterization and prevention.* JOM, 2007. **59**(8): p. 49-53.
110. Fernandez, E., et al., *Calcium phosphate bone cements for clinical applications. Part I: solution chemistry.* J Mater Sci Mater Med, 1999. **10**(3): p. 169-76.
111. Vereecke, G. and J. Lemaître *Calculation of the solubility diagrams in the system Ca(OH) 2-H 3PO 4-KOH-HNO 3-CO 2-H 2O.* Journal of Crystal Growth, 1990(104): p. 820-832.
112. ASTM International, W.C., PA, *Standard test method for determining average grain size*. 2013, ASTM International.
113. Krebs, H.A., *Chemical composition of blood plasma and serum.* Annu Rev Biochem, 1950. **19**: p. 409-30.
114. Fischer, J., et al., *Improved cytotoxicity testing of magnesium materials.* Materials Science and Engineering: B, 2011. **176**(11): p. 830-834.

115. Birkholz, M., *Principles of X-ray Diffraction*, in *Thin Film Analysis by X-Ray Scattering*. 2006, Wiley-VCH Verlag GmbH & Co. KGaA. p. 1-40.
116. Ismail, A.A., F.R. van de Voort, and J. Sedman, *Chapter 4 Fourier transform infrared spectroscopy: Principles and applications*, in *Techniques and Instrumentation in Analytical Chemistry*, J.R.J. Paré and J.M.R. Bélanger, Editors. 1997, Elsevier. p. 93-139.
117. Subramanian, A. and L. Rodriguez-Saona, *Chapter 7 - Fourier Transform Infrared (FTIR) Spectroscopy A2 - Sun, Da-Wen*, in *Infrared Spectroscopy for Food Quality Analysis and Control*. 2009, Academic Press: San Diego. p. 145-178.
118. Bell, D.C. and N. Erdman, *Low Volatage Elactron Microscopy: Principles and Applications*. 2013 ed. Current and future titles in the Royal Microscopical Society—John Wiley Series, ed. S. Brooks. 2013: John Wiley & Sons Ltd.
119. Egerton, R., *Physical Principles of Electron Microscopy. An Introduction to TEM, SEM, and AEM*. 2005: Springer.
120. Schadler, S., C. Burkhardt, and A. Kappler, *Evaluation of electron microscopic sample preparation methods and imaging techniques for characterization of cell-mineral aggregates.* Geomicrobiology Journal, 2008. **25**(5): p. 228-239.
121. Schneider, C.A., W.S. Rasband, and K.W. Eliceiri, *NIH Image to ImageJ: 25 years of image analysis.* Nat Meth, 2012. **9**(7): p. 671-675.
122. Moreno, E.C., et al., *Precipitation of hydroxyapatite from dilute solutions upon seeding.* Calcified Tissue Research, 1977. **24**(1): p. 47-57.
123. Song, Y., H.H. Hahn, and E. Hoffmann, *Effects of solution conditions on the precipitation of phosphate for recovery: A thermodynamic evaluation.* Chemosphere, 2002. **48**(10): p. 1029-1034.
124. Zhu, P., et al., *Investigation of Apatite Deposition onto Charged Surfaces in Aqueous Solutions Using a Quartz-Crystal Microbalance.* Journal of the American Ceramic Society, 2003. **86**(5): p. 782-790.
125. Willumeit, R., et al., *Chemical surface alteration of biodegradable magnesium exposed to corrosion media.* Acta Biomater, 2011. **7**(6): p. 2704-15.
126. Muller, L. and F.A. Muller, *Preparation of SBF with different HCO3- content and its influence on the composition of biomimetic apatites.* Acta Biomater, 2006. **2**(2): p. 181-9.
127. Yamamoto, A. and S. Hiromoto, *Effect of inorganic salts, amino acids and proteins on the degradation of pure magnesium in vitro.* Materials Science & Engineering C-Biomimetic and Supramolecular Systems, 2009. **29**(5): p. 1559-1568.
128. Lindström, R., et al., *Corrosion of magnesium in humid air.* Corrosion Science, 2004. **46**(5): p. 1141-1158.
129. Cui, Z., et al., *Atmospheric corrosion of field-exposed AZ31 magnesium in a tropical marine environment.* Corrosion Science, 2013. **76**: p. 243-256.
130. Barrere, F., et al., *Influence of ionic strength and carbonate on the Ca-P coating formation from SBF×5 solution.* Biomaterials, 2002. **23**(9): p. 1921-1930.
131. Wopenka, B. and J.D. Pasteris, *A mineralogical perspective on the apatite in bone.* Materials Science and Engineering: C, 2005. **25**(2): p. 131-143.
132. Bigi, A., et al., *The role of magnesium on the structure of biological apatites.* Calcified Tissue International, 1992. **50**(5): p. 439-444.
133. Barrere, F., et al., *Nucleation of biomimetic Ca–P coatings on Ti6Al4V from a SBF×5 solution: influence of magnesium.* Biomaterials, 2002. **23**(10): p. 2211-2220.

134. Xin, Y., et al., *Influence of aggressive ions on the degradation behavior of biomedical magnesium alloy in physiological environment.* Acta Biomater, 2008. **4**(6): p. 2008-15.
135. Światowska, J., P. Volovitch, and K. Ogle, *The anodic dissolution of Mg in NaCl and Na2SO4 electrolytes by atomic emission spectroelectrochemistry.* Corrosion Science, 2010. **52**(7): p. 2372-2378.
136. Zeng, R.-C., et al., *Corrosion of magnesium alloy AZ31: The influence of bicarbonate, sulphate, hydrogen phosphate and dihydrogen phosphate ions in saline solution.* Corrosion Science, 2014. **86**: p. 171-182.
137. Ardelean, H., et al., *Corrosion processes of Mg–Y–Nd–Zr alloys in Na2SO4 electrolyte.* Corrosion Science, 2013. **73**: p. 196-207.
138. Jang, Y., et al., *Effect of biologically relevant ions on the corrosion products formed on alloy AZ31B: an improved understanding of magnesium corrosion.* Acta Biomater, 2013. **9**(10): p. 8761-70.
139. Elliott, J.C., *Structure and Chemistry of the Apatites and Other Calcium Orthophosphates*, in *Studies in Inorganic Chemistry*, J.C. Elliott, Editor. 1994, Elsevier. p. 1-389.
140. Mekmene, O., et al., *Effects of pH and Ca/P molar ratio on the quantity and crystalline structure of calcium phosphates obtained from aqueous solutions.* Dairy Science & Technology, 2009. **89**(3-4): p. 301-316.
141. Rey, C., et al., *Fourier transform infrared spectroscopic study of the carbonate ions in bone mineral during aging.* Calcified Tissue International, 1991. **49**(4): p. 251-258.
142. Van der Houwen, J.A.M. and E. Valsami-Jones, *The application of calcium phosphate precipitation chemistry to phosphorus recovery: The influence of organic ligands.* Environmental Technology, 2001. **22**(11): p. 1325-1335.
143. van der Houwen, J.A.M., et al., *The effect of organic ligands on the crystallinity of calcium phosphate.* Journal of Crystal Growth, 2003. **249**(3–4): p. 572-583.
144. Gordon, J.A., et al., *Bone sialoprotein expression enhances osteoblast differentiation and matrix mineralization in vitro.* Bone, 2007. **41**(3): p. 462-73.
145. Neve, A., A. Corrado, and F.P. Cantatore, *Osteoblast physiology in normal and pathological conditions.* Cell Tissue Res, 2011. **343**(2): p. 289-302.
146. Suvorova, E.I. and P.A. Buffat, *Electron diffraction and high resolution transmission electron microscopy in the characterization of calcium phosphate precipitation from aqueous solutions under biomineralization conditions.* Eur Cell Mater, 2001. **1**: p. 27-42.
147. Cortizo, M., M. de Mele, and A. Cortizo, *Metallic dental material biocompatibility in osteoblastlike cells.* Biological Trace Element Research, 2004. **100**(2): p. 151-168.
148. Myrissa, A., et al., *In vitro and in vivo comparison of binary Mg alloys and pure Mg.* Materials Science and Engineering: C, 2016. **61**: p. 865-874.
149. Burmester, A., R. Willumeit-Romer, and F. Feyerabend, *Behavior of bone cells in contact with magnesium implant material.* J Biomed Mater Res B Appl Biomater, 2015.
150. Barros, L.F., et al., *Apoptotic and necrotic blebs in epithelial cells display similar neck diameters but different kinase dependency.* Cell Death Differ, 2003. **10**(6): p. 687-97.
151. Dai, J. and M.P. Sheetz, *Membrane tether formation from blebbing cells.* Biophys J, 1999. **77**(6): p. 3363-70.
152. Liu, W., et al., *Impact of silver nanoparticles on human cells: effect of particle size.* Nanotoxicology, 2010. **4**(3): p. 319-30.

153. Asharani, P.V., et al., *Comparison of the toxicity of silver, gold and platinum nanoparticles in developing zebrafish embryos.* Nanotoxicology, 2011. **5**(1): p. 43-54.
154. Albers, C.E., et al., *In vitro cytotoxicity of silver nanoparticles on osteoblasts and osteoclasts at antibacterial concentrations.* Nanotoxicology, 2013. **7**(1): p. 30-6.
155. Contreras, R.G., et al., *Type of cell death induced by seven metals in cultured mouse osteoblastic cells. In Vivo*, 2010. **24**(4): p. 507-12.
156. Kawata, K., M. Osawa, and S. Okabe, *In Vitro Toxicity of Silver Nanoparticles at Noncytotoxic Doses to HepG2 Human Hepatoma Cells.* Environmental Science & Technology, 2009. **43**(15): p. 6046-6051.
157. Zhang, J., et al., *Effects of gadolinium on proliferation, differentiation and calcification of primary mouse osteoblasts in vitro.* Journal of Rare Earths, 2012. **30**(8): p. 831-834.
158. Wang, X., et al., *The morphogenetically active polymer, inorganic polyphosphate complexed with GdCl, as an inducer of hydroxyapatite formation in vitro.* Biochem Pharmacol, 2015.
159. Song, G., et al., *The electrochemical corrosion of pure magnesium in 1 N NaCl.* Corrosion Science, 1997. **39**(5): p. 855-875.
160. BarrÈre, F., et al., *Biomimetic calcium phosphate coatings on Ti6Al4V: a crystal growth study of octacalcium phosphate and inhibition by Mg2+ and HCO3−.* Bone, 1999. **25**(2, Supplement 1): p. 107S-111S.

Acknowledgements

This thesis is a report of my research carried out from June 2012 to March 2016. At the end of this fruitful time, I would like express my sincere thanks to my supervisor, Prof. Dr. Regine Willumeit-Römer, for giving me the opportunity to work in the “Institute of Metallic Biomaterials” in Helmholtz-Zentrum Geesthacht (HZG) as well as for her continuous support and scientific guidance. I would like to extend my sincere thanks to my direct supervisor, Dr. Frank Feyerabend, for his support and for being open to questions, interacting with scientific ideas, and sharing deep discussions. My thanks to Prof. Dr. Christine Selhuber-Unkel for her supervision in Kiel University and for giving me the opportunity to become a PhD candidate. My special thanks to Prof. Dr. Boriana Mihailova from Hamburg University for her cooperation and deep discussions concerning FTIR and EMPA analyses.

I also express my thanks to researchers from the Institute of Metallic Biomaterials in HZG and to Dr. Bérengère Luthringer for her support and fruitful discussions concerning the biological characterisation in my work. My thanks also to Dr. Thomas Ebel and Prof. Dr. Micheal Dahms for their scientific meetings.

I am thankful for Dr. Daniel Laipple from the Material Institute in HZG for his help in performing the experiments with the SEM/FIB device. I would like to extend my thanks to Ute Kohlmeyer (Galab, Hamburg, Germany) for providing the ICP-MS measurement and to Gabor Szakacs and Yiyi Lu from the Magnesium Innovation Centre (MagIC) in HZG for their support in materials production and material characterisation.

I would like to deeply thank Gabriele Salamon for introducing me to cell culture and for her technical assistance in the laboratory, in addition to her support during my maternity leave. I would like to remember all colleagues, lab technicians and friends for providing me with a peaceful working environment and sharing a nice time together.

Finally, my heartfelt thanks to my parents, sisters, husband and son for encouraging me, blessing me and cheering me on.

The research leading to these results has received funding from the People Program (Marie Curie Actions) of the European Union's Seventh Framework Program FP7/2007-2013/ under REA grant agreement n° 289163.

List of Figures

Appendix

1. Abbreviations

BSE	Backscattered Electron
CCC	Cell Culture Conditions
CPD	Critical Point Drying
DAPI	4´,6-Diamidino-2-Phenylindole Dihydrochloride
DMEM	Dulbecco's Modified Eagle Medium
DR	Degradation Rate
EDX	Energy Dispersive X-ray
EIXE	Electron Induced X-ray Emission spectroscopy
EMPA	Electron Microprobe Analysis
FBS	Fetal Bovine Serum
FITC	Fluorescence Isothiocynate
FTIR	Fourier Transform Infrared microspectroscopy
HBSS	Hank's Balanced Salt Solution
ICP-MS	Inductive Coupled Plasma- Mass Spectroscopy
L929	Fibroblast L929 mouse cell line
LDH	Lactate Dehydrogenase
OB	Osteoblasts
P/S	Penicillin/Streptomycin
PBS	Phosphate Buffered Solution
RPMI	Rosewell Park Memorial Institute media
RT	Room Temperature
SEM	Scanning Electron Microscope
XRD	X-ray Diffraction

2. Chemical elements symbols and formulas

Ag	Silver
Ar	Argon
Ca	Calcium
$Ca_5(PO_4)_3OH$	Hydroxyapatite (in enamel and bone)
$CaC_2O_4.H_2O$	Whewellite
$CaCl_2$	Calcium chloride
Cl	Chlorine
Gd	Gadolinium
HCO_3^-	Carbonate
K	Potassium
Mg	Magnesium
$Mg(OH)_2$	Brucite
$MgCO_3$	Struvite
$MgSO_4$	Magnesium sulphate
Na	Sodium
$NaHCO_3$	Sodium bicarbonate
P	Phosphorus
PO_4	Phosphate

3. List of publications

Papers:

Nezha Ahmad Agha, Frank Feyerabend, Boriana Mihailova, Stefanie Heidrich, Ulrich Bismayer and Regine Willumeit-Römer: Magnesium Degradation Influenced by Buffering Salts in Concentrations Typical of *In vitro* and *In vivo* Models. Materials science and engineering. Matierals Science and Engineering C 58 (2016) 817-825. doi: 10.1016/j.msec.2015.09.067.

Nezha Ahmad Agha, Regine Willumeit-Römer, Daniel Laipple, Berengere Luthringer, Frank Feyerabend: The Degradation Interface of Magnesium Based Alloys in Direct Contact with Human Primary Osteoblasts Cells. PLOS One. doi: 10.1371/journal.pone.0157874.

Cecchinato Francesca[*], **Nezha Ahmad[*],** Adela Martinez, Berengere Luthringer, Frank Feyerabend, Ann Wennerberg, Ryo Jimbo, Regine Willumeit: Influence of binary magnesium alloys corrosion on morphology and adhesion of human undifferentiated cells. PLOS One. doi:10.1371/journal.pone.0142117. (* Equally contributed)

Anastasia Myrissa, **Nezha Ahmad Agha**, Yiyi Lu, Elisabeth Martinelli, Johannes Eichler, Gabor Szakacs, Claudia Kleinhans, Regine Willumeit Römer, Ute Schäfer, Annelie-Martina weinberg: *In vitro* and *in vivo* comparison of binary Mg alloys and pure Mg. Materials Science and Engineering C 61 (2016) 865-874. doi:10.1016/j.msec.2015.12.064.

Frank Feyerabend, Hans-peter Wendel, Boriana Mihailova, Stefanie Heidrich, **Nezha Ahmad Agha**, Ulrich Bismayer, Regine Willumeit Römer: Blood compatibility of magnesium and its alloys**.** Acta Biomaterialia 25 (2015) 384-394. doi:10.1016/j.actbio.2015.07.029.

Olga charyeva, Frank Feyerabend, Regine Willumeit-Römer, Daniel Zukuwski, Cryille Gasqueres, Gabor Szakacs, **Nezha Ahmad Agha**, Norbert Hort, Felix Gensch, Francesca Cecchinato, Ryo Jimbo, Ann Wennrberg, Katrin Sussane Lips: *In vitro* Resorption of Magnesium Materials and its Effect on Surface and Surrounding Environment. MOJ Toxicology 1 (2015). doi: 10.15406/mojt.2015.01.00004.

Conference abstracts:

Nezha Ahmad Agha, Daniel Laipple, Regine Willumeit-Römer, Frank Feyerabend: Magnesium degradation influenced by cell interaction. 7th Symposium on Biodegradable Metals. Published in European cell and materials Vol. 30. Suppl. 3, 2015 (page 86).

Nezha Ahmad Agha, Frank Feyerabend, Boriana Mihailova, Hans-Peter Wendel, Daniel Laipple, Regine Willumeit Römer. Magnesium Implant degradation influenced by blood and cells. 27th European Conference on Biomaterials (2015).

Nezha Ahmad Agha, Frank Feyerabend, Boriana Mihailova, Stefanie Heidrich, Regine Willumeit. Magnesium corrosion under physiological conditions. 6th Symposium on Biodegradable Metals. Published in European cell and materials Vol. 28. Suppl. 3, 2014 (page 22).

Nezha Ahmad Agha, Frank Feyerabend, Boriana Mihailova, Regine Willumeit. Magnesium corrosion under physiological conditions. Magnesium in translational medicine conference (2014).

Francesca Cecchinato, **Nezha Ahmad**, Frank Feyerabend, Ryo Jimbo, Regine Willumeit-Römer, Ann Wennerberg: Influence of magnesium alloys degradation on human undifferentiated cells. 7th Symposium on Biodegradable Metals. Published in European cell and materials Vol. 30. Suppl. 3, 2015 (page 68).

Regine Willumeit-Römer, Hans-peter Wendel, Boriana Mihailova, **Nezha Ahmad Agha**, Frank Feyerabend. How does blood contact change Magnesium degradation?. 6th Symposium on Biodegradable Metals. Published in European cell and materials Vol. 28. Suppl. 3, 2014 (page 29).

Awards:

3rd ranking place for best posters presented about *In vitro* studies in the 7th Symposium on Biodegradable Metals.

MAGNESIA award for the recognition of excellent research work of Dr. Regine Willumeit group presented in the conference: ‘’magnesium in translational medicine’’ (2014).